



**Università
degli Studi
di Palermo**

AREA QUALITÀ, PROGRAMMAZIONE E SUPPORTO STRATEGICO
SETTORE STRATEGIA PER LA RICERCA
U. O. DOTTORATI

Dottorato di ricerca in Ingegneria dell'Innovazione Tecnologica
Dipartimento di Ingegneria
Settore Scientifico Disciplinare: ING-IND/14

Unconventional application of Image Correlation techniques on Biomaterials and cardiovascular applications

LA DOTTORESSA
SOFIA DI LEONARDO

IL COORDINATORE
Prof. SALVATORE GAGLIO

I TUTOR
Prof. GIUSEPPE PITARRESI
Prof. GAETANO BURRIESCI

XXXIV ciclo
2021/2022

Table of Contents

Table of Contents	I
List of Figure.....	III
List of Tables.....	IX
Abstract	X
Acknowledgements	XII
Abbreviation.....	XIII
Symbols.....	XV
1. Introduction	1
1.1 Thesis Outline	2
2. Background	5
2.1 Cardiovascular issues	5
2.1.1 Complex biomaterials	6
2.1.2 Complex fluid-dynamics.....	7
3. Materials and Methods	10
3.1 Materials.....	10
3.1.1 Artificial heart valves.....	10
3.1.2 Nitinol	14
3.2 Experimental Techniques.....	16
3.2.1 Cross-correlation based.....	16
3.2.1.1 DIC.....	18
3.2.1.2 PIV	22
3.2.2 Thermal based.....	26
3.2.2.1 IRT	26
3.3 Experimental Apparatus.....	29
3.3.1 Pulse Duplicator system.....	29
4. Cardiovascular prostheses applications.....	35
4.1 Complex biomaterials	35
4.1.1 Nitinol characterisation.....	35
4.1.1.1 Mechanical characterisation (DIC).....	36
4.1.1.2 Thermo-Mechanical characterisation (DIC and IRT).....	60
4.1.2 Biological tissue characterisation (DIC).....	72
4.2 Complex fluid-dynamics.....	85

4.2.1	Analysis of healthy native aortic valve (and effects of alterations – valve sparing technique ex vivo).....	86
4.2.2	EOA direct measurement (PIV).....	96
4.2.3	Experimental issues	104
4.2.3.1	Experimental feasibility (SPH – PIV)	105
4.2.3.2	Refractive Index Matching	114
5.	Conclusion	130
6.	Appendix	134
	Appendix A. Selection of the $ROI_{s\sigma}$ dimension based on the maximum estimated error on the stress determination.....	134
	Appendix B. Angles between the regions at the interface between the two phases	137
	Appendix C. Manufacturing	138
	Appendix D. Custom Heat Exchanger for sided liquids.....	141
	Bibliography.....	146

List of Figure

Figure 1 Sketch of the heart in sagittal and transversal section [26]	7
Figure 2 Left heart cardiac cycles [27]	8
Figure 3 Sketch of the aortic root anatomy [30]	9
Figure 4 Mechanical valves: a) Ball-and-cage valve (Starr-Edwards) [39], b) tilting disc valve (Medtronic-Hall) [40], c) Bileaflet valve (St. Jude) [41]	11
Figure 5 Porcine biological valve (Perimount) [43]	12
Figure 6 TAVI valves: a) balloon-expandable valve (Cribier valve) [47], b) self-expanding valve (Medtronic CoreValve) [5]	13
Figure 7 Nitinol behaviours [56].....	15
Figure 8 a) bovine pericardium natural pattern, b) C–Mn steel metal microstructure[61], c) black and white painted spackel[2], d) etched aluminium alloy[62]	19
Figure 9 The basic steps of the Ncorr algorithm correlation [3].....	21
Figure 10 PIV 2D setup [63].....	22
Figure 11 a) IR match during correlation, b) peak finding [63].....	23
Figure 12 ViVitro pulse duplicator system [77]	30
Figure 13 Pulse duplicator system diagram [77].....	31
Figure 14 Pulse duplicator data output.....	32
Figure 15 Specimen speckle surface	38
Figure 16 Propagation of the front of phase transition observed in a generic ROI between two successive images, superposed to the region of gradual strain variation	

predicted by the DIC technique (a); and strain map after exclusion of the transition region (b).....	41
Figure 17 Regions of interest selected for the calculation of the Young's moduli and Poisson's ratios (a); and for the determination of the stress-strain parameters (b)....	45
Figure 18 Stress-strain curve obtained from the tensile machine output (a); and fitting used for the determination of the parameters defining the mechanical behaviour of the material (b).....	47
Figure 19 a) Horizontal displacement map; b) vertical displacement map; c) horizontal strain map; d) vertical strain map.....	48
Figure 20 a) Instants of the cycle (i-ix) where the sequence of whole specimen deformations in (b) was determined. Horizontal displacements (of Figure 19a) are amplified of 10 times, and the regions occupied by austenite and martensite, obtained from the strain maps, are represented in light and dark grey, respectively.....	49
Figure 21 a) Shape of the specimen with amplified lateral displacements; b) map of the specimen showing the austenitic and martensitic regions, and the position of the neutral axis represented by a white line (calculated using Equation 19); c) principal directions determined on the measured strains. All pictures are in relation to the instant P, as indicated in Figure 18.a.	51
Figure 22 Typical stress-strain map determined on square ROIs with side equal to 25% of the specimen width (in Figure 17.b), positioned on the axis of the specimen (a); and fitting used for the determination of the parameters defining the mechanical behaviour of the material (b).....	52

Figure 23 Schematic representation of the region of interface between the austenitic and martensitic regions (a), and of the full specimen in the transformation plateau region (b).....	56
Figure 24 Stress-strain map determined with the standard and DIC approaches described in the article.	58
Figure 25 Plot of the load vs displacement or engineering stress/strain curves for test QS, and comparison of thermal and ϵ_{yy} DIC maps on some selected points along the upper and lower plateaus of phase transformation transitory	65
Figure 26 a) Plot of Load-Displacement curve for test C; (b) map of ϵ_{yy} strain from DIC during the first cycling ed c) map of ϵ_{yy} strain from DIC during the second cycling	66
Figure 27 a) Thermogram preceding the start of first cycling stage; b) plots of temperature versus frames (i.e. time) during cycling from points MT and AS, indicated in (a) and the related zoomed detail of the temperature variation.....	67
Figure 28 a) Power and b) Phase spectrum of the Load signal.....	68
Figure 29 a,c) Power and b,d) Phase spectrum of the temperature signal referred to Austenite and Martensite areas	69
Figure 30 Maps of C_{up} test thermoelastic amplitude signal of the first a), second b) and third c) harmonic and in d),e) and f) the respective phase map.	70
Figure 31 gripping mechanisms: a) sutures and b) rakes [7]	74
Figure 32 Specimen cutting layout	75
Figure 33 Wide specimen clamped with a detail of the speckle	76
Figure 34 a) Lifting system, b) Specimen cutting.....	76

Figure 35 Simulation design a) wide, medium, small and trimmed specimen; b) wide trimmed specimen	78
Figure 36 Wide specimen and rakes structurally meshed	79
Figure 37 ϵ_{xx} strain map of: wide specimen a) experimental, b) numerical; medium specimen c) experimental, d) numerical; small specimen e) experimental, f) numerical; trimmed specimen g) experimental, h) numerical;	82
Figure 38 Numerical wide trimmed specimen ϵ_{xx} strain map	83
Figure 39 True stress strain curves a) experimental; b) numerical	83
Figure 40 Specimen bending during traction test	84
Figure 41 FreeStyle (Medtronic) prosthesis. Frontal, Bottom and Top views.....	89
Figure 42 David implant step by step: (a) equipment, (b) FreeStyle cutting, (c) valve preparation, (d) graft positioning, (e) graft suturing, (f) final implant.....	90
Figure 43 FreeStyle prosthesis and the three valve-sparing implants, David, Yacoub and De Paulis, set into resin support.	91
Figure 44 Implant performance parameter diagram of: a) mean systolic transvalvular pressure drop (SN4); b) mean systolic transvalvular pressure drop (SN5); c) Effective orifice area (SN4); d) Effective orifice area (SN5); e) Closing Regurgitant volume (SN4); f) Closing Regurgitant volume (SN5); g) Energy Loss (Forward + Closing) (SN4); h) Energy Loss (Forward + Closing) (SN5).....	94
Figure 45 Schematic flow through a stenotic aortic valve [127]	97
Figure 46 Particles movement in the laser thickness in an interval of time Δt	99
Figure 47 Sagittal planes (S_1, S_2) and transversal plane (T) identification.....	100
Figure 48 a) Setup for transversal plane, b) picture of the light sheet, c) mechanical valve view with the light on and laser off, d) biological valve view with laser on..	101

Figure 49 Velocity magnitude of st. Jude mechanical valve on plane a) S1, b) S2.	102
Figure 50 St. Jude mechanical valve a) velocity magnitude on T plane b) percent of invalid vectors (CHC=-1).....	103
Figure 51 Velocity magnitude of Perimount biological valve on plane a) S1, b) S2	103
Figure 52 Perimount biological valve a) velocity magnitude on T plane b) percent of invalid vectors (CHC=-1).....	104
Figure 53 Case of study a) 3D view b) dimensioned drawing in millimetres.....	109
Figure 54 Example of Synthetic image.....	110
Figure 55 a) Mean velocity vectors in flow direction, b) standard deviation	112
Figure 56 SPH results: a) magnitude velocity displayed for every particle, b) velocity vector field	113
Figure 57 Refraction of a light rays that cross an interface between materials with different RI [159]	114
Figure 58 Mismatching experimental set-up.....	118
Figure 59 Regions of correlation.....	119
Figure 60 a) Dog-bone pericardium specimens, b) specimen support, c) gripped and immersed specimen.....	121
Figure 61 Qualitative schedule plot of test in PBS	123
Figure 62 Qualitative schedule plot of test in PG solution	123
Figure 63 Picture composed of: a) 100% PBS (or % PG); b) 100% PG	125
Figure 64 a) Best match between PG solution and Sylgard-184, b) diagram of correlation coefficient R and viscosity respect to PG concentration	126

Figure 65 a) Best match between PG solution and FER-7061, b) diagram of correlation coefficient R and viscosity respect to PG concentration.....	126
Figure 66 Stress-strain plot of the first in PBS repetition performed on the first sample	127
Figure 67 C1a curves for all the repetition with PBS and PG of specimen a) SP2 b) SP3	128
Figure 68 Maximum stress of all the repetition for specimen a) SP2 and b) SP3 ...	128
Figure 69 Comparison between: a) SP3 kept in PG solution and SP1 kept in PBS solution b) SP3 kept after test few days in PBS solution and SP1 kept in PBS solution	129
Figure 70 a) Specimen cross-section; b) Bending moment diagram	136
Figure 71 Aortic root 3D model.....	138
Figure 72 Refractive index 3D model of the mould	139
Figure 73 Aortic mock root 3D model.....	140
Figure 74 Mould for mock root realization a) 3D model b) printed mould.....	141
Figure 75 Sylgard-184 aortic mock root	141
Figure 76 a) ViVitro heat exchanger, b) Heat bath	142
Figure 77 ViVitro setup for PIV tests at body temperature	143
Figure 78 Controlbox a) front panel, b) back panel	144
Figure 79 Electric circuit sketch	145

List of Tables

Table 1 Mechanical characteristics obtained with the different approaches.....	53
Table 2 Experiments Denomination	63
Table 3 Maximum value of stress for all the cases	84
Table 4 Implant performance parameter at 5 l/min of Cardiac Output.....	95
Table 5 Mean velocity component and relative standard deviation.....	112
Table 6 Material Properties at room temperature	117

Abstract

Image Correlation techniques are increasing in popularity and are now suitable to investigate complex structural and fluid-dynamics of cardiovascular systems. These approaches operate through a digital correlation of a pair of images to determine physical quantities of complex systems. In this thesis, their application to the mechanical characterisation of complex biomaterials (Nitinol and soft materials), and the characterisation of complex biofluid-dynamics was investigated, with the aim to analyse their reliability and enhance their accuracy and field of application.

Digital Image Correlation, supported by Infrared Thermography, was used to achieve a more in depth understanding of the mechanical behaviour of Nitinol shape memory alloys. The analysis led to the design of a new approach that minimise the error of standard characterisation methods.

Application of DIC to soft materials focused on biaxial test protocols commonly adopted in their characterisation. These were investigated, identifying major drawbacks that reduce the accuracy of the results. A new setup arrangement of easy implementation was developed to reduce the source of errors from above 50% to below 20%.

For the characterisation of complex biofluid-dynamics, a new Particle Image Velocimetry (PIV) approach was attempted to improve the current estimation of the Effective Orifice Area (the leading parameter in heart valves characterisation) by allowing its direct measurement.

Previously unreported limitations in the application of PIV to the analysis of the fluid-dynamics in complex cardiovascular cases were identified and investigated by implementing a new approach based on the use of SPH (Smoothed-particle hydrodynamics) *Synthetic Images*.

Image correlation techniques were also used to address another experimental issue typical of PIV applications in cardiovascular engineering, the refractive index mismatch between blood equivalent test fluid and the anatomical phantoms. In particular, a new blood equivalent was developed, with similar density and viscosity as human blood at body temperature. This has same refractive index as a new optically transparent silicone (FER-7061), for which a prototyping protocol was implemented. In summary, this thesis presents a range of studies focused on applications of digital image correlation to cardiovascular engineering, making a distinct contribution to the state of knowledge in the area by identifying main limitations of the different methods and proposing new original approaches that allow to minimise them, to better support the development and assessment of safer and more effective cardiovascular solutions.

Acknowledgements

I miei più sentiti ringraziamenti vanno ai miei Tutor Gaetano Burriesci e Giuseppe Pitarresi che hanno acceso ed alimentato la mia curiosità guidandomi nella ricerca. Ringrazio in particolare ancora Gaetano Burriesci e la Fondazione Ri.MED per avermi inserito in un gruppo di ricerca composto da: Danila Vella, Alessandra Monteleone, Alessia Viola e Giulio Musotto, diventato ormai anche un gruppo di amici che ringrazio per aver in questi anni ascoltato e condiviso le mie preoccupazioni, i mille discorsi sui possibili risvolti negativi degli esperimenti e le mie battute non sempre divertenti.

I would like also to thank the UCL Cardiovascular Engineering team: Jake Salmonsmit, Giorgia Bosi, Ebba Montgomery Liljeroth and at last (non per importanza) my mentor Andrea for their support in my UCL research periods.

In fine vorrei ringraziare per il loro supporto tutti i componenti della mia famiglia Mamma, Papà e Alice sempre presenti nella mia vita, ed i nuovi componenti: la mia nipotina Costanza e mio cognato Leoluca; i miei cognati Alberto, Andrea e Manfredi e i miei suoceri Marica e Sergio. Ma soprattutto vorrei ringraziare mio marito Pierfrancesco per aver sempre supportato e condiviso le più importanti decisioni della mia vita.

Abbreviation

AAo	Ascending Aorta
CFD	Computational Fluid Dynamics
CHC	Choice code
CO	Cardiac Output
DCC	Direct Cross-Correlation
DFT	Discrete Fourier Transformation
DIC	Digital Image Correlation
EOA	Effective Orifice Area
FDA	Food and Drug Administration
FEA	Finite Element Analysis
FFT	Fast Fourier Transform
FOV	Field of View
FSI	Fluid-Structure Interaction
GOA	Geometric Orifice Area
IR	Interrogation Region
IRT	Infrared Thermography
LVOT	Left Ventricle Outflow Tract

NETD	Noise Equivalent Temperature Difference
NTC	Thermocouple
PANORMUS	Parallel Numerical Open-source Model for Unsteady flow Simulations
PBS	Phosphate Buffered Saline
PG	Propylene Glycol
PID	Proportional–Integral–Derivative controller
PIV	Particle Image Velocimetry
PLA	Polylactic Acid
PT100	Thermocouple
ROI	Region of Interest
SJ	Sinotubular Junction
SPH	Smoothed-particle hydrodynamics
SV	Stroke Volume
TAVI	Transcatheter Aortic Valve Implantation
TSA	Thermoelastic Stress Analysis
VSG	Virtual strain gage

Symbols

Roman symbols

A, B	Compared images
A_1, A_2, A_3	Harmonics amplitude components
A_m	Mean value of the harmonic signal
C	Tube cross-section
c_p	Specific heat at constant pressure
c_v	Specific heat at constant volume
d	Displacement
D	Tube diameter
e	Eccentricity of the neutral axis
E	Young's modulus
E_A	Young's modulus of the austenitic phase
E_f, E_c, E_l	Forward, Closing and Leakage Energy loss
E_M	Young's modulus of the martensitic phase
f	Frequency
F	Force measured at the load-cell
h_A, h_M	Segment lengths of Figure 23

I, I^*	Pixel light intensity of the reference and investigated sub-image
I_m, I_m^*	Mean light intensity values of the reference and current sub-image
K	Thermoelastic constant of equation 8
K_0, K_1	Thermoelastic coefficients of equation 9
l	Specimen gauge length
l_t	Laser thickness
m, n	image row and column
M	Magnification factor
M_{max}	Maximum bending moment
n_1, n_2	Materials refractive index of Figure 57
p	Subset dimension
Δp	Mean Systolic Transvalvular Pressure Drop
p_v, p_a	Ventricular and the aortic pressure
δq	Heat exchange
q_v	Flow through the aorta
Re	Reynold number
Re_c	Critical Reynold number
SV	Stroke volume
t	Specimen thickness

t_B	Time at the end of the systolic positive pressure phase
t_C	Time at the beginning of the diastolic positive pressure phase
Δt	Time interval
T	Absolute temperature of the component
T_0	Room temperature
ΔT	Thermoelastic effect
u, v	Velocity components in x and y direction
U, V	Displacement components in x and y direction
U_M	Uncertainty related to the magnification factor
$U_{\Delta t}$	Uncertainty related to the laser pulse separation
$U_{\Delta X}$	Uncertainty related to the measurement
U_u	Uncertainty of the estimated velocity
v_{jet}	High velocity jet
v_{peak}	Mean peak velocity
v_z, v_{xy}	Velocity in flow direction and in the transversal plane
w	Specimen with
w_A, w_M	Segment lengths of Figure 23
Wo	Womersley number

Greek symbols

α	Coefficient of thermal expansion
α_A, α_M	Angle between the interface and the transversal section of the austenitic and martensitic region (in Figure 23)
α_i	Exponent of material parameter
ε_{ij}	Strain tensors
ε_L	Transformation strain (axial) associated with the austenite to martensite transformation
ε_{Lx}	Transversal transformation strain associated with the austenite to martensite transformation
$\varepsilon_{xx}, \varepsilon_{xy}, \varepsilon_{yy}$	Green-Lagrangian strain components
$\bar{\varepsilon}_{xx}, \bar{\varepsilon}_{yy}$	Mean strain on the selected ROI
θ_1	Angle of light incidence
θ_2	Angle of light refraction
$\bar{\lambda}_1, \bar{\lambda}_2, \bar{\lambda}_3$	Deviatoric principal stretches
μ_i	Moduli of material parameter
ν	Kinematic viscosity
ν_A	Poisson's ratio of the austenitic phase
ν_M	Poisson's ratio of the martensitic phase

ν_T	Poisson's ratio associated with the transformation
ρ	Material density
σ_E	Reference stress for Young modulus calculation (Equation 15)
σ_{ij}	Stress tensors
σ_{LPS}	Lower plateau strength (at 2.5 % of strain during)
σ_m	Mean value of the cyclic stress loading
$\Delta\sigma$	Variation of the cyclic stress loading
$\Delta\sigma_{ii}$	First stress invariant
σ_S^{AM}	Initial stress for the austenite to martensite phase transformation
σ_f^{AM}	Final stress for the austenite to martensite transformation
σ_{UPS}	Upper plateau strength (at 3 % of strain during loading)
σ_S^{MA}	Initial stress for the martensite to austenite phase transformation
σ_f^{MA}	Final stress for the martensite to austenite phase transformation
ϕ_1, ϕ_2, ϕ_3	Phases of the harmonic signal components
ω	Angular frequency

1. Introduction

Image Correlation techniques are full-field contactless optical techniques that, through correlation of pairs of images, allow to measure physical quantities of complex systems [1–4]. The movement of an object or fluid is obtained by measuring the tracer (speckle pattern, or particles seeding) displacement for each pair of sub-images. The application of these techniques to the investigation of complex structural and fluid-dynamics cardiovascular problems is increasing in popularity [5,6]. In the case of structural problems, they are used for characterisation of biomaterials such as biological soft tissues [7], biopolymers [8–10], and smart rigid materials such as Nitinol, which operate under large strains and exhibit complex non-linear constitutive relations [11–13]. These materials are particularly relevant for critical cardiovascular products [14], such as surgical and transcatheter cardiac valves, stents, cardiac patches and stent graft [15,16]. In particular, Nitinol is one of the most used material for endovascular stent, valvular plugs, transcatheter heart valves and device suitable for percutaneous procedures in general, whilst biological soft tissues and biopolymers are

used for valve leaflet and coatings. In the case of cardiovascular fluid dynamic applications, Image Correlation techniques allows to characterise the complex motion deriving by the interaction between pulsatile flows and deformable anatomical components or prostheses. This characterisation is particularly important because related to blood damage phenomena such as haemolysis and thrombosis [17,18], which may be responsible for devices or procedures failure.

This work investigates the use of Image Correlation techniques for the mechanical and hydrodynamic characterisation of complex devices and physiological systems, achieving a more complete understanding of their reliability, so as to maximise their reliability by proposing a number of innovative solutions that allow to improve and extend their applicability.

1.1 Thesis Outline

This thesis proposes and investigates the application of image correlation techniques in two main fields: the mechanical characterisation of complex biomaterials and materials for endovascular prostheses, and the characterisation of complex biofluid-dynamics.

In Chapter 2 the background and the basic knowledge of the employed methodologies are presented.

Chapter 3 describes the materials and methods used for both the two field studies. In particular, it first describes some common cardiovascular prosthetic devices and the features related with their materials (see section 3.1). Then three full field techniques

used for the characterisation are presented, namely: Digital Image Correlation (DIC), Particle Image Velocimetry (PIV) and Infrared Thermography (IRT) (in section 3.2). Finally, the fluid-dynamics apparatus used for the fluid-dynamics characterisation is described (in section 3.3).

Chapter 4 presents and discusses the research results. Section 4.1 focuses on the mechanical characterisation of Complex biomaterials, which have included a superelastic Nitinol grade under tensile static and cycle straining and the biaxial behaviour of biological soft tissue and biopolymers. Section 4.1.1.1 describes the contribution of DIC to enhance the mechanical characterisation of NiTi shape memory alloys. The study proposes and implements a new methodology to obtain more accurate parameters to define the constitutive behaviours of this class of materials. In section 4.1.1.2, the thermomechanical behaviour of Nitinol is further investigated by combining the DIC mapping with the measured temperature field, obtained with the use of an infrared camera. The study has focused on the thermomechanical heat sources activated during cyclic loading, including the Thermoelastic effect and the Elasto-caloric effects introduced by phase transformation. The original combination of DIC and IRT data, and the proposed frequency domain analysis of the acquired temperature, shows several potentials to further enhance the characterisation of the complex mechanical behaviour of such shape memory alloys. In section 4.1.2 the DIC technique is employed in demonstrating an improved biaxial characterisation protocol for soft materials. It is shown how the sample geometry and the gripping mechanism adopted in current standard biaxial tests may introduce some peculiar influences on the measured mechanical response, which hamper the evaluation of a truly intrinsic constitutive behaviour. The present section shows the results of a validation study of

some changes introduced in sample preparation, which can overcome some of the actual drawbacks in the current characterisation practice.

Section 4.2 covers Complex fluid-dynamics analysis. In section 4.2.1, the fluid-dynamics performance of the healthy aortic valve and the effect of its alteration are analysed. In Section 4.2.2 a complex case-study is reported, where the PIV technique is proposed in an original experimental setup specifically designed to provide a measure of the Effective Orifice Area in heart valves. This promising PIV analysis enabled to identify significant sources of error such as experimental feasibility and image distortion due to refractive index mismatching in-depth in Section 4.2.3. In particular, Section 4.2.3 examines the main experimental limitations related with the use of PIV to perform *in vitro* investigations of the hemodynamic behaviour of natural and artificial aortic valves. It is in particular enquired the intrinsic accuracy of the PIV technique and the influence of a number of experimentally related factors which may influence the interpretation of results. A number of solutions and approaches are also discussed, aimed at improving the interpretation of PIV results and thus expand the applicability of the techniques. In particular, in section 4.2.3.1, Smoothed-particle hydrodynamics (SPH) is proposed as a new method to generate *Synthetic Images* (PIV images generated using a random distribution of virtual tracer particles with a prescribed motion) for complex fluid-dynamics uncertainty quantification and test parameters setting. In section 4.2.3.2 a new blood equivalent is proposed to operate with a new optically transparent silicone with uncommonly low refractive index to address one drawback of the PIV technique related to optical distortion of collected images.

2. Background

2.1 Cardiovascular issues

Cardiovascular diseases are one of the main causes of premature mortality, and valvular diseases are one of the main contributing factors. These diseases, if not cured, may lead to heart failure. In this context prosthetic devices play a crucial role in restoring valve functioning, even if they have a number of side effects that have to be considered to choose the best solution for each patient. So, it is essential to maximise their safety and efficacy. This requires improvement in the characterisation of available materials, to exploit them to their full potential, reduce failure, and better understand the physiological environment when they operate in order to increase their efficacy and minimise disturbances.

For this purpose, research in Cardiovascular Engineering and in Bioengineering is developing ever more complex test systems that should allow a better comprehension of the Cardiovascular system details.

2.1.1 *Complex biomaterials*

Implants in their history were made with a lot of different materials, that have been changed with the research progresses. The principal and more complex materials used in cardiovascular implants are: biocompatible alloy, biological tissues, pyrolytic carbon and other synthetic materials such as polymers [19,20].

Previous studies on alloy materials have focused on materials with: an adequate biocompatibility, non-ferromagnetic behaviour (MRI safe), low wearing, non-corrosive, and high toughness. Titanium grade 5 (Ti6Al4V), Stainless-steel (AISI 816LVM), cobalt chromium alloy, Platinum iridium have proved the best match between strength, durability and biocompatibility.

These are all isotropic materials that can be characterized by following the standard ASTM E8 [21]. More recently a superelastic shape memory titanium alloy has become very popular because of its superelastic or shape memory behaviour. These properties, however, demand a more accurate characterisation. Previous research on nickel-titanium alloys focused on their thermal and mechanical characterisation through standard and fatigue tests [22,23]. However, the application of full-field techniques as DIC and IRT on nickel-titanium alloy reveals a phase inhomogeneity that may invalidate the basic assumptions on which standard materials characterisation of the mechanical response of the material is based.

A lot of implants use also biological soft tissues and rubber polymers for compliant parts. Their mechanical behaviours, due to their complex composition, usually requires biaxial tests. The mechanical characterisation of those material is

crucial for the design of a number of critical devices, such as heart valves, however a standard characterization is not available yet.

2.1.2 *Complex fluid-dynamics*

The heart is an organ composed of two positive displacement reciprocating pumps called left heart and right heart. Even if they are topologically parallel, their placement in the circulatory system is in series [24]. The right side moves the deoxygenated blood from the systemic system to the lungs and the left side moves the oxygenated blood from the lungs to the rest of the body [25]. The heart has four cavities connected with each other and with large vessels by unidirectional check valves: the Left Ventricle is connected with the Left Atrium by the mitral valve and with the Aorta by the Aortic valve. Instead, Right Ventricle is connected with the Right Atrium by the tricuspid valve and with the Pulmonary artery by the Pulmonary valve (heart sketch in Figure 1).

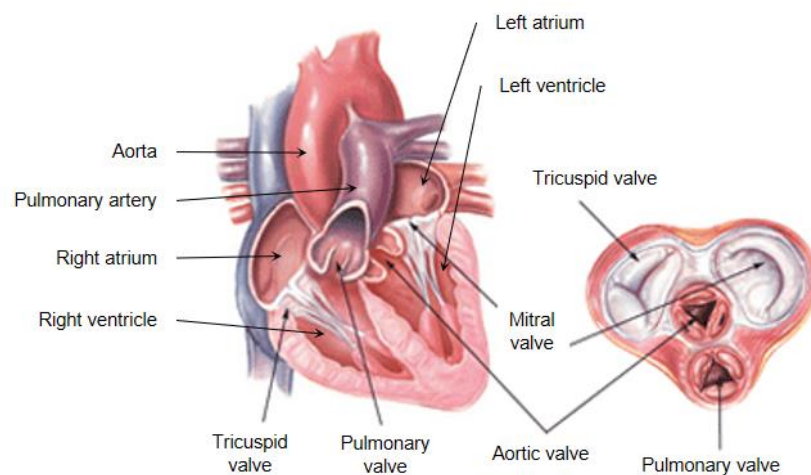


Figure 1 Sketch of the heart in sagittal and transversal section [26]

Because of the extreme cyclic loading (pressures in the left heart are five times higher than in the right heart), the valves of left heart are more affected to diseases than the right [27]. The function of the valves is to regulate and direct the flow during the cardiac cycle (in Figure 2). Starting with the left heart systole, the ventricle contracts rising the pressure of the ventricular blood. The mitral valves close when the ventricular pressure becomes greater than the atrial pressure and then, after an isovolumetric contraction, the aortic valve opens when ventricular pressure becomes greater than the aortic pressure and the aortic ejection phase begins. Then, after a period of ejection, the diastole starts with the ventricle relaxation that causes the aortic valve closure when the ventricular pressure becomes lower than the aortic pressure and, after a isovolumetric relaxation, the mitral valve opens when the ventricular pressure becomes lower than the atrial pressure.

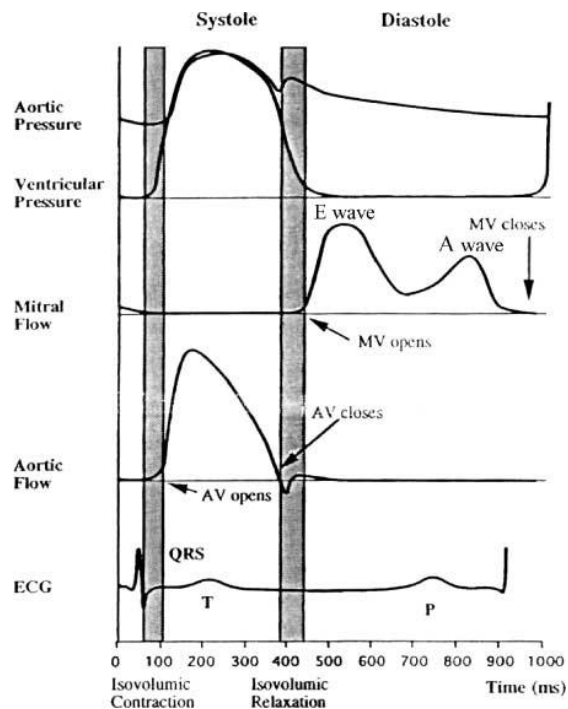


Figure 2 Left heart cardiac cycles [27]

The aortic valve is one of the most affected by diseases [28]. It is anatomically composed by three leaflets enclosed in three Valsalva sinuses (sketch in Figure 3). The leaflets are connected through the annulus to the heart wall and to the ascending aorta through the commissures. Valsalva sinuses are almost hemispherical bulges, and from two of which (left and right) the coronary artery originate [29].

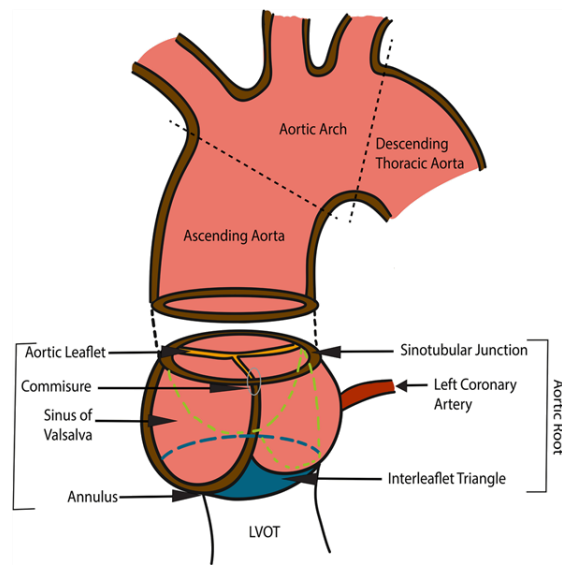


Figure 3 Sketch of the aortic root anatomy [30]

In the heart diseases valvular heart diseases are one of the most frequent heart diseases, due to its association with aging. In particular, the most common aortic disease is the aortic valve stenosis due to calcification [31]. Practically the valve calcification causes leaflet stiffening that hampers the physiological valve opening/closing, that causes reduction of aortic forward flow during systole and backflow during diastole. Instead, other common diseases are related to the aortic insufficiency [32]. It's often related to aortic root dilatation that may affect the proper valve function causing backflow during the diastole. Depending on the diseases and its severity the valve replacement or aortic valve-sparing could be the only treatment option.

3. Materials and Methods

3.1 Materials

3.1.1 Artificial heart valves

Artificial heart valves have the function to replace the native valve and its proper functioning. They comprise an occluding component (made of one or more parts), a housing, and an anchoring element. Artificial heart valves are usually classified depending on the basis of occluding component, and on their implantation method. In particular, they are principally classified in mechanical and biological valves that may be implanted with an open-heart surgery or a transcatheter surgery.

Mechanical prostheses are surgical valves that present the longest durability (exceeding the life expectancy of patient) and no calcification phenomena, but they are prone to thrombus formation and bleeding complications from anticoagulation [33]. Various types of valves have been implemented over the years: Ball-and-cage valves, Tilting-disk valves and Bileaflet valves.

The first generation comprised by a caged ball (see Figure 4 a) [34]. During the systolic period the ventricular pressure push the sphere, creating a gap through which the blood flows until the inversion of pressure, that pushes back the sphere, occluding the orifice and preventing the regurgitation of blood back to the ventricle. The blood in these valves has to flow around the ball, creating flow separation and recirculation regions, which caused a higher incidence of haemolysis [35].

The occluding component of tilting disc valve (in Figure 4 b) have, during the cardiac cycle, a floating disc that open laterally with an angle of 60-80°. In the open position the disc forms two orifice with different dimension and two flow jets with different velocity that induce a central recirculation and vorticity [36].

Most recent mechanical valve are the Bileaflet valve (in Figure 4 c), the first of which was St. Jude valve (in Figure 4 a). The St. Jude valve is composed by two leaflets made of tungsten impregnated with graphite, a cuff made of Dacron and a ring made of graphite coated with pyrolytic carbon [37]. The valve generates two lateral jet flows bigger than the central one. the Bileaflet result less thrombogenic than the tilting disc but still need anticoagulants treatments [38].

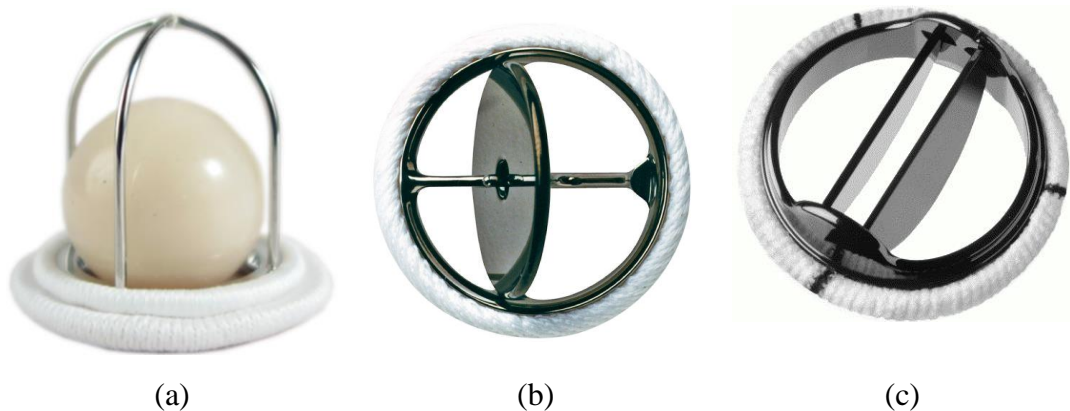


Figure 4 Mechanical valves: a) Ball-and-cage valve (Starr-Edwards) [39], b) tilting disc valve (Medtronic-Hall) [40], c) Bileaflet valve (St. Jude) [41]

Biological valves were introduced as an alternative to the mechanical one. In fact, biological valves are less thrombogenic and do not require life-long anticoagulant therapy. Although, those valves are plagued with leaflet calcification and leaflet laceration [36,42].

Biological valves are geometrically similar to the native valve, in fact present three leaflets with a central orifice and a flow jet that is much more similar to the native valve [27]. In the first cases of biological valve implantation, the patient's valve was replaced with cryo-treated human aortic valves from a donor (homograft) [36]. The advent of technique of tissue preservation, by using glutaraldehyde, led to develop valves made of animal tissues such as the porcine aortic valves or bovine pericardium. These are composed by a rigid or flexible stent, inside which the tissue is sutured to create the occluding leaflets (see Figure 5).



Figure 5 Porcine biological valve (Perimount) [43]

TAVI valves (in Figure 6) are indicated for all patients of advanced age and/or with comorbidity in which the open-heart surgery implies medium to high risk, because they allow to avoid surgery. The prosthesis is collapsed into a catheter that is inserted from a peripheral vessel as the femoral artery, then the valve is positioned inside the native valve. The first TAVI was a balloon-expandable valve (in Figure 6 a) [15,44]. The valve is composed by pericardial leaflets mounted onto a stainless-steel

stent. The crimped valve and the deflated balloon are fit onto a catheter, inserted into the body and guided to the heart. Once the proper location is reached, the valve is implanted through balloon expansion of the stent that pushes the native leaflets in the aortic root wall [45]. Many devices now, instead, use self-expanding approaches (in Figure 6 b). The valve is composed of pericardial leaflets mounted inside a Nitinol stent. The latter is crimped inside a sheath of the catheter, once in position is unsheathed and self-expands inside the native leaflets.

The two TAVI prostheses introduced are both recommended to be used interchangeably in most clinical situations [46]. However, from the beginning they have shown an increased incidence of cerebral ischemic events. These complications occur in the first days after device implantation, but the risk of stroke remain high for the first two months [15].

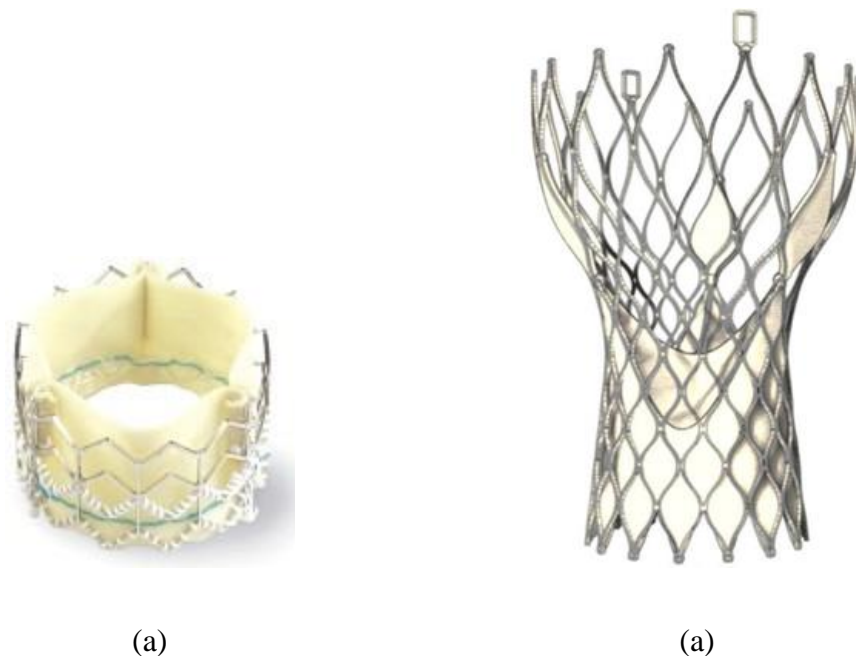


Figure 6 TAVI valves: a) balloon-expandable valve (Cribier valve) [47], b) self-expanding valve (Medtronic CoreValve) [5]

Most of the previous prostheses involve the use of biological tissues, in this application they have to operate in severe conditions, hence their mechanical characterisations are a crucial aspect to be investigated. Biological tissues composition is multilayer. The outer layer of pericardium is composed of layers of collagen fibrils and elastin fibres [48]. Pericardium and a lot of other biological tissues have a J-curve relationship between stress and strain [49]. Their characterisation can be carried out through uniaxial testing following the British Standard [50,51] or through biaxial testing that, although more indicated for materials of this nature, has no standard test to be followed yet.

3.1.2 *Nitinol*

Nitinol is a nearly equiatomic Nickel-Titanium alloy that has unique mechanical behaviour depending on its composition, temperature and level of stress. In particular, Nitinol has two different crystalline phase structures: Martensite and Austenite. The first phase is characterised by a monoclinic crystal, stable at low temperature and high stress levels; the second is characterized by a body-centered cubic crystal, stable at high temperature and at low stress levels [52].

Hence, the phase transformation can occur thermally, with heat transfer or absorption, or mechanically, by applying a certain stress level [53]. The phase at the operating temperature depends on the transformation temperature value. When the operating temperature is lower than the transformation one, twinned Martensite is stable and the behaviour of the material is governed by the shape memory effect [54,55], in which deformed Nitinol, in its detwinned Martensitic configuration, can

recover the original shape if heated up to the transition temperature (see Figure 7). Instead, when the operating temperature is higher than the transformation one, the nitinol behaviour is superelastic and austenitic Nitinol, when subjected to high levels of stress, transforms into detwinned martensite before reaching a yield point, exhibiting a significant deformation during such transformation. If the stress in martensitic state is kept below the yield stress, the material returns to the austenitic phase, recovering the large strains accumulated in the previous loading stage (see Figure 7).

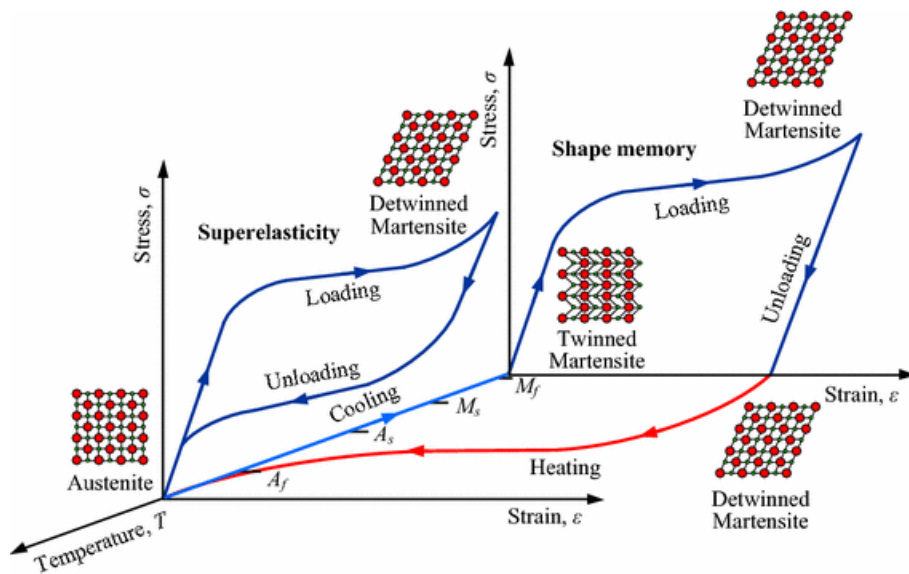


Figure 7 Nitinol behaviours [56]

The shape memory behaviour is widely used for industrial application as actuators [57], instead the superelastic behaviour is mostly used in medical application as stent, cardiovascular valves, etc., where the ability of these medical devices to undergo reversible high deformations is a key beneficial feature [58].

Because of its complex nature, Nitinol characterisation is a complex task. In this work, Digital Image Correlation and Infrared Thermography based methods were applied on nitinol strips undergoing tensile cycles, in order to investigate its

mechanical behaviour and improve current characterisation approaches. The full-field nature of the proposed techniques is in particular exploited to better investigate the non-homogeneous responses of the material.

3.2 Experimental Techniques

3.2.1 Cross-correlation based

Various techniques based on Cross Correlation function have been proposed for their feature like: non-intrusive, indirect and full-field. They are optical techniques that don't need contact, measure the movement of an object/flow by monitoring the tracer motion and moreover by dividing the images in subsets a full-field information can be obtained. Those characteristics make such techniques particularly suitable for complex systems.

In particular, they are based on the comparison of a sequence of images of an object/flow. In the 2D setup a monochromatic digital camera is placed perpendicularly to the observation plane, acquiring a sequence of images [59]. Each image is represented by a matrix of values in the grey scale, which codes the mean light intensity framed from each pixel sensor. In fact, each matrix cell corresponds to a pixel and contains a number between 0 (black) and 255 (white) that respectively corresponds to maximum dark light and maximum bright light. The image is divided into small groups of pixels (called subsets or interrogation regions) which is subjected to an automatic detection of the "tracer" movement. The tracer is a component placed on an object surface or immersed in a fluid flow clearly identifiable in shape and position [60]. During the automatic

detection the tracer is identified in the first image (or sub-image) and then it is recognized in the following image. The comparison of the tracer position in both images, knowing the time acquisition, allows to identify its movement that is directly related to flow velocity or object deformation.

To perform automatic detection a correlation functions is used, it may take several forms. For example, in equation 1 a basic function is reported. Where the difference in light distribution between the initial sub-image and a tentative sub-image in the final image is compared.

$$C(x, y, U, V) = \sum_{\Delta x, \Delta y = -p/2}^{p/2} [I(x + \Delta x, y + \Delta y) - I^*(x + U + \Delta x, y + V + \Delta y)]^2 \quad 1$$

where p is the subset dimension, x and y are the P coordinates (central point of the sub-image), I and I^* are the light intensity of each pixel respectively of the reference sub-image and the investigated sub-image, and U and V are the unknown P displacement.

Practically the cross-correlation function is used to find the tracer in its final configuration by finding the sub-image (in a set of tentative) with the same light intensity of the reference one. When a correlation function is expressed as a sum of squared differences, like in equation 1, then the optimum displacement variables are obtained as those minimising the correlation function, i.e. the best correlation is represented by the minimum. Correlation function may be defined by summation of sum of squared, where the best correlation is represented by the maximum of the correlation function.

3.2.1.1 DIC

Digital Image Correlation is a non-contact optical technique (DIC) that allows to obtain displacement and strain fields of components undergoing deformation by using image processing algorithms. In the case of in plane deformation, the bi-dimensional technique (DIC/2D) can be applied, monitoring the surface component with a single camera. In particular, the DIC/2D setup requires a specimen with a random speckle pattern on its surface of investigation, a camera with the optical axis perpendicular to the specimen surface, a loading system, and a fixed light source. The specimen motion is monitored by acquiring pictures of the pattern at regular time intervals. The sequence of pictures is processed by means of cross-correlation algorithms, that partitions the picture into small equidistant subsets, defines the pattern of each subset in the first image and find the final configuration with the same distribution of intensity. The subset displacement, knowing the period of acquisition, provides the displacement of the subset central point. The resolution of the displacement/strains maps depends on the subset spacing chosen (distance between the central points of two adjacent subsets) [59].

As mentioned in section 3.2.1, the correlation function in equation 1 is a simplified version where the tentative subset can be found only among subsets which maintain the same initial square shape (case of rigid body motion) and the displacements have a pixel resolution (case of pixel tracking).

Furthermore, in order to represent more closely the deformation, the subset defined in the first image during the correlation is: translated, rotated and deformed in order to find with greater accuracy the best match. Another fundamental step to

achieve a sub-pixel accuracy, is the need to obtain a continuous grayscale distribution from the original pixelated one, by means of interpolation procedures such as bi-cubic bi-spline interpolations of light distribution. These two steps end up in a non-linear optimisation of the correlation function, that requires some more advanced optimisation algorithms.

The method accuracy relies on the subset speckle distribution uniqueness. This feature depends on the ratio between subset dimension and speckle dimension and on the speckle distribution itself. In fact, to apply the technique, the material surface should present a random speckle pattern. The latter may arise from the natural texture or microstructure of the material or can be artificially applied by painting or etching the surface (shown in Figure 8).

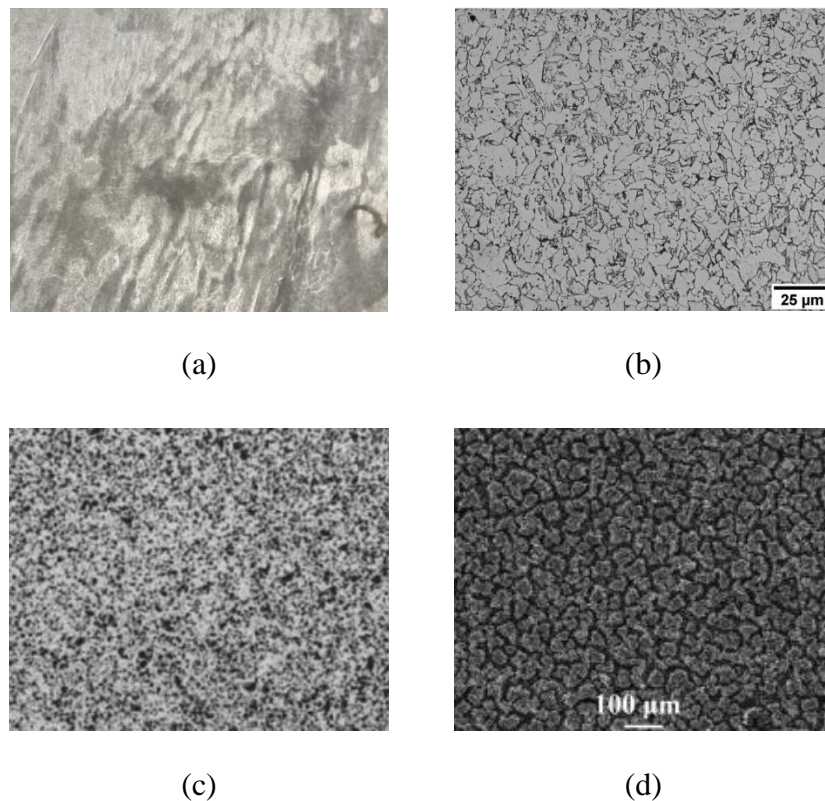


Figure 8 a) bovine pericardium natural pattern, b) C-Mn steel metal microstructure[61], c) black and white painted spackel[2], d) etched aluminium alloy[62]

The speckle in order to minimize false positive correlation, has to be:

- Not repetitive,
- Isotropic,
- With a high level of contrast.

In this work, biomaterials were mechanically characterized by applying a 2D DIC technique. In particular the Ncorr [3] freeware software was used.

Ncorr is a Matlab based open-source program that implements a digital image correlation analysis to a sequence of picture. The Ncorr algorithm uses circularly shaped subsets, applying two different correlation stages: an initial guess and a more refined optimisation of a normalized cross correlation function (see Figure 9). The initial guess, keeping the subset undeformed, thus yields U and V with integer (pixel) accuracy. The next step uses a nonlinear optimizer to refine these results with sub-pixel resolution by finding the minimum of a correlation function expressed in the form of equation 2:

$$C = \sum \left[\frac{I(\tilde{x}, \tilde{y}) - I_m}{\sqrt{\sum [I^*(\tilde{x}, \tilde{y}) - I_m]^2}} - \frac{I^*(\tilde{x}^*, \tilde{y}^*) - I_m^*}{\sqrt{\sum [I^*(\tilde{x}^*, \tilde{y}^*) - I_m^*]^2}} \right]^2 \quad 2$$

where I_m and I_m^* correspond to the mean grayscale values of the reference and current subset, (\tilde{x}, \tilde{y}) and $(\tilde{x}^*, \tilde{y}^*)$ are the coordinates of a reference and deformed current subset point.

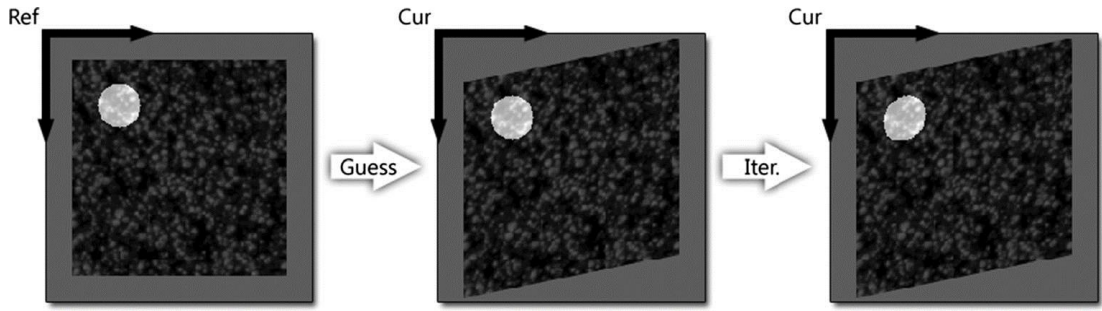


Figure 9 The basic steps of the Ncorr algorithm correlation [3]

After the second step of correlation the Green-Lagrangian strain are calculated from the displacement, as in equations 3,4 and 5.

$$\varepsilon_{xx} = \frac{1}{2} \left(2 \frac{\partial U}{\partial x} + \left(\frac{\partial U}{\partial x} \right)^2 + \left(\frac{\partial V}{\partial x} \right)^2 \right) \quad 3$$

$$\varepsilon_{xy} = \frac{1}{2} \left(\frac{\partial U}{\partial y} + \frac{\partial V}{\partial x} + \frac{\partial U}{\partial x} \frac{\partial U}{\partial y} + \frac{\partial V}{\partial x} \frac{\partial V}{\partial y} \right) \quad 4$$

$$\varepsilon_{yy} = \frac{1}{2} \left(2 \frac{\partial V}{\partial y} + \left(\frac{\partial U}{\partial y} \right)^2 + \left(\frac{\partial V}{\partial y} \right)^2 \right) \quad 5$$

in which the strain is calculated as a composition of displacement differentiation. The differentiation is particularly sensitive to noise, this means that any displacement noise is magnified in the strain fields. Hence, in order to smoother the strain results a least squares plane fit of the displacements is first applied, over an area called Virtual Strain Gauge (VSG). The latter calculates the displacements gradients on a selected number of displacement data, whose extension depends on the choice of the VSG size. The displacement gradients are then replaced into equations 3,4 and 5 to determine the strain in the plane ε_{xx} , ε_{xy} and ε_{yy} . The strain map is then obtained in matrix form and can be exported for further post-processing, e.g. in the Matlab environment.

3.2.1.2 PIV

Particle Image Velocimetry (PIV) is a technique that allows to capture velocity information of whole flow fields in time or phase resolution [1]. Time-resolved PIV allow to measure the temporal evolution of a flow field, its 2D system is usually composed by a high-speed camera and a continuous laser. Instead, phase-resolved PIV system composed of a Double-pulse Laser and a camera (setup in Figure 10) is used to study specific instant of a periodic flow. The test fluid shall consist of an optically transparent liquid, seeded with neutrally buoyant particles of dimension 9-13 μm , these are selectively illuminated on a plane with a laser sheet at two time instants separated by an interval Δt of the order of microsecond. The light scattered by the particles located in the fields of view (FOV) is recorded in a sequence of frames by a camera, situated perpendicular to the laser sheet. In order to avoid blurring of the image, laser pulse duration must be short enough to “freeze” the motion of the particles during the pulse exposure. Furthermore, the time interval Δt has to be long enough to be able to determine the particles displacement in the sequence of image and short enough to do not let particles moving away from the FOV.

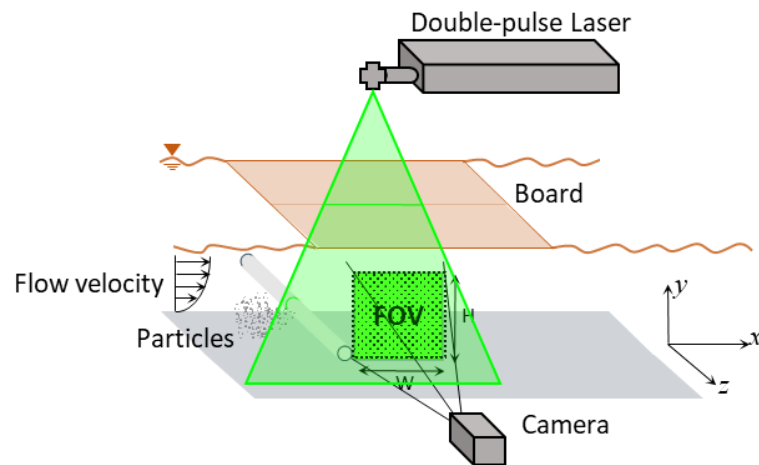


Figure 10 PIV 2D setup [63]

The acquired pictures are correlated with a correlation method similar to that described in the previous section applied to small part of the image (interrogation region). The first image (Frame A in Figure 11a) is subdivided in small interrogation regions (IR) with equal pixel dimension equally spaced. Each IR has a random distribution of particles captured as light dot in a dark background. The correlation method, in the following image (Frame B in Figure 11a), moves IR around in the neighbourhood, finding for each position a maximum value of the correlation function in equation 6, as its shown in Figure 11b [63–65].

$$C(i^*, j^*) = \sum_i \sum_j I(i, j) \cdot I^*(i - i^*, j - j^*) \quad 6$$

where i and j are the coordinate of the reference IR, i^* and j^* are the coordinate of the current IR.

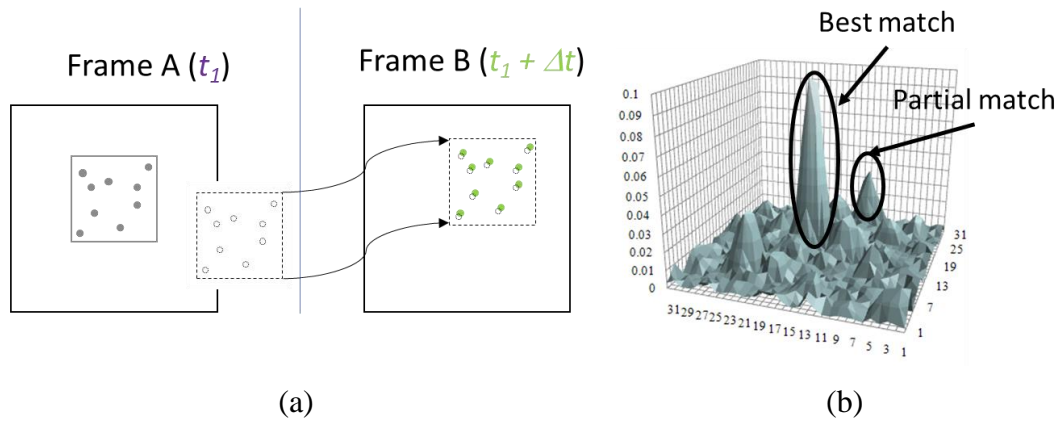


Figure 11 a) IR match during correlation, b) peak finding [63]

That function finds, by comparing images grey intensity, small peak in case of partial overlap and a big peak for the best match. When the best match is found, the IR displacement and velocity are calculated. All the vectors, calculated for each IR, are then compared. If a vector is too long/short compared with the neighbours, it is considered invalid and, in the postprocessing, is recalculated as the mean value of the

neighbours. All the valid and recalculated vectors are then mediated. In order to reduce noise errors, mean operation is applied on a certain number of acquisitions of the same instant of the period.

In this work, two different PIV algorithms were used in two ways. In a first study to validate PIV methods by means of *synthetic images* PIVlab was used (in section 4.2.3.1) [66]. In a second study, aimed at measuring experimentally Effective Orifice Area of heart valves, a PIV2D TSI system was used (in section 0). TSI system is composed by a Double-pulse laser (wavelength of 532 nm), a camera, a synchronizer (with a trigger port) and its own software Insight4G for acquisition and processing. Insight4G software and PIVlab apply a cross-correlation method for the image processing to identify the best match and calculate the velocity vector.

PIVlab is an open source Matlab program that allow to analyse external PIV images [4,66]. The code consists in four main steps: image input, ROI selection, pre-processing, image evaluation, and vector validation. Image input enables to charge external image organized in pair (image A and image B). ROI selection allows to select an image portion where the evaluation have to be applied speeding up the whole image processing. Image pre-processing is usually applied to increase the contrast between the particles and the background by using different techniques that enhance the image quality. Then image evaluation applies the cross-correlation algorithm on each IR. It can be applied with a direct cross-correlation (DCC) or a discrete Fourier transformation (DFT). The DCC approach apply the correlation in the spatial domain, instead the DFT ones compute the correlation in the frequency domain [65]. Even if the DCC shows a more accurate results compared with the DFT [67], DCC needs

higher computation costs that can be offset by executing several times the DFT approaches [68]. In fact, the DFT approaches is implemented to apply one to four times the correlation specifying for each pass the dimension of the IR. In those passes the deformation of the IR is also considered by applying a regular DFT analysis to find the centre of the IR. Then the IR deformation is calculated in the following passes. The image evaluation ends with the peak finding procedure that detect the peak of correlation by applying a Gaussian function to the IR position finding the sub-pixel peak position. When the peak position is known the velocity vectors are calculated using the spatial calibration and time step inserted from the user. Then, as last step the vector validation is performed to obtain reliable results. In this step the outline vectors are removed by applying a threshold and the removed vectors are replaced by interpolation of the neighbourhood. The vectors were then exported in Matlab for further investigation.

Insight4G software included in the TSI system apply a cross-correlation method to the images acquired with the TSI system. The analysis steps are: mask, image pre-processing, cross-correlation processing and post-processing. Mask selection allows to delimit the ROI to be processed. Image pre-processing modify the images through the application of different kind of filters or operations chosen depending on the acquired images. In particular, in the following sections image filter was applied performing a low-pass filter that replace the intensity of each pixel by the mean intensity of its neighbourhood. Then, a multi-pass processing was performed. It consists in a first processing pass that compute the vector field of the defined interrogation region. The result of the first processing is used to optimize the second processing pass. At last, a post-processing is applied on the vector field. This function

filters out the spurious vectors and fill the removed vectors through interpolation of the neighbourhood vectors. The mean operation was made in Tecplot [69], a post processing program used to make further calculation and present the results.

3.2.2 *Thermal based*

3.2.2.1 *IRT*

Measurements of temperature fields by means of Infrared Cameras have achieved a significant level of performance, due to the progresses in Infrared sensors and Imaging. Modern focal plane array cooled sensors, for instance, are able to acquire high-resolution images (e.g. 600x500 pixels) at very high frame rates (e.g. up to 200 Hz) with a high thermal resolution, expressed in terms of Noise Equivalent Temperature Difference, NETD (typical values of 18 Mk). Furthermore, Infrared cameras operate as non-contact sensors, provide full-frame data, do not require complex sample surface treatments and are relatively easy to setup in a laboratory environment.

Infrared Thermography (IRT), in particular, monitors the temperature in a time interval. The approach followed to sample the temperature and to evaluate the harmonic content of the acquired thermal history is based on a technique generally known as Thermoelastic Stress Analysis (TSA). This is an experimental technique that provides information on the surface stress field by recalling the Thermoelastic Effect [70]. This considers the temperature changes induced by the elastic components of the deformation. The temperature variation is associated with the volume variation under elastic straining, such that a material warms up when it is squeezed (negative volume

change due to compression) and cools down when it is stretched (positive volume change under traction). Common materials, subjected to a change in elastic strain, experience only small temperature changes (of the order of 1 mK) [59].

A useful analytical formulation of the Thermoelastic law can be derived by starting from the Biot state equation [71], written in the form reported in equation 7, which describes the relationship between the temperature change with the stress-strain variation:

$$dT = \frac{T}{\rho \cdot c_v} \cdot \frac{\partial \sigma_{ij}}{\partial T} \cdot d\varepsilon_{ij} + \frac{\delta q}{c_v} \quad 7$$

where T is the absolute temperature of the component, ρ is the density, c_v is the specific heat at constant volume change, δq is the heat exchanged between the system and the environment, σ_{ij} and ε_{ij} are respectively the stress and strain tensors.

Under the assumptions of:

- homogeneous and isotropic material;
- physical and elastic properties of the material remain constant within the small range of temperature changes;
- linear elastic Hookean behaviour;
- adiabatic transformation.

Equation 7, integrated over a finite stress interval $\Delta\sigma_{ii}$, and replacing strain components in terms of stress components, can be written as:

$$\Delta T = -T_0 \cdot K \cdot \Delta\sigma_{ii} \quad 8$$

where T_0 is the room temperature and K is the thermoelastic constant of the material, equal to $\frac{\alpha}{\rho \cdot c_p}$, in which α is the coefficient of thermal expansion and c_p is the specific heat at constant pressure.

Adiabatic conditions are usually obtained applying cyclic loads. This allows to obtain the thermoelastic effect ΔT , filtering the harmonic content of the sampled temperature. In particular, the thermoelastic signal ΔT is obtained by evaluating the amplitude of the harmonic term of temperature, that is modulated at the loading frequency. This filtering procedure, also called lock-in correlation, is able to provide a higher resolution threshold than that of the native NETD of the IR camera, with values of $\Delta T = 1$ mK typically achievable.

For materials that satisfy the conditions previously introduced, equation 8 allows to find the full-field surface distribution of the first stress invariant, i.e. $\sigma_x + \sigma_y$, with little limitations on the complexity of the analysed structures and on the type of material analysed. On the other hand, TSA requires a cyclic or dynamic loading able to introduce adiabatic conditions, and therefore is a technique particularly suitable for applications in fatigue studies and fatigue characterisations of materials and structures.

When physical and elastic properties of the material cannot be considered as temperature independent, equation 8 becomes more complex, since the derivative of the stress tensor with respect to temperature cannot neglect the derivatives of the material parameters. By carrying out the analytical derivation with these derivatives, a more complex thermoelastic law is obtained, called the second-order theory [72,73], where the dependence of elastic parameters from the temperature is not neglected. By

considering a cyclic uniaxial stress loading $\sigma = \sigma_m + \Delta\sigma \cdot \sin(\omega t + \varphi)$, equation 7 becomes:

$$\Delta T = -T_0(K_0 - K_1\sigma_m)\Delta\sigma \cdot \sin(\omega t) - T_0 \frac{K_1}{4} (\Delta\sigma)^2 \cos(2\omega t) \quad 9$$

where: $K_0 = \frac{\alpha}{\rho \cdot c_s}$; $K_1 = \frac{1}{\rho \cdot c_s} \frac{1}{E^2} \frac{\partial E}{\partial T}$.

In equation 9, the stress and temperature variations are not linearly dependent. In fact, a temperature variation at twice the load frequency arises and is usually referred to a Second Harmonic term. Furthermore, by considering the First Harmonic term, i.e. the one at the load frequency, this now depends also on the applied mean stress σ_m , and the relative temperature variation can become in phase with the load, if $K_1\sigma_m > K_0$.

In the present work, IRT and TSA techniques were applied on Nitinol to investigate the thermal responses of the material.

3.3 Experimental Apparatus

3.3.1 Pulse Duplicator system

The ViVitro system (ViVitro Superpump System SP7084, ViVitro, Victoria, BC, Canada) is a pulse duplicator apparatus that allow to reproduce physiological heart condition of half heart (in Figure 12). It is based on the 2-element Windkessel model in which the systemic arterial system is modelled as a circuit. Its electrical analogue involves a capacitor and a resistance placed in parallel that represent respectively the arterial compliance and the peripheral resistance [74,75]. The arterial compliance takes

into account the elasticity and extensibility of the arterial tissues, instead the peripheral resistance is the resistance found by the blood in its flowing. Furthermore, by using a blood analogue with equivalent density and viscosity the blood inertia can be taken into account [76]. In the ViVitro hydraulic system the compliances (aortic and systemic) are modelled as air pocket in a filled system, and the resistance is modelled with an adjustable pipe restriction.

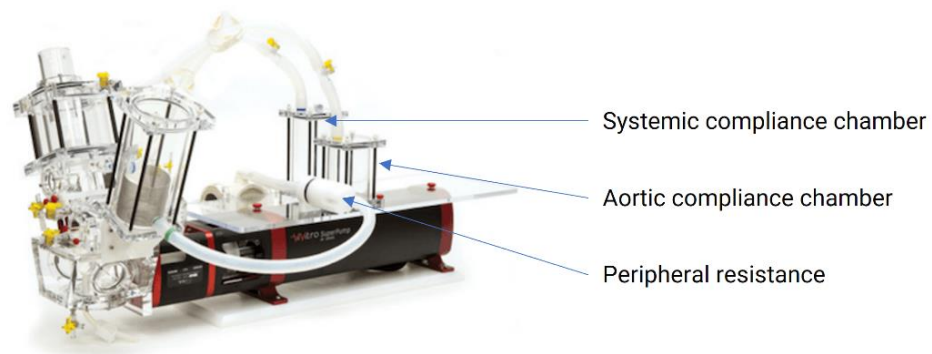


Figure 12 ViVitro pulse duplicator system [77]

ViVitro system is composed by three optically transparent cardiac chambers connected by one-way valves, as in the human heart. The pulsatile flow is regulated by a servo controlled volumetric pump that cyclically compresses and releases a silicone mock ventricle, by pressing the liquid placed in an external chamber communicant with the pump. When it is used as left heart, the ventricle communicates with the outlet chamber through the aortic valve, and with the atrium through the mitral valve (sketch in Figure 13). Moreover, the aortic chamber is connected to two external compliance that mimic the systemic compliance and the aortic compliance. The system is instrumented with pressure transducers (Utah Medical 6069 Pressure Transducers) in all cardiac chambers and an electromagnetic flowmeter (Carolina Medical flowmeter), indicated in Figure 13. The flowmeter probe, at the inlet of the aortic

valve, contains an electromagnet that produce an electromatic field across the vessel. The fluid motion is identified because generates in the magnetic field an induced voltage proportional to velocity. To reach experimental condition of Cardiac Output (CO) and Mean Aortic Pressure the peripheral resistance allows to change the aortic pressure and the Vivitest software allows to control the stroke waveform of the piston.

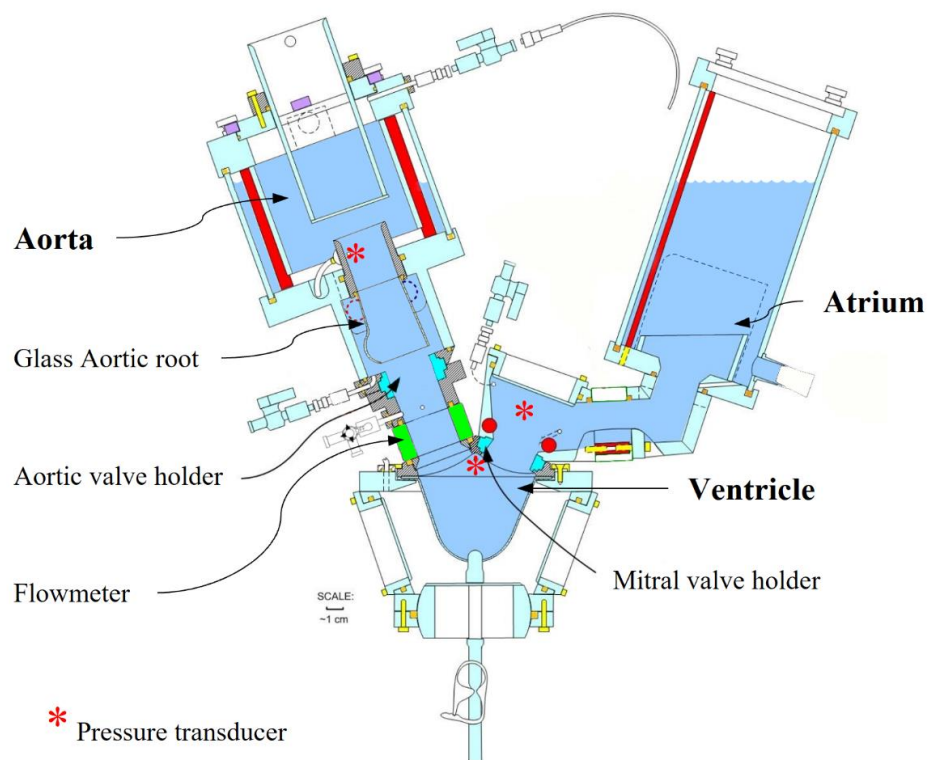


Figure 13 Pulse duplicator system diagram [77]

In Figure 14 it is reported an example of data acquisition in an experiment where a St. Jude mechanical valve of size 29 mm was inserted as mitral valve (in Figure 4c) and a Perimount biological valve of diameter 23 mm (in Figure 5) was inserted as aortic valve. A FDA waveform that simulate physiological strokes (including atrial contraction) is used. In particular, are reported the pressure curve (Atrial, Ventricular and Aortic pressure), the Flow curve divided in 4 period, are reported.

Flow period:

- I. Identifies the beginning of the systolic forward flow;
- II. Identifies the end of the systolic forward flow and the beginning of closing;
- III. Identifies the end of closing regurgitation and the beginning of leakage;
- IV. Identifies the end of leakage (correspond to marker I for the following cycle).

Pressure period:

- A. Identifies the beginning of the systolic positive pressure phase;
- B. Identifies the end of the systolic positive pressure phase;
- C. Identifies the beginning of the diastolic positive pressure phase;
- D. Identifies the end of the diastolic positive pressure phase.

In Figure 14 the heart phases described in 2.1.2 (Figure 2) can be observed.

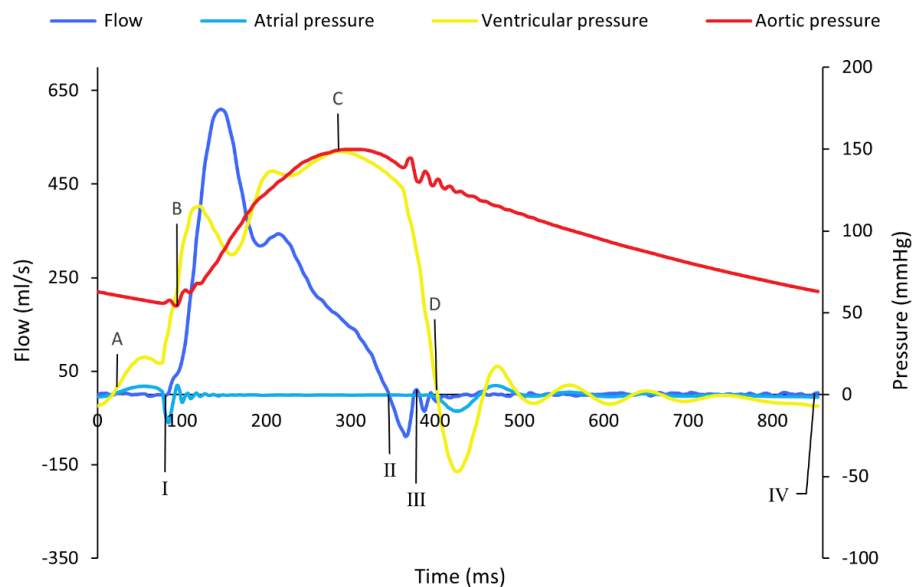


Figure 14 Pulse duplicator data output

From the curves in Figure 14, following the standard ISO5840 [78], performance parameters can be obtained. In particular, the parameters identified as more significant:

- Mean Systolic Transvalvular Pressure Drop Δp ,

It is an indicator of systolic valve performance calculated from the mean value of pressure difference across the aortic valve (between B and C) as in equation 10

$$\Delta p = \frac{\int_B^C (p_v - p_a) dt}{t_C - t_B} \quad 10$$

where p_v and p_a are respectively the ventricular and the aortic pressure, t_C is the time at the beginning of the diastolic positive pressure phase and t_B is the time at the end of the systolic positive pressure phase

- Effective Orifice Area EOA

It is representative of the cross section at the *vena contracta*, and is calculated by the Gorlin equation [79]:

$$EOA = \frac{q_{vRMS}}{51.6 \sqrt{\frac{\Delta p}{\rho}}} \quad 11$$

in which q_{vRMS} is the root mean square forward flow and ρ is the density of the test fluid

- Closing and Leakage regurgitant Volume

It indicates the amount of back flow during the Closing period (II-III) and the Leakage period (III-IV), calculated as the integral of the flow curve during the respective period

- Forward, Closing and Leakage Energy loss

They are calculated respectively in equation 12, 13 and 14

$$E_f = 0.1333 \int_I^{II} \Delta p \cdot q_v(t) dt \quad 12$$

$$E_c = 0.1333 \int_{II}^{III} \Delta p \cdot q_v(t) dt \quad 13$$

$$E_l = 0.1333 \int_{III}^{IV} \Delta p \cdot q_v(t) dt \quad 14$$

Where 0.1333 is a conversion coefficient from mmHg to mJ, $q_v(t)$ is the instantaneous flow at time t .

4. Cardiovascular prostheses applications

4.1 Complex biomaterials

4.1.1 Nitinol characterisation

Thanks to its unique behaviour characterised by a superelastic response, Nitinol has now become the material of preference in a number of critical applications, especially in the area of medical implants. However, the reversible phase transformation producing its exceptional behaviour is also responsible for a number of phenomena that make its mechanical characterisation particularly complex. This necessarily reduces the level of safety and design optimization of current applications, which rely on substantially approximate mechanical parameters. In this study, the mechanical and thermo-mechanical behaviours are analysed by means of a simultaneous application of digital image correlations (DIC) and Thermoelastic Stress Analysis (TSA).

4.1.1.1 Mechanical characterisation (DIC)

Thanks to its unique properties and its biocompatibility, Nitinol has now established as a material of preference in a number of medical devices including cardiovascular, orthopaedic and orthodontic implants [80].

The criticality of these applications, which demands the highest level of safety and design optimisation, requires the accurate characterisation of the material mechanical behaviour at the working temperatures. This is normally achieved by means of uniaxial tension testing, and based regulatory standards such as the ASTM E8 [21], which describes the methods for tension testing of homogeneous and isotropic metals. In the case of the assessment of superelastic Nitinol alloy, this is integrated by the ASTM F2516 [23], which provides additional details for the extraction of the upper and lower plateau strength and residual elongation from the test data.

Although these tests are based on the assumption of homogeneity, previous studies have observed that when the super-elastic behaviour is exhibited during the test, the phase transformation is localised and moves to progressively involve the whole sample area. Therefore, during this stage, the specimens comprise regions with different crystal structures and mechanical properties. In fact, the material superelastic behaviour is the result of a stress-induced phase transformation from austenite to martensite, which initiates at localised Lüders bands [81,82]. These regions, characterised by very large strains of the order of 6-8 % [83], progressively expand with the specimen elongation, until the entire gauge length has transformed. This invalidates the assumption of homogeneity of the test material, potentially reducing the reliability of the information obtained from standard tension testing.

As a consequence, test results commonly used to characterise Nitinol need to be reinterpreted to determine if and how they can still provide quantitative parameters suitable to describe the mechanical behaviour of the material. This work presents an analysis of the phenomena occurring in a Nitinol plate specimen during quasi-static uniaxial tension testing in the super-elastic region, by means of digital image correlation (DIC).

Test setup

A test specimen was obtained from a Nitinol plate (0.2 mm thick, 6.35 mm large and 35 mm high) of transformation temperature equal to 13 °C, as determined from differential scanning calorimetry analysis. A black random speckle was applied with an airbrush on one side of the plate specimen, previously painted white (the specimen surface is shown in Figure 15). The sample was tested on a uniaxial electromechanical testing machine Instron 3367, at room temperature (20 °C), at which the super-elastic behaviour is exhibited. Displacement was applied through load-unload cycles, with a sequence of quasi-static triangular waves, at a cross-head speed of 0.5 mm/min. Progressively increasing peaks of deformation, raising of 1 % at each cycle, were applied, monitoring the stress-strain diagram in order to arrest the applied deformation at the lowest percentage integer ensuring that the stress-induced martensitic transformation for the whole gauge length was achieved (i.e. the upper transformation plateau is completed). The analysis was then performed on the final cycle.

The specimen was monitored during the test with a Reflex Nikon D5100 camera, equipped with a Macro lens (AF-S VR Micro-Nikkor 105mm f/2.8G IF-ED), used to acquire pictures of the painted face of the specimen plate at every 3 seconds. These

images were used to determine the displacement and the strain on the specimen surface by means of 2D DIC [2].

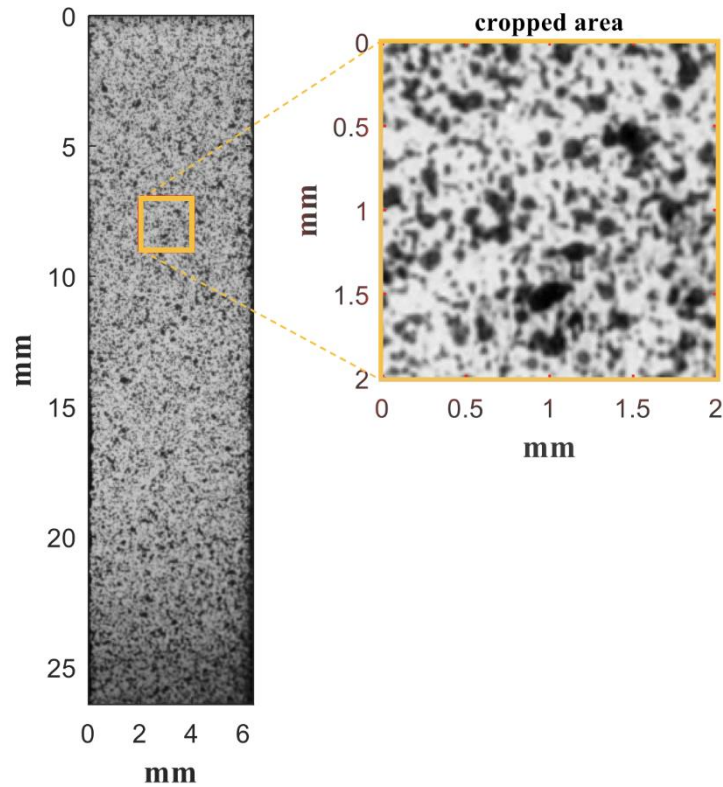


Figure 15 Specimen speckle surface

Standard analysis

For the standard analysis, strains were calculated from the crosshead displacement and stresses as force measured by the load-cell, divided by initial cross-sectional area.

In compliance with the ASTM F2516–14 guidance [23] the upper plateau strength σ_{UPS} was measured as the stress at 3 % of strain during the loading of the sample, and the lower plateau strength σ_{LPS} as the stress at 2.5 % of strain during the unloading of the sample.

The Young's moduli of the austenitic and martensitic phases were calculated by fitting the modulus line to the fully transformed stress-strain curves (i.e. before and after the transformation plateaus) by least-squares regression analyses. As the regions close to the upper and lower plateaus initiation are characterised by significant departures from linearity, the austenitic Young's modulus was calculated on the portion of the loading curve up to a stress σ_E , at $\frac{3}{4}$ between σ_{LPS} and σ_{UPS} :

$$\sigma_E = \sigma_{LPS} + \frac{3}{4}(\sigma_{UPS} - \sigma_{LPS}) \quad 15$$

Similarly, the martensitic modulus was calculated on the portion of the unloading curve from the maximum applied stress to σ_E .

For the determination of the mechanical parameters, the plateau curves were fitted with straight lines, as per standard practice [84,85] by least-squares regression analyses. The initial and final transformation stresses between the two crystal phases (namely, the initial stress for the austenite to martensite phase transformation σ_s^{AM} ; the final stress for the austenite to martensite phase transformation σ_f^{AM} ; the initial stress for the martensite to austenite phase transformation σ_s^{MA} ; and the initial stress for the martensite to austenite phase transformation σ_f^{MA}) were obtained from the intersection between these lines and those used to fit the regions where the Young's moduli were estimated. The intersection points at the ends of the upper plateau were used to determine the transformation strain associated with the austenite to martensite transformation ε_L .

DIC analysis

For the local mechanical response DIC analyses was applied. As previously mentioned, the usual stress and strain calculation described above does not take into consideration the inhomogeneity due to the presence of local regions of different material phases, which nucleate in Lüders bands and progressively expand to occupy the entire gauge length [86]. The strain maps determined applying DIC on Nitinol can overcome this issue, as they are able to clearly identify the regions where the specimen is in the austenitic and martensitic phase, with the latter characterised by much higher strain levels [2]. However, these are not free from the limitations intrinsic in the technique and in the specific experiment. In fact, evaluation of deformation in DIC is based on the assumption of continuity of displacements over the surface, which makes it unsuitable to provide accurate data in regions where there are discontinuities [87]. Moreover, when the analysis is performed in the transformation regions separating the austenitic and martensitic portions, these keep changing between the successive images that are used to perform the correlation. This results in the presence of a thin band (typically of a few tenths of a millimetre) at the interface between the austenitic and martensitic phases, characterised by a gradual variation between the strains identifying the two regions. This appears clear in Figure 16, where the propagation of the front of phase transition between two successive images is represented together with the regions where the gradual variation is predicted by the technique. Hence, caution must be adopted when analysing the strain data estimated in this transition band, where data are of difficult interpretation. In the proposed approach, two threshold strain values were set at 20% and 80% of ε_L , distinguishing three zones:

austenite, martensite and an indeterminate band. The latter was excluded from the computation of the mean values of strain, as shown in Figure 16.b.

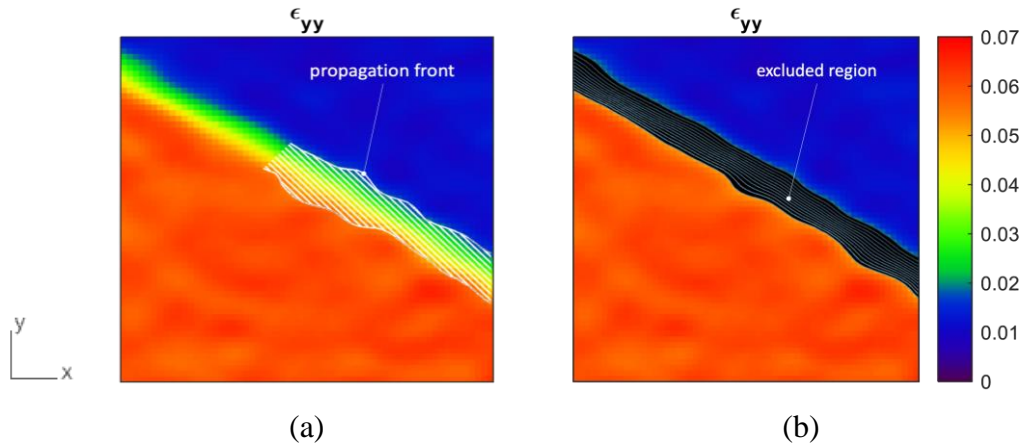


Figure 16 Propagation of the front of phase transition observed in a generic ROI between two successive images, superposed to the region of gradual strain variation predicted by the DIC technique (a); and strain map after exclusion of the transition region (b).

True stresses were calculated as the ratio between the force recorded at the loadcell and the actual cross-sectional area of the analysed region of interest (ROI), estimated as:

$$\sigma = \frac{F}{w * t * (1 + \bar{\epsilon}_{xx})^2} \quad 16$$

where w and t are the width and thickness of the specimen, respectively, and $\bar{\epsilon}_{xx}$ is the mean strain measured orthogonally to the direction of the load (horizontal direction) for the entire ROI. Here, it is assumed that the lateral strain is the same along the width and along the thickness of the specimen.

The Young's moduli of the austenitic and martensitic configurations were calculated from DIC data as ratio between the true stress and the mean strains over a region of interest covering the whole specimen, with exception of two regions in the grips proximity of length equal to the width of the specimen ($ROI_{E,v}$ in Figure 17.a). For consistency with the standard analysis, the same portion of the stress-strain curve

and the same fitting approach as described above for the moduli calculation were used. For these cases, as the whole specimen is in a single phase (either austenite or martensite), the homogeneity assumption can be considered accurate.

A convenient feature of DIC approaches is that they evaluate the whole plain strain tensor, from which it is straight forward to obtain the Poisson's ratio [88]. The Poisson's ratios of the austenitic and martensitic configurations were calculated from DIC data over the same ROI ($ROI_{E,v}$ in Figure 17.a) and obtained as negative of the ratio of the mean transversal strain in the region, $\bar{\epsilon}_{xx}$, to the mean axial strain in the region, $\bar{\epsilon}_{yy}$.

The phase transformation process is characterised by the propagations of Lüders bands, which typically form at an angle of about 55° from the specimen axis [89], thus determining the simultaneous presence of austenite and martensite along the transversal sections crossing the bands. As these two crystal phases are characterised by significantly different Young's moduli, this can result in the local departure of the neutral axis from the centre of gravity of the specimen and the onset of a bending moment. The presence of bending produces local variations of strains and stresses that increase the uncertainty in the stress-strain parameters determined from standard tests. In order to minimise this effect, the features of DIC can be exploited to focus on small ROIs, so as to reduce the variation in the measured parameters. However, although the reduction in the ROI can provide accurate values of the local strains, the associated local stress is more uncertain, especially if a bending moment is superposed to the tensile load. The maximum eccentricity of the neutral axis will be reached when the transformation occurs with a single front within the sample un-gripped area. In this

case, the neutral axis will also coincide with the interface between the two phases, which will be located at a distance from the axis of the cross section equal to:

$$e_{max} = \frac{w}{2} \cdot \frac{1 - \sqrt{2}}{1 + \sqrt{2}} = -0.086 w \quad 17$$

Under these conditions, it can be demonstrated that, assuming an extreme ratio between the Young's moduli of the austenitic and martensitic phases equal to 2, a square ROI region covering 25% of the specimen width and centred at the geometric axis of the specimen would reduce the effect of the spurious bending stress on the average stress calculated through equation 15 of one order of magnitude (see Appendix A). This ROI size was then taken as a good compromise between the need to measure precise strains by focusing on a small region, without compromising the accuracy in the stress determination.

This is in particular true when the maximum bending moment is assumed to keep below:

$$M_{max} \approx \frac{tw^2}{6} \cdot (\sigma_{UPS} - \sigma_{LPS}). \quad 18$$

In fact, for higher values, the cross sections immediately adjacent to the transformation front where the martensitic transformation has covered the full section would not be able to remain in the martensitic phase and, in the compressed side, would return to austenite.

The maximum expected error in the stress determination would be around 0.12 times the difference between the upper and lower plateau strengths. Please notice that the above mentioned behaviour is based on an extreme conservative condition, as the ratio between the austenitic and martensitic Young's moduli is normally lower than 2,

and the Lüders bands tend to separate into striae in the regions of high bending moment, thus reducing the eccentricity of the neutral axis, the peak of bending stress and the error in the stress measurement. Moreover, the mentioned bending moment induced by the mismatch in Young's modulus of the two phases is partially counterbalanced by the bending moment produced by the curvature taken by the specimen as effect of the higher elongation experienced by the specimen side which is more interested by the martensitic transformation (see also Section Appendix A for a more in-depth analysis).

Hence, in order to obtain results representative of the whole specimen, the analysis of the stress-strain relationship was performed and averaged over five square regions of interest ($ROI_{\sigma,\epsilon}$) of equal size, with square side equal to 25% of the specimen's width and centre located on the vertical axis, evenly spaced along the sample length so as to cover the whole region up to a distance from the grips equal to the specimen width (see in Figure 17.b).

The initial and final transformation stress between the two crystal phases and the transformation strain ϵ_L were determined as described above for the standard analysis.

Another interesting additional parameter determined from the DIC analysis was the Poisson's ratio associated with the transformation, ν_T , here defined as the negative of the ratio of the transversal transformation strain ϵ_{Lx} to the axial transformation strain ϵ_L calculated over the $ROI_{E,\nu}$ (see Figure 17.a).

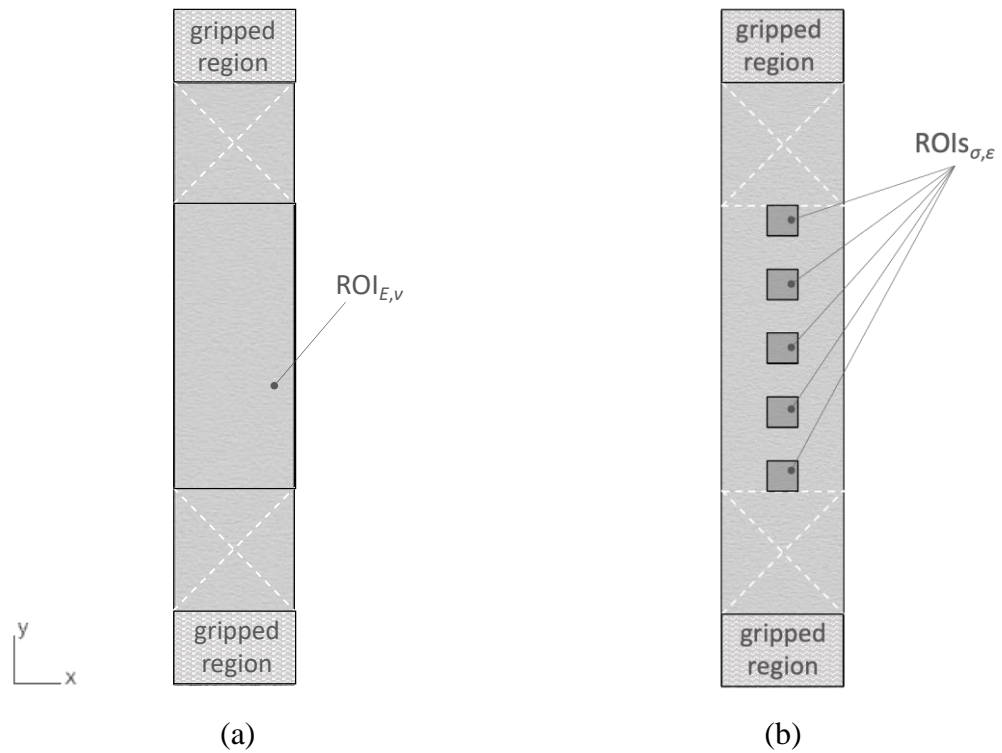


Figure 17 Regions of interest selected for the calculation of the Young's moduli and Poisson's ratios (a); and for the determination of the stress-strain parameters (b).

Results and Discussion

Standard test

Stress-induced martensitic transformation was achieved for the whole gauge length at a peak deformation of 6 %, when the upper transformation plateau appeared to have been completed.

The stress-strain curve obtained from the tensile machine output is represented in Figure 18.a. The curve starts with a smooth and linear behaviour during the austenitic specimen deformation, up to the initiation of the phase transformation (portion $O-A$ in Figure 18.a). This is associated with an initial loss in linearity (portion $A-B$ in Figure 18.a), followed by a sudden drop in the stress at point B in Figure 18.a. Then the stress plateaus up to point C in Figure 18.a, achieving large increases of strains with relatively reduced changes in the stress level. Once the entire gauge length

of the specimen has transformed, the material swaps to the Young's modulus of the martensitic phase, terminating the plateau region (portion *C-D* in Figure 18.a). Then the load is gradually removed, recovering superelastically the entire strain, through the re-transformation into the austenitic phase achieved along the lower plateau (portion *E-F* in Figure 18.a). This is associated with the nucleation of austenite in unloading Lüders bands, followed by a linear elastic return to the initial unloaded configuration (portion *F-O* in Figure 18.a).

The σ_{UPS} and σ_{LPS} were respectively equal to 373.3 MPa and 143.6 MPa, giving a value of σ_E equal to 315.87 MPa. The austenitic Young's modulus was equal to 34.7 GPa; and the martensitic Young's modulus, calculated during the unloading from the peak stress of 411.1 MPa to σ_E was 28.8 GPa (17.0 % lower than the austenitic one).

The fitted straight lines used for the determination of the parameters defining the mechanical behaviour of the material are displayed in Figure 18.b. The initial and final stresses defining the upper plateau were $\sigma_s^{AM} = 356.8$ MPa and $\sigma_f^{AM} = 402.4$ MPa, respectively; while the initial and final stresses defining the lower plateau were $\sigma_s^{MA} = 163.7$ MPa and $\sigma_f^{MA} = 127.9$ MPa, respectively. The transformation strain associated with the austenite to martensite transformation ε_L was equal to 5.1 %.

All mechanical characteristics obtained with the standard analysis are summarised in Table 1.

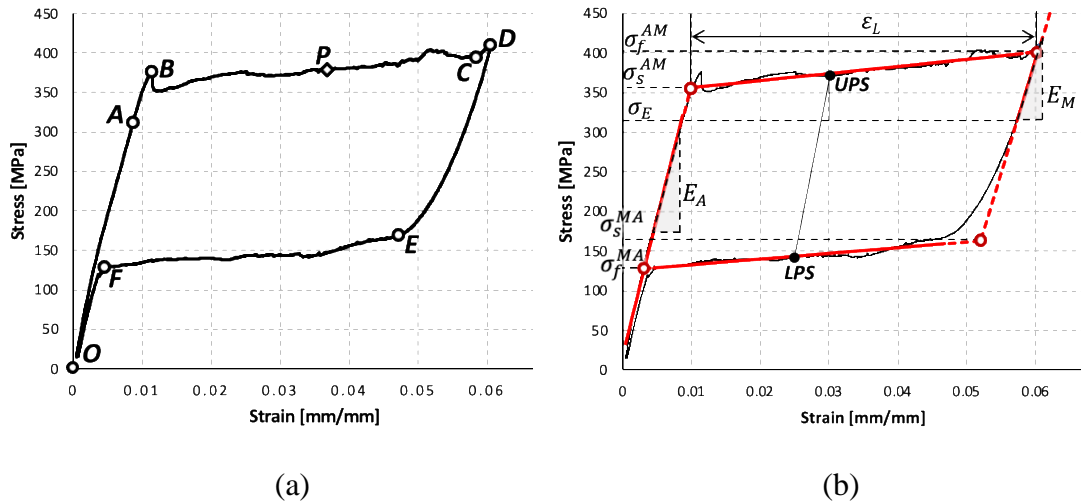


Figure 18 Stress-strain curve obtained from the tensile machine output (a); and fitting used for the determination of the parameters defining the mechanical behaviour of the material (b).

DIC test

The maps of the horizontal (U) and vertical (V) displacements obtained from Ncorr postprocessing at a generic instant P of the upper plateau (as indicated in Figure 18.a) are represented in Figure 19.a and b, respectively. These reveal that, for the analysed instant, the deformation is substantially higher at the bottom portion of the specimen. Moreover, the maps of U and V are not symmetrical about the axis of the specimen, confirming the presence of lateral deflections and local curvatures.

The associated maps of the horizontal and vertical strains ϵ_{xx} and ϵ_{yy} are reported in Figure 19.c and d, respectively. The strain components clearly indicate a bipolar behaviour, with portions of the specimen (the bottom portion for the selected instant) undergoing very high levels of vertical strain (about 7 %), associated with substantial lateral contraction (around 3.5 %). These appear uniformly distributed up to the Lüders bands. This behaviour is consistent with the crystal rearrangement produced by the transformation into martensite. The level of strains experienced by the region in its austenitic state are negligible, when compared with the bottom region. As mentioned

above, a band of gradual passage from the strains characterising the two regions, where strains are considered indeterminate, can be observed in the maps. This, in the presented test, had a thickness of about 0.3 mm, which is consistent with the propagation of the martensitic region between the two instants used for the image correlation.

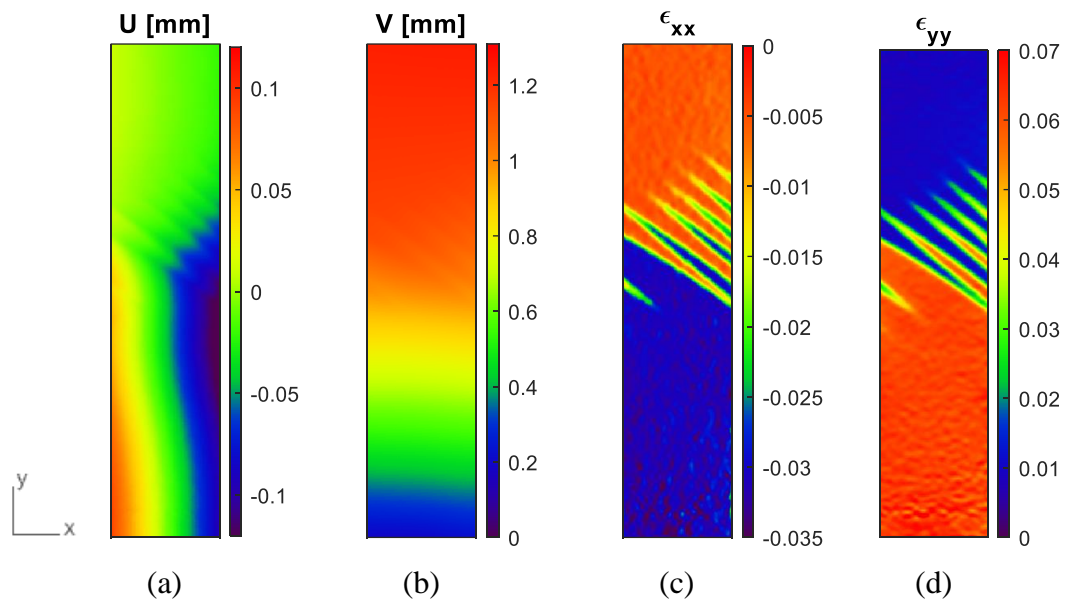
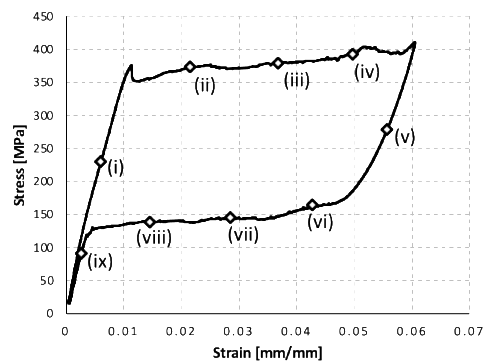


Figure 19 a) Horizontal displacement map; b) vertical displacement map; c) horizontal strain map; d) vertical strain map.

A sequence of deformed shapes of the sample, obtained from the DIC data for the instants i-ix indicated in Figure 20.a is represented in Figure 20.b. Horizontal displacements are amplified of 10 times, while the vertical displacements are kept in the same scale as the physical ones. For each instant, the martensitic and austenitic regions obtained from the strains are mapped on the deformed shape (light grey for austenite and dark grey for martensite). The sequence clearly confirms that the transformation from austenite to martensite initiates at one end of the specimen (in proximity of the bottom grip, for the presented test) and then propagates towards the other end, with Lüders bands forming fringes as the front of propagation progresses

towards the centre of the specimen. The transformation follows the opposite direction during unloading, maintaining similar features.

The Young's moduli of the austenitic and martensitic configurations calculated from DIC over $ROI_{E,v}$ in Figure 17.a were equal to 39.0 GPa and 30.8 GPa, respectively. These values are expected to be different from the corresponding constants quantified from the standard approach, because they are based on strains quantified only in a region at a distance from the grips, and on true stresses, estimated on the basis of the transversal strains according to Equation 16. In particular, both moduli are significantly larger than estimated with the standard analysis.



(a)



i ii iii iv v vi vii vii ix

(b)

Figure 20 a) Instants of the cycle (i-ix) where the sequence of whole specimen deformations in (b) was determined. Horizontal displacements (of Figure 19a) are amplified of 10 times, and the regions occupied by austenite and martensite, obtained from the strain maps, are represented in light and dark grey, respectively.

The Poisson's ratios for the austenitic and martensitic phases, estimated in the same ROI, were respectively equal to 0.47 and 0.42.

The above results confirm the material inhomogeneity and the presence of spurious bending moments, in support of the hypothesis that the analysis of the stress-strain relationship shall be performed on small regions of the specimen in proximity of the longitudinal axis (ROIs _{σ,ϵ}). The fact that the ratio between the austenitic and martensitic Young's modulus is 1.45, and hence much smaller than the value of 2 previously assumed for the estimation of the stress error, indicates that the accuracy is expected to be higher than the one defined above as acceptable. In addition, the eccentricity of the neutral axis due to the mismatch in Young's modulus of the two phases, measured along the entire specimen's axis as:

$$e_{NA} = \frac{\sum xE(x)}{\sum E(x)}; \quad 19$$

is only about one quarter of that estimated from Equation 17.

Another useful result is the fact that the maximum principal direction determined from the strain maps is maintained about aligned with the direction of the applied force ($\pm 5^\circ$) (see Figure 21). All these considerations confirm that the usual stress calculation over the ROIs _{σ,ϵ} (the ratio between the force measured at the load-cell divided by the actual cross section for the ROIs _{σ,ϵ} represented in Figure 17.b) is an acceptable approximation.

The typical stress-strain diagram obtained from the ROIs _{σ,ϵ} in Figure 17.b is represented in Figure 22 (in particular, the central ROI is used in the figure). The

diagrams from the different ROIs are very similar and with very low variability, as indicated by the small standard deviation in the parameters reported below.

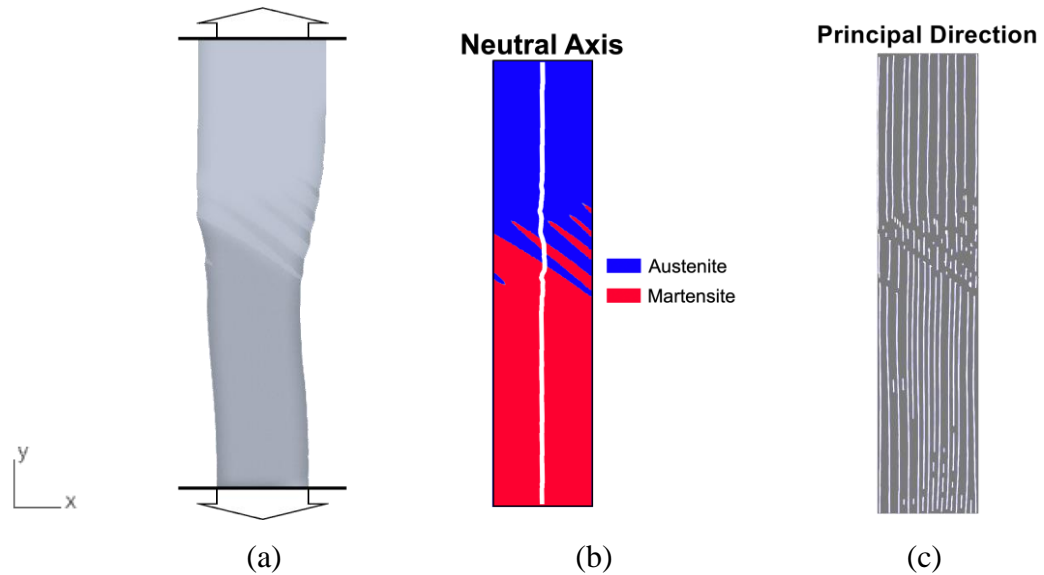


Figure 21 a) Shape of the specimen with amplified lateral displacements; b) map of the specimen showing the austenitic and martensitic regions, and the position of the neutral axis represented by a white line (calculated using Equation 19); c) principal directions determined on the measured strains. All pictures are in relation to the instant P, as indicated in Figure 18.a.

The initial and final stresses defining the upper plateau, recomputed using DIC, were respectively $\sigma_s^{AM} = 378.6 (\pm 1.1 \%)$ MPa and $\sigma_f^{AM} = 401.9 (\pm 1.4 \%)$ MPa; the initial and final stresses defining the lower plateau were respectively $\sigma_s^{MA} = 150.3 (\pm 2.2 \%)$ MPa and $\sigma_f^{MA} = 140.0 (\pm 1.6 \%)$ MPa; and the upper and lower plateau strengths were $\sigma_{UPS} = 387.2 (\pm 1.3 \%)$ MPa and $\sigma_{LPS} = 144.3 (\pm 1.1 \%)$ MPa, respectively. Hence, despite maintaining the plateau strength nearly unchanged compared to the standard analysis, significant increase in σ_s^{AM} and σ_s^{MA} and decrease in σ_f^{AM} and σ_f^{MA} indicate a substantial flattening of the two plateaus (more evident for the lower plateau).

The transformation strain associated with the austenite to martensite transformation ε_L estimated with DIC was $\varepsilon_L = 0.053$, and the associated transversal

(horizontal) transformation strain was $\varepsilon_{Lx} = -0.027$, indicating a Poisson's ratio ν_T associated with the transformation equal to 0.5.

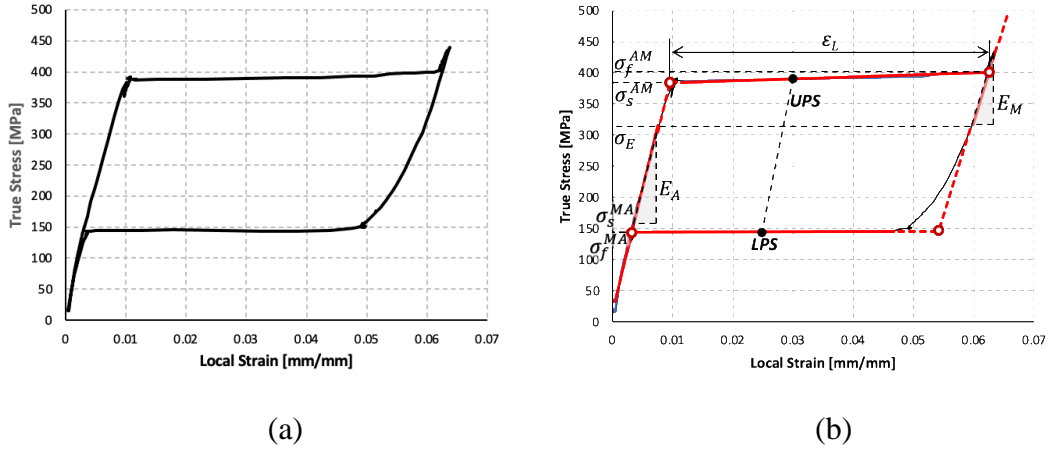


Figure 22 Typical stress-strain map determined on square ROIs with side equal to 25% of the specimen width (in Figure 17.b), positioned on the axis of the specimen (a); and fitting used for the determination of the parameters defining the mechanical behaviour of the material (b).

The stress-strain curve obtained from this approach (e.g. curves displayed in Figure 22a,b) are much closer to the idealised set of straight lines that are fitted to extract the parameters defining the mechanical response of Nitinol. Therefore, they are particularly suitable to characterise the material in a more accurate and consistent way.

The parameters obtained from this approach are summarised in the second data column in Table 1, aside the mechanical characteristics obtained with the standard analysis. In the common practice and in compliance with the available regulatory standards, the stress and strain in Nitinol specimens subjected to uniaxial tension testing are assumed uniformly distributed over a finite area comprised in the extensometer gauge length. However, the present study confirms that this assumption cannot be considered valid. The strain distribution (shown in Figure 19.c,d and used to obtain the maps of phase distribution in the sequence in Figure 20) suggests that the material instantaneously switches between the austenitic and martensitic

configurations when the plateau stress is locally reached. This bimodal behaviour has major consequences.

Table 1 Mechanical characteristics obtained with the different approaches

Parameter		Standard Analysis	DIC reduced ROI	Variation
E_A	[GPa]	34.7	39.0	+ 12.0 %
E_M	[GPa]	28.8	30.8	+ 7%
ν_A		-	0.46	
ν_M		-	0.40	
ν_T		-	0.50	
σ_S^{AM}	[MPa]	356.8	378.6 (± 1.1 %)	+ 6.1 %
σ_f^{AM}	[MPa]	402.4	401.9 (± 1.4 %)	+ 0.1 %
σ_{UPS}	[MPa]	373.3	387.2 (± 1.3 %)	+ 3.7 %
σ_S^{MA}	[MPa]	163.7	150.3 (± 2.2 %)	- 8.2 %
σ_f^{MA}	[MPa]	127.9	140.0 (± 1.6 %)	+ 9.5 %
σ_{LPS}	[MPa]	143.6	144.3 (± 1.1 %)	+ 0.5 %
ε_L	[%]	5.1	5.3 (± 0.4 %)	+3.9 %

In fact, in order to maintain geometrical congruence, the interface between the region where the martensitic transformation has occurred, which experiences significant levels of longitudinal and lateral deformation, and the portion of the specimen which is in the austenitic phase, need to take a specific angle with respect to the axis. With reference to Figure 23.a, as an effect of the transformation strain ε_L experienced by the martensitic region, it will be:

$$h_M = h_A(1 + \varepsilon_L) \quad 20$$

and

$$w_M = w_A(1 - \nu_T \varepsilon_L) \quad 21$$

where ν_T corresponds to the Poisson's ratio associated with the phase transformation. Basic geometrical considerations (reported in the Appendix B) lead to the determination of the angles that need to establish between the interface (transformation front line) and the transversal section of the austenitic and martensitic regions, α_A and α_M , respectively:

$$\alpha_A = \arctan \sqrt{\frac{2\nu_T - \nu_T^2 \varepsilon_L}{2 + \varepsilon_L}}; \quad 22$$

and

$$\alpha_M = \arcsin[(1 + \varepsilon_L) \sin \alpha_A]. \quad 23$$

Interestingly, these angles do not depend on the mechanical properties of two phases, but only on the transformation strain and on the transformation Poisson's ratio. As in our case $\varepsilon_L = 0.053$ and $\nu_T = 0.5$, the equation above provides an angle of 34.73° for α_A and 36.86° for α_M , with an average inclination of the transformation front with respect to the cross section of the specimen of 35.80° . Moreover, because of the same phenomenon, the axes of the austenitic and martensitic regions will tend to be angled with respect to each other, aiming at a misalignment given by $\alpha_M - \alpha_A$, which in the presented case is of 2.13° . As a result, the specimen plays towards the side where the martensitic length is greater, as shown in Figure 20.b(ii). This is necessarily associated with the introduction of a spurious bending moment. Moreover, the presence of a fixed constrain at the grips requires that the length of the specimen in the left and right sides stays approximately equal and the axes at the top and bottom maintain their alignment during the test. Hence, as the front of transformation progresses towards the midspan,

the bending moment increases until, eventually, a set of new fringes form, serving as hinge regions which allow the specimen to realign its axes at the top and bottom ends and relax the bending moment, as schematically shown in Figure 23.b (this is evident in the experimentally determined sequence reported in Figure 20.b, starting from instant iii). These fringes allow to balance the percentage of austenite (whose stretching is negligible) and martensite (which is highly stretched) in the left and right sides of the specimen, so as to match the vertical length of the specimen for the different vertical lines. This phenomenon produces new transformation fringes at the side of the specimen where the length of the stretched martensitic region is inferior and, therefore, needs to be increased. The described process justifies and explains the formation of the Lüders bands which, consistently with the literature [81,82], were observed in the present study at an angle of about 35° from the cross-sectional plane (corresponding to about 55° from the specimen's longitudinal axis). It is reasonable to expect that similar phenomena may occur along the thickness, although with much smaller influence on the overall specimen behaviour, due to reduced dimension.

The implication of the described phenomenon is that the same cross section may be characterised by multiple regions with alternative crystal configurations and, therefore, different mechanical properties. This, as described above, results in departures of the neutral axis from the cross-sectional centre of gravity, that contribute to locally introduce an additional bending moment. However, as the neutral axis tends to move towards the side where the Young's modulus is greater (the austenitic region), this effect does not cumulate with the one described above, but it does locally counterbalance it.

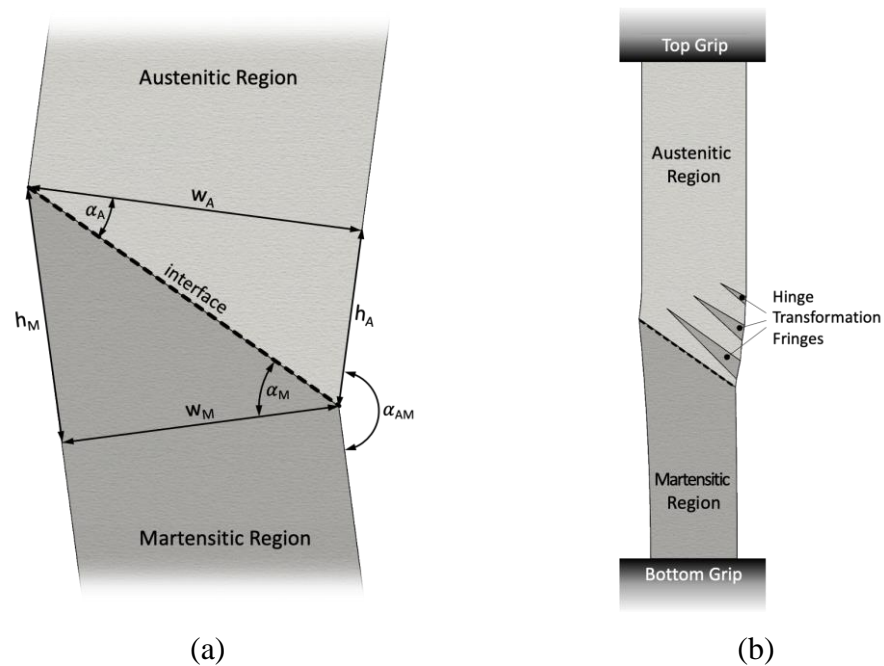


Figure 23 Schematic representation of the region of interface between the austenitic and martensitic regions (a), and of the full specimen in the transformation plateau region (b).

The phenomena described above refute the very basis of uniaxial tension tests, questioning the suitability of current practices to derive information on the material behaviour which should be compatible with the high-risk applications that rely on Nitinol. In fact, the stress-strain curve obtained from the tensile machine output, as shown in Figure 17, represents an average in time of a combination of effects which interest different and varying regions of the specimen. This is reflected in the irregularity of the plateaus, that makes particularly difficult to identify objective criteria to idealise the diagram and extract the common material characteristics.

In this test, the testing machine crosshead was used to determine the strain (this is accepted by the ASTM standards [21,23]), but similar issues are to be expected with the use of mechanical extensometers. In fact, any practical distance between the extensometers knife edges would still be associated with highly inhomogeneous behaviours. Moreover, the propagation of the transformation front and hinge fringes

at a large angle with the specimen's cross section (larger than 35 °) would introduce errors and further complexity in the interpretation of the results.

Most importantly, all phenomena described above that can affect the results are essentially dependent on the specimen dimensions and testing setup, making the measurement of the mechanical characteristics of the material very difficult to generalise. This indicates a clear need for a new approach allowing a more objective analysis, especially in consideration of the high-risk healthcare applications where Nitinol is commonly used, that require the highest levels of optimisation. In this scenario, features of full-field and non-contact measurement such as those of DIC techniques become essential to provide a proper investigation of the material behaviour.

The stress-strain curve obtained from the DIC results (in Figure 22) on smaller ROIs (25% of the specimen's width in the presented study) focalised along the geometric axis of the specimen, so as to minimise bending stresses, become very repeatable and more suitable to characterise the material behaviour. Comparing the stress-strain diagrams obtained with the standard and DIC approaches (see Figure 24), it is evident that the sudden drop in the stress observed in the data from the tensile machine output is an artefact due to the phenomena described above. Instead, at local level, the reduction in load associated with the triggering of the martensitic transformation at a different region of the specimen, is perceived as a small unloading along the austenitic curve, then compensated by further increase in stress, until transformation initiates in the analysed ROI. As a result, the plateau flattens substantially at levels of stress closer to the final plateau stress. Flattening of the

plateau is even more evident for the lower plateau, where the difference between the start and finish transformation stress is in the order of 7 %.

Another interesting correction introduced by the local DIC analysis is in the slope of the martensitic phase, which contrary to the standard approach appears to be well overlapping for the loading and unloading branches.

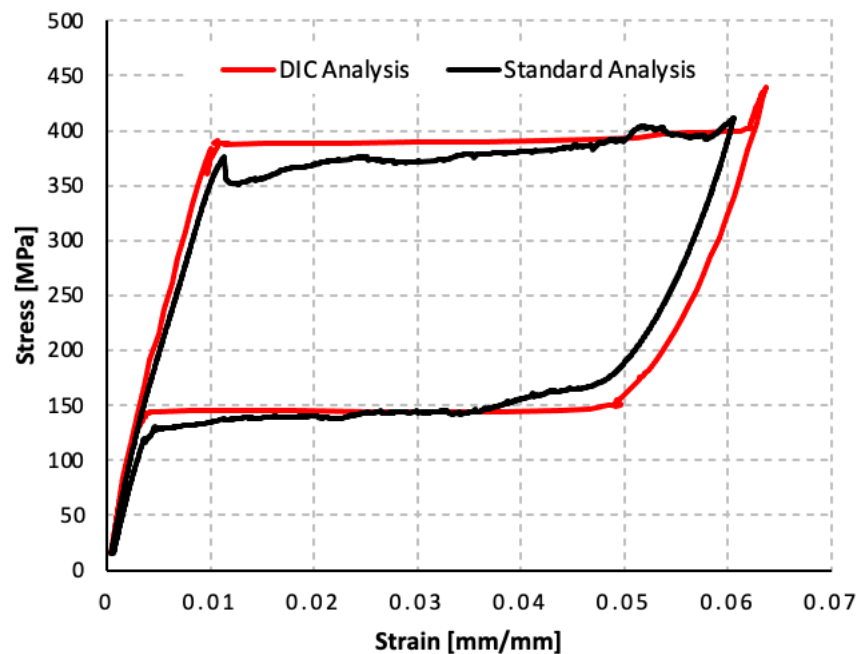


Figure 24 Stress-strain map determined with the standard and DIC approaches described in the article.

Also, true stresses determined from the DIC analysis are substantially larger than the engineering stresses, resulting in significant increase in the transformation stresses and in the Young's moduli of the two materials than predicted with the standard approach.

These differences are due to the high Poisson's ratios observed for the austenitic and martensitic phases ($\nu_A = 0.46$ and $\nu_M = 0.40$), which appear to be much larger than the value of 0.33 commonly assumed in the literature for both phases [90] and produce substantial contractions in the actual cross section. This interesting finding compares

well with measurements of the Poisson's ratio performed on polycrystalline martensitic Nitinol with neutron diffraction, which indicated a value of ν_M equal 0.39 ± 0.03 [91]. Similarly, the material data provided in a computational study from *Kleinstreuer et al.* indicate a value of 0.46 for both ν_A and ν_M [92]. For what concerns the Poisson's ratio associated with the transformation ν_T , this appears more consistent with the data in the literature, that typically refer to a value of 0.5 [86]. As the Poisson's ratios are critical for a correct description and modelling of the material's behaviour, these contrasting data clearly indicates a gap in the current literature.

Although the presented approach may contribute to determine more objective and representative parameters of the mechanical properties, less dependent of the specific test setup and conditions, this still needs to be accompanied by the implementation of more advanced constitutive models for Nitinol alloys, able to better replicate the inhomogeneous phenomena observed in the test.

Conclusion

In conclusion, the main sources of error affecting the reliability of standard uniaxial tension tests for the mechanical characterisation of superelastic Nitinol alloys was analysed. In particular, the stress induced transformation that provides the super-elastic behaviour also causes the presence of regional inhomogeneities in the test specimen, associated with the formation of Lüders bands, lateral displacements and spurious bending moments superposed to the tensile load. These phenomena limit the reliability of standard characterisation methods to provide parameters sufficiently accurate to achieve an adequate description of the material and to exploit its features optimally. DIC analysis, by allowing a full field detection of the strains, can help not

just to clarify, but also to overcome these limitations. In fact, performing the mechanical characterisation in regions of interest sufficiently small, in proximity of the specimen's axis, allows to minimise the spurious effects and determine more accurate and consistent parameters, that describe a material response which appear to be closer to the ideal one and independent of the testing setup. This is characterised by flatter plateaus that closely match straight lines suitable to extract parameters defining the mechanical response of Nitinol. Therefore, they are particularly suitable to provide a more accurate and consistent characterisation of the material. Still, results are affected by assumptions and approximations in the determination of the stress and in the exclusion of the regions at the interface between the two crystal phases. Nevertheless, the proposed approach surely provides a substantially improved characterisation of the material, much needed to support the selection of specific alloys and thermo-mechanical treatments, and to achieve optimised levels of safety and efficacy in the most critical applications where Nitinol is employed.

4.1.1.2 Thermo-Mechanical characterisation (DIC and IRT)

The combined use of DIC and TSA (respectively described in section 3.2.1.1 and 3.2.2.1) has the potential to allow the investigation of thermo-mechanical couplings in Nitinol while distinguishing the local nature of the material that is well inferred through DIC maps. In this section a thermo-mechanical analysis is proposed, that is carried out by implementing the same measuring setup and signal processing procedures typical of the TSA technique. In particular, a TSA alike investigation is carried out on Nitinol strips subject to cyclic tensile loading with variable amplitudes.

In literature, the investigation on phase transformation and thermo-mechanical behaviour in superelastic Nitinol has significantly advanced since full-field techniques for measuring temperature were adopted [93–97]. In particular, IRT has proven to be most useful in revealing the localized features of phase transformation [11,98–101]. A majority of fatigue studies so far has focused on phase transformation fatigue, i.e. the case when each loading cycle involves a two-way phase transformation [102–104]. In these conditions, fatigue strength is primarily related with the ability of the material to cyclically sustain a forth-and-back transition between the Austenite and Martensite states, which results in a low-cycle fatigue strength. This case, though, is primarily relevant in applications such as solid-state cooling, or other functional applications specifically relying on the maximum recoverable strain evolution [105]. Under such high-strains amplitude fatigue, the latent heat of transformation is also the major thermo-mechanical heat source (elasto-caloric effect), and its reversible nature is reflected on the modulation of the temperature signal, which is in phase with the loading signal.

Under low amplitude strain cycling, assuming adiabatic conditions, neglecting internal dissipations and assuming also that no latent heat of transformation is released, the main heat source that remains should consist in the thermoelastic effect. This scenario would allow to express the temperature changes as functions of stresses-strains only, through the first or second order laws of the Thermoelastic effect [70,72,73] (see equation 8 and 9). Only a few works have explored the validity and utility of the previous assumptions [12,106], where the temperature appears to change in phase with the load, against the predictions of the first order Thermoelastic theory. By adopting a second order thermoelastic theory, *Eaton-Evans et al.* found that a

positive-valued derivative of the Young's modulus E with temperature could indeed justify a thermoelastic signal in phase with the external load [12,106]. A relatively high and positive dE/dT was also measured experimentally in the Austenite and Martensite states around room temperature.

In this work, the Nitinol thermo-mechanical coupling is investigated by analysing a low amplitude cyclic load chosen with a wave amplitude smaller than the difference between the two stress transformation plateaus. Such loading condition should freeze the distribution of Austenite or Martensite zones.

Test setup

A rectangular strip of Nitinol described in section 4.1.1.1 (see Figure 15) has been tested under quasi-static and cyclic loading. During loading, the strain field and temperature are synchronously monitored by 2D Digital Image Correlation from one face of the sample, and Infrared Thermography on the opposite face of the sample. The temperature field was acquired with an Infrared camera (FLIR X6540sc thermal camera) with a sampling frame rate of 105 Hz for cycling test, of 1 Hz for quasi-static test. To enhance the emissivity and reduce reflection, the sample surface was previously painted with a matt black paint. Thermal data were pre-processed in Flir Research IR v3.4 software and then exported for post-processing in Matlab. Instead, the other face of the specimen was painted with a black speckle on a white background for the DIC application. That surface was monitored with a camera (Nikon D5100 equipped with a Macro lens) sampling one picture every 2 seconds. The DIC technique (described in section 3.2.1.1) was applied processing the picture in NCORR obtaining as result the strain maps used to identify the transformation status.

Loading was applied on an electro-mechanic Instron 3367 testing machine with loads profile reported in Table 2. In particular, a quasi-static test (QS) was applied in displacement control at a speed of 0.5 mm/s to perform a quasi-static complete transformation. Then two cyclic tests (C_{up} and C_{down}) were set to have a sufficiently small cyclic load amplitude that should hamper any progression of phase transformation. The latter tests were conducted together (test C), using as reference the quasi-static loading. In particular, after a ramp from 0 to 1.2 mm, at 0.5 mm/min, the specimen was cycled between 1.2 and 1.05 mm at 0.6 mm/s (2Hz) for 150 cycles (C_{up}). Then, in order to completely transform the austenite, it was performed a ramp from 1.2 to 2.1 mm and down from 2.1 to 1.2 mm, both at 0.5 mm/min. The C_{down} cyclic loading range was performed between 1.2 and 1.35 mm at 2 Hz for 150 cycles and then the specimen was brought back to 0 at 0.5 mm/min.

Table 2 Experiments Denomination

Type of experiment	Test Denomination
Quasi-static	QS
Cyclic no phase transformation from upper plateau	C_{up}
Cyclic no phase transformation from lower plateau	C_{down}

Signal processing

The harmonic content of the applied loading waveform and the temperature signal in C_{up} and C_{down} were obtained by applying the Discrete Fourier Transformation (DFT). Due to the triangular shape of the displacement waveform the power in the harmonic spectrum is principally distributed on odd multiples of the wave fundamental frequency ω , with a decreasing amplitude at increasing frequency.

The temperature sequences acquired during cyclic loading were analysed in Matlab by applying a Discrete Fourier Transform (DFT) based analysis [107].

In Matlab the signal processing scheme to evaluate the amplitude of the principal harmonic was applied implementing the following steps:

- A time window is selected such to include approximately an integer number of cycles;
- Thermal/load signal are analysed with the DFT Matlab function, obtaining the equation below:

$$Y(x) = A_m + A_1 \sin(\omega \cdot x + \phi_1) + A_2 \sin(2\omega \cdot x + \phi_2) + A_3 \sin(\omega \cdot x + \phi_3) \quad 24$$

where A_m is the mean value, A_1, A_2, A_3 are the the harmonics amplitude, ϕ_1, ϕ_2, ϕ_3 are the corresponding phases and ω is the angular frequency;

- The harmonics amplitudes (A_1, A_2, A_3) and phases (ϕ_1, ϕ_2, ϕ_3) at the angular frequency (ω) and integer multiple of the angular loading frequency (2ω and 3ω) are reported.

Results

Figure 25 summarize the *QS* test result. The load-displacement curve shows a superelastic behaviour that is characterized by two pseudo-plateaus. Moreover, thermograms and ε_{yy} maps referred to specific points of the load-displacement curve are reported. From the strain map it is observed that the transformation starts from the gripped area and progresses with a unique front advancing in a continuous manner, swiping all the remaining sample area from one grip to the other. Next to each DIC map in Figure 25 is also reported the temperature. Since this is a quasi-static test, the temperature map changes originating from the localized latent heat of transformation

tending to diffuse away by conduction, so thermal fronts appear blurred. Even so, it is clearly observed that the zone of actual phase transformation is also the zone with higher temperature (in the case of upper plateau, point a,b,c,d,e in Figure 25) or lower temperature (in the case of lower plateau, point f,g,h,i,l in Figure 25).

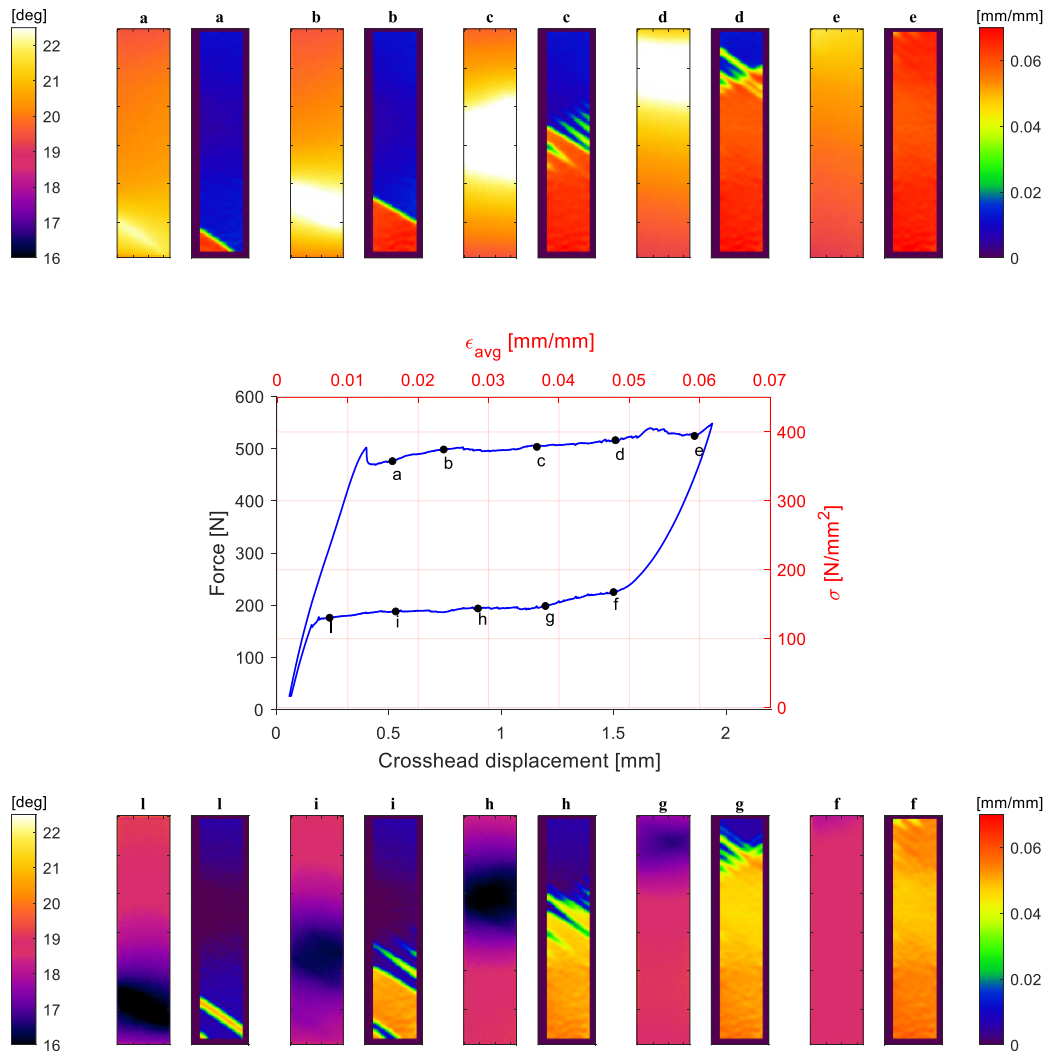


Figure 25 Plot of the load vs displacement or engineering stress/strain curves for test QS, and comparison of thermal and ϵ_{yy} DIC maps on some selected points along the upper and lower plateaus of phase transformation transitory

Figure 26a shows the load vs crosshead displacement curve for the C test, which included the C_{up} and C_{down} cyclic windows. The C_{up} cyclic loading step was run between 1.2 and 1.05 mm avoiding any activation of forth-and-back transformation,

as shown by the DIC map in Figure 26b. A similar behaviour is obtained for the second cyclic loading window (see the DIC map in Figure 26c), starting from the lower plateau. Therefore, phase transformations in both cyclic loadings remain frozen. Figure 26c shows the C_{down} strain map. It has a larger martensitic area than the austenitic one, that result too close to the lower grip. For this reason, just the C_{up} test was analysed.

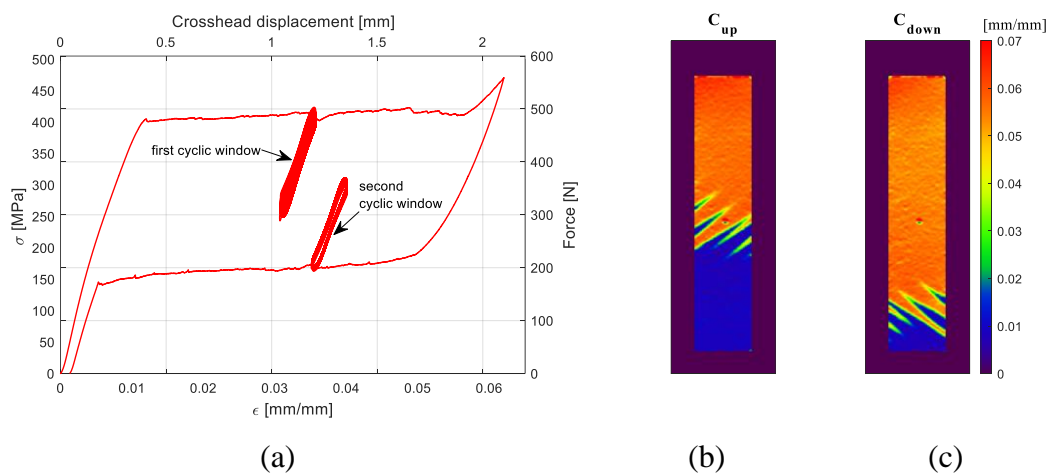


Figure 26 a) Plot of Load-Displacement curve for test C; (b) map of ϵ_{yy} strain from DIC during the first cyclic ed c) map of ϵ_{yy} strain from DIC during the second cycling

Figure 27a illustrates the temperature distribution during the first cycling window, starting on the upper plateau (C_{up}). In particular, two temperature profiles are shown, one referring to a martensitic area, and the second area placed in the non-transformed Austenite (see Figure 27b). The first noteworthy feature, common to both regards the initial decay of the mean temperature. It is believed that such drop is due to the strong dependence of the thermoelastic signal with the average stress. In fact, when the cyclic loading starts, the average stress goes from the plateau stress to a lower value. Similarly to what observed by *Eaton-Evans et al.* [106], the specimen exhibited a temperature change that has the same sign of the tensile stress change. Another

feature of the temperature signal regards the low noise, this could well be the effect of a rather high thermoelastic coefficient K_I of Nitinol (in equation 9).

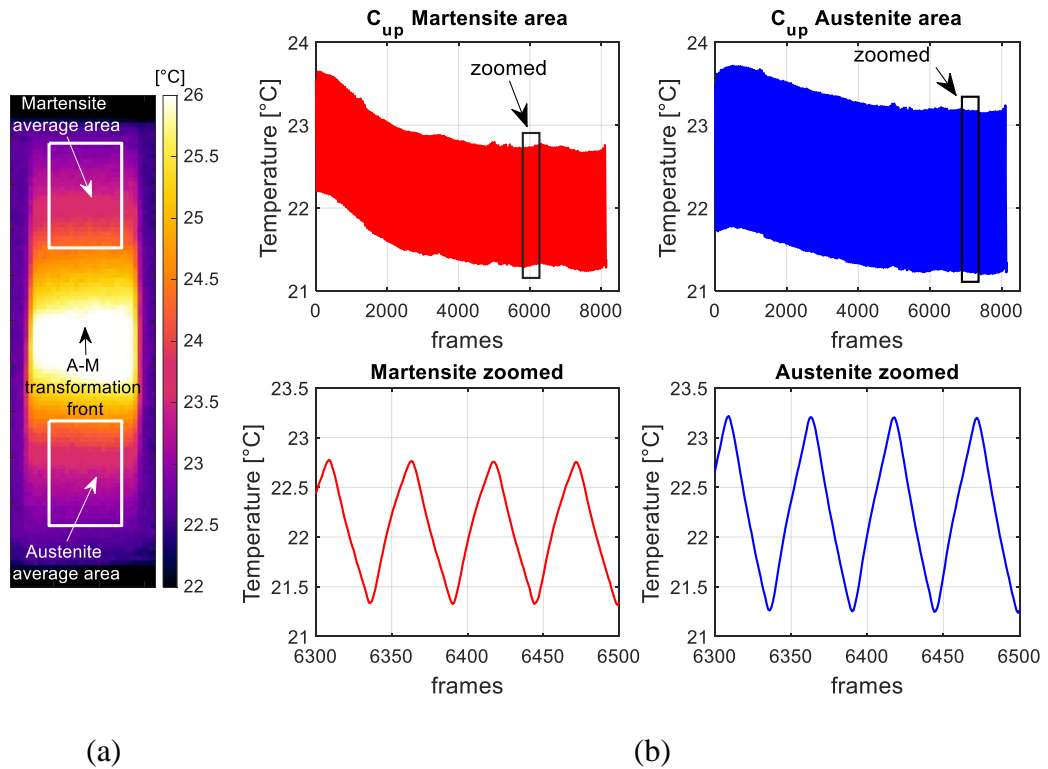


Figure 27 a) Thermogram preceding the start of first cycling stage; b) plots of temperature versus frames (i.e. time) during cycling from points MT and AS, indicated in (a) and the related zoomed detail of the temperature variation.

Figure 28 and Figure 29 show power and phase spectrums of the load and thermal signals acquired during the C_{up} cycling window. The DFT was performed on a sub-window which contained about 40 cycles, taken from the end of the cycling window, when the average temperature signal became stabilized. Because of the triangular wave form, the power spectrum exhibits a quite rich frequency content (in Figure 29a and Figure 29a,c). In Figure 28 and Figure 29 the green dots are the mean value, the red dots indicate harmonics at odd multiple of ω , blue dots at even multiples of ω and all other grey dots belong to the noise bed.

The load signal exhibits significant harmonics at odd and even multiples of ω , as shown in Figure 28a. These might arise due to a non-linear response of the material within each cycle. It is noticed (in Figure 28b) that the phase of the second and fourth harmonics seem to approach 0° , even if the second harmonic has a value of 60° .

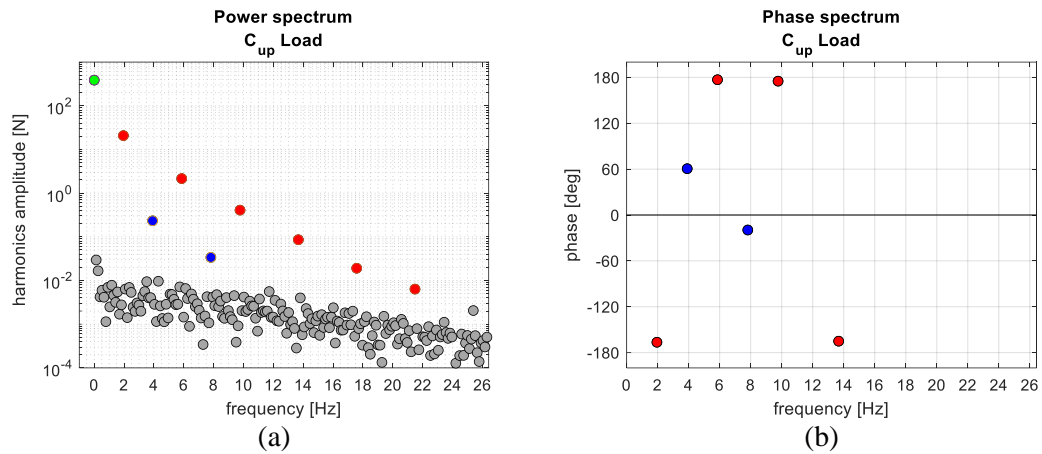


Figure 28 a) Power and b) Phase spectrum of the Load signal

Figure 29 reports the harmonic power spectrum of the temperature signal related to the Austenite and Martensite area. It is here highlighted that while all odd harmonics have a $\pm 180^\circ$ phase, in agreement with the triangular wave loading, The second and fourth harmonics follow different behaviours in the Austenite and Martensite area. In particular, in the Austenite area the second harmonic seems to be opposite in phase with the second harmonic of the load (compare Figure 28b with Figure 29b). In the Martensite area all even harmonics have $\pm 180^\circ$ phases.

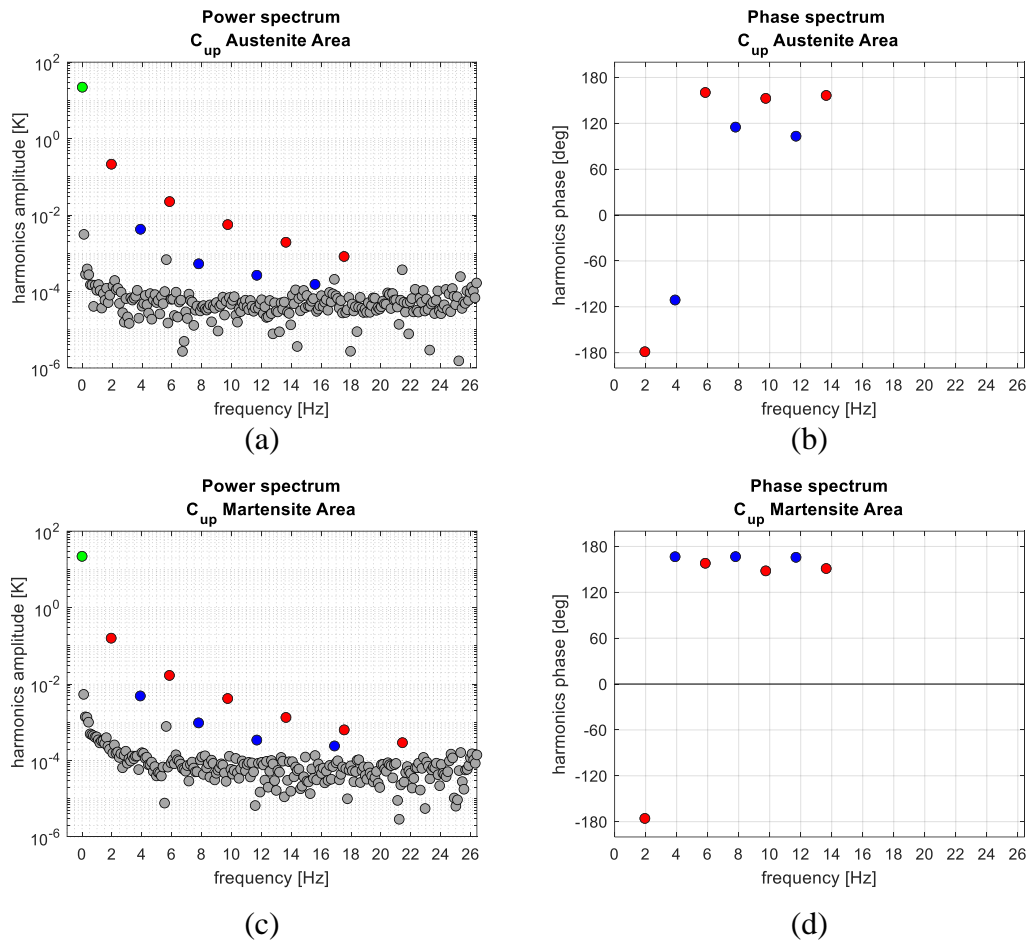


Figure 29 a,c) Power and b,d) Phase spectrum of the temperature signal referred to Austenite and Martensite areas

Finally, Figure 30 shows the maps of the amplitude and phase of the first, second and third harmonics, i.e., the harmonics at ω , 2ω and 3ω .

The harmonic amplitude maps at ω and 3ω have very similar features (in Figure 30a,c), with the 3ω map which seems just rescaled to lower values. This behaviour induces to believe that the response of odd harmonics is proportional to the amplitude of the corresponding load harmonics. Furthermore, the amplitude of the ω harmonic is higher in the Austenite region and lower in the Martensite region. This result seems to be in accordance with the literature results [12,106], where the Austenite region exhibited a higher signal than the Martensite. Average values taken from areas inside

the Austenite and the Martensite zones indicate a ratio of thermoelastic signals of about 1.716/1.297. Instead, the second harmonic in Figure 30b has an almost uniform signal in the Austenite and Martensite phase areas. In Figure 30d,e,f the harmonics phases are reported. It can be noticed that the first and third harmonic have for Austenite and Martensite areas the same phase (± 180) and the second harmonic present a significant phase shift between Austenite and Martensite.

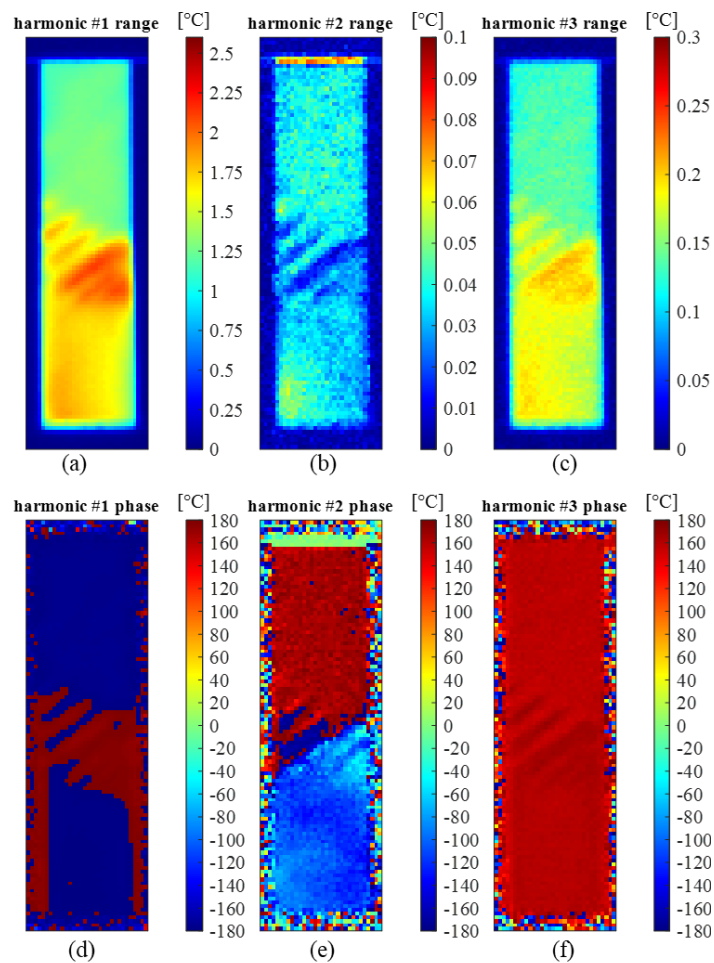


Figure 30 Maps of C_{up} test thermoelastic amplitude signal of the first a), second b) and third c) harmonic and in d),e) and f) the respective phase map.

From Figure 30a it is also interesting to observe that in the zones where the transformation fronts are localized, the thermoelastic signal seems to increase. This is more evident in the lower-right part of the transformation front zone, where the

Martensite Lüders bands appears as thinner branches. Such increase might be due to a number of reasons, which require further investigations, instead in the rest of the sample the phase signal is almost constant.

So, the temperature harmonic at $\omega, 3\omega$, and distinctly all other significant harmonics at odd multiples of ω , are in-phase with the corresponding load harmonics for both the Austenite and Martensite. This behaviour can only be justified by a second order thermoelastic effect formulation expressed by the equation 9 when $K_1\sigma_m > K_0$. The harmonic amplitude at 2ω results with an amplitude at least two orders of magnitude smaller than the ω (see Figure 30a,b). Furthermore equation 9 foresees that the harmonic at 2ω should be a cosine wave with 0° phase if the harmonic at ω is a cosine wave triggered at $\pm 180^\circ$. The outcome in terms of phases can be seen in Figure 28b and Figure 29b,d. In particular, Austenite regions have a 2ω phase that differs from 0° and Martensite regions also have 2ω phases different from 0° and consistently equal to $\pm 180^\circ$. Furthermore, it is curiously observed that the harmonic at 2ω in the Austenite material is opposite in phase to the harmonic at 2ω of the load signal. This is a typical response expected from a first order Thermoelastic theory, which is anyway ruled out by the behaviour of the material at odd harmonics. The Martensite 2ω phase is instead compliant with the first order thermoelastic theory. Its 2ω harmonic has a $\pm 180^\circ$ phase shift with the load 2ω harmonic.

Conclusion

In conclusion, the combined application of DIC and TSA can effectively provide important application on the local mechanical response of Nitinol components,

currently impossible to observe with other approaches. The study shows evidence that the Thermoelastic Effect theory and the thermoelastic heat source are not able to fully justify the amplitude and phase.

However, despite the unconventional thermoelastic response of Nitinol, a direct link is observed between the local and global stress state and the thermal signal emitted, substantially stronger in intensity than in common metals. This suggests that the proposed approach may establish as an important tool to enhance the thermomechanical characterisation of Nitinol components, contributing to enhance the safety of critical application, such as those in the cardiovascular area.

4.1.2 Biological tissue characterisation (DIC)

The interest on biological tissue testing is due to the necessity to achieve a more accurate mechanical characterisation, allowing their more consistent and efficient use in prosthetic applications such as cardiac and vascular patches or bioprosthetic heart valves. In fact, as described in section 3.1.1, the majority of biological and TAVI prosthetic valves are made from bovine or porcine pericardium. This is a membrane that encloses the heart of mammals, with the function to provide lubrication to the heart pulsatile movement, and contribute to redistribute the cardiac pressure [108]. It is a composite material constituted of multidirectional bundles of collagen and elastin fibres embedded in a matrix of proteins and polysaccharides in hydrated complexes. Collagen fibres are coiled and aligned with some preferential directionality, that causes a nonlinear and anisotropic behaviour [49,109]. The matrix confers an incompressible behaviour because of its high water content [48]. The mechanical characterisation for

pericardium and other soft biomaterials is commonly carried out by following existing standard, mostly set for rubber materials [50,51,110,111]. However, uniaxial tests are inadequate because they are not able to capture the heterogeneous multi-axial large deformation fields that characterises their common operating conditions [112]. In this contest, biaxial test may overcome many of the uniaxial loading limitations, although a standard test has not been defined yet.

Biaxial testing machines may use three principal types of gripping systems: clamps, suture and rakes [7]. Large specimens are usually trimmed with a cruciform shape and gripped by using the clamp system, in which the anchored edges load the central area. Instead, small specimens of square shape are better characterized by suture and rakes systems. Suture systems (in Figure 31a) grip the specimen by using sutures lines mounted on pulleys. Pulleys allows specimen rotation applying uniform force, although the system presents poor repeatability due to difficult setup. Rakes systems (in Figure 31b) grip square specimens with a set of pins, thin beams anchored on a common base. Pins have an easier mounting procedure and permit specimen enlarging or shrinking. Suture and rakes systems involve stitches passing through punctures, which necessarily require an excess of length over the gauge length, to be left for the anchoring, whose minimum size will depending on the suture retention strength of the material. The effect of this excess of material on the experiment results, normally assumed negligible [7], has never been studied systematically.

In this work, in order to verify the influence of the extra material on the mechanical behaviour, the specimen dimension is investigated experimentally and numerically, by performing biaxial tests on silicone samples with different outer frame

dimensions. Practically, in order to assess specimen dimension influence, the specimens were tested and cut in sequence, obtaining from each test mechanical characteristics. Then, the experimental mechanical characteristics obtained through Digital Image Correlation DIC were compared with the numerical ones.

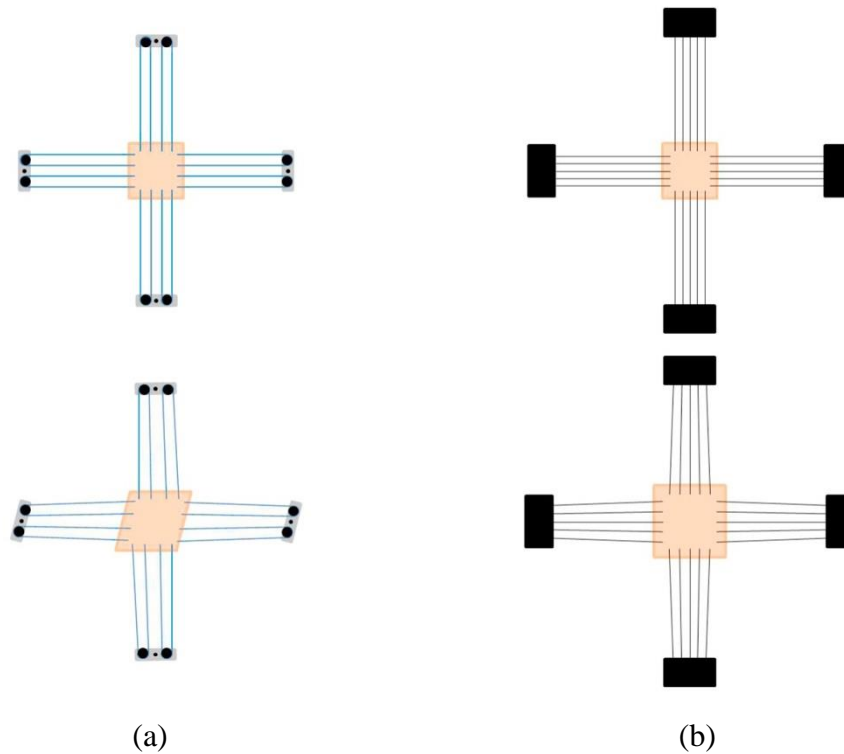


Figure 31 gripping mechanisms: a) sutures and b) rakes [7]

Test setup

Three square specimens, of side 20 mm and thickness 1.197 mm, 0.937 mm and 0.922 mm respectively, made of GI-1100 bicomponent silicone (Silicones Biaxial Test System) were mechanically tested. Tests were conducted on a CellScale Biotester (CellScale Biomaterials Testing, Canada) The testing machine apply biaxial forces to soft tissue specimens and is composed by four actuators, two load cells of 23 N each and a CCD camera for DIC application. To grip the specimen BioRakes CS-BT-305-22-30 (tin diameter: 305 μm , tine spacing 2.2 mm, puncture depth:1.9 mm) were used.

These are recommended for square specimen of side 11.0 – 13.0 mm, suitable for a gauge length of 10 mm. Therefore, considering that the test region is 10 mm and the initial specimen side is 20 mm, the outer frame is 5 mm per each side (wide specimen in Figure 32). Furthermore, in order to study the influence of the outer frame, each specimen was tested and trimmed in sequence three times, reducing the outer frame from 5 mm to 3 mm and 1 mm respectively (wide, medium and small specimen in Figure 32). Then, the small specimen after the test was cut between the rakes with cuts aligned with the rakes beams and the four corners were removed, obtaining the trimmed specimen outlined in Figure 32.

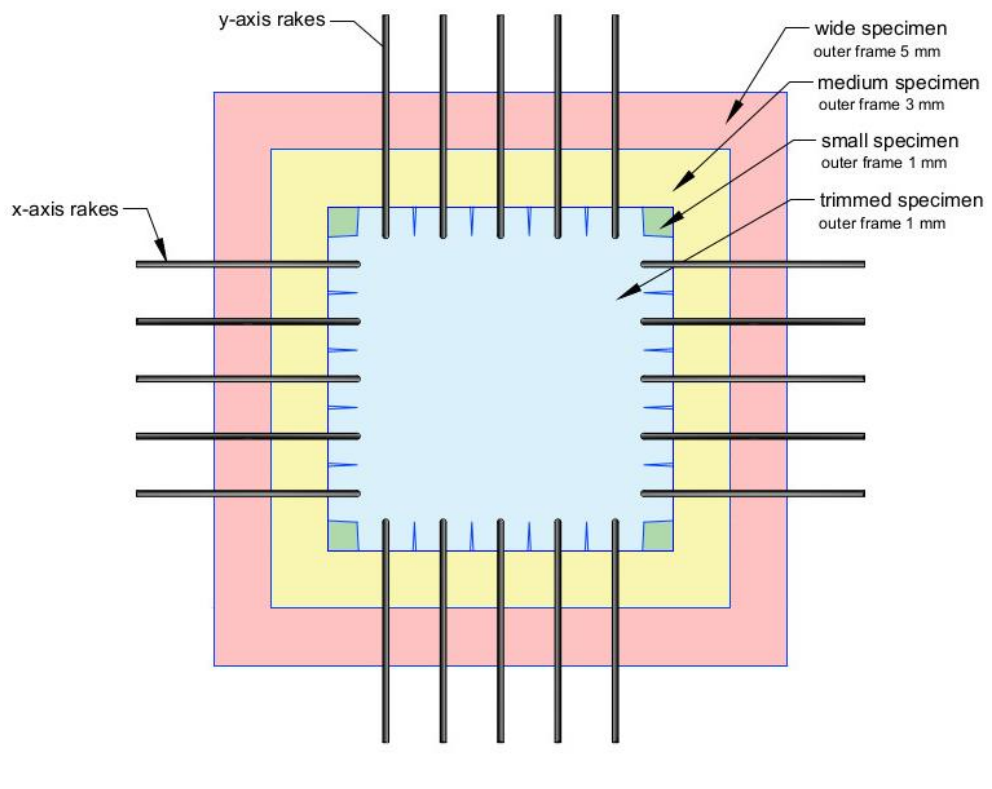


Figure 32 Specimen cutting layout

For DIC application one side of the wide specimen was painted with a random black speckle (in Figure 33) and was kept untouched during all sequence of tests.

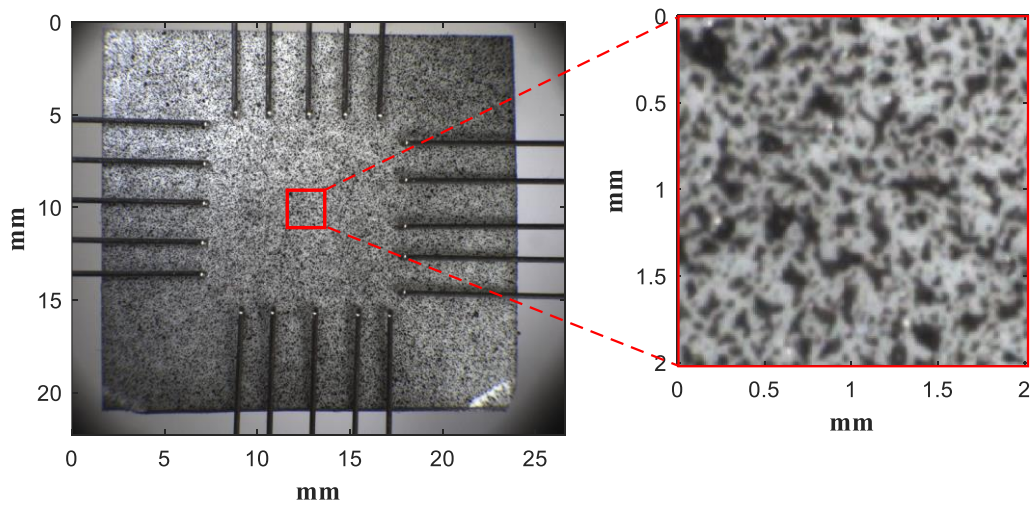


Figure 33 Wide specimen clamped with a detail of the speckle

In order to test multiple times, the same specimen without altering the attachment configuration, these were maintained clamped during the cutting procedure (in Figure 34b). For this purpose, a lifting system was designed and 3D printed (in Figure 34a). The test was set in displacement control, applying a ramp from 0 mm to 2.5 mm at 0.1 mm/s, followed by a recovery to 0 mm.

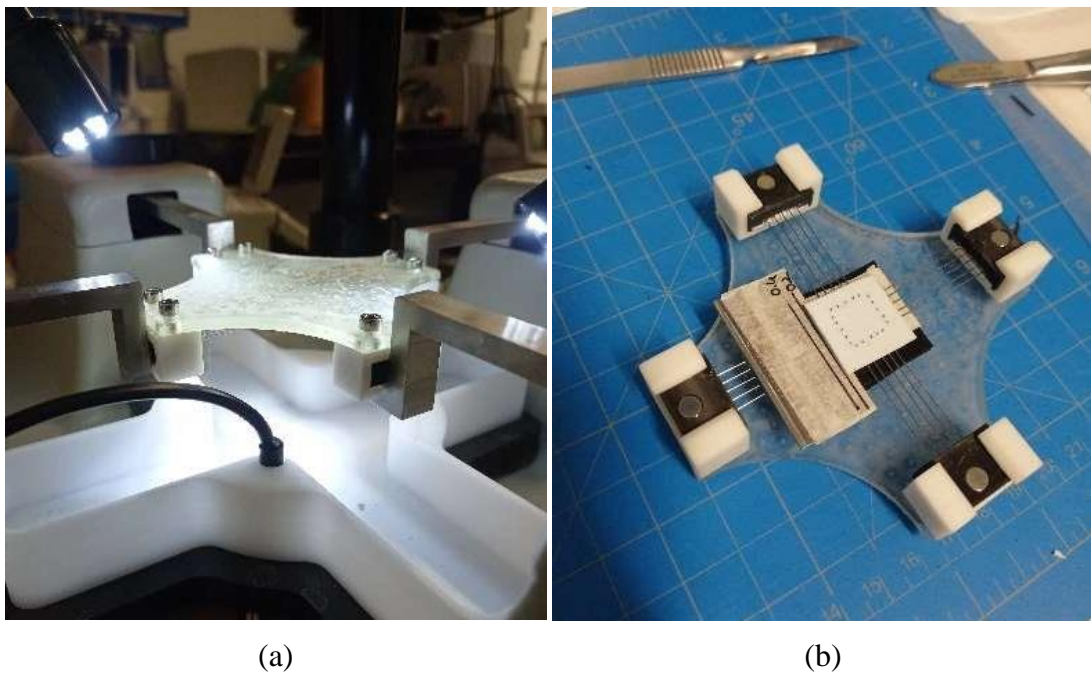


Figure 34 a) Lifting system, b) Specimen cutting

To apply the DIC technique the pictures were processed on Ncorr [3]. In particular, a ROI was selected adjacent to the rakes, applying a subset of 15-18 pixels, subset spacing 50% of the subset and a VSG of 3 (parameters described in section 3.2.1.1). During the whole test specimen pictures were acquired with a frequency of 5 Hz.

True stress - true strain curves were obtained for each specimen. The DIC strain map ε_{xx} , ε_{yy} were mediated respectively in x and y direction in a square region of side equal to 30 % of the gauge length, in order to be sufficiently far from the rakes. The true stress, instead, were obtained from the force, assuming volume conservation* as in equations 25 and 26. Moreover, because of the isotropic material, results in the x and y direction were mediated, obtaining an overall result:

$$\sigma_{xx} = \frac{F_x \cdot (l + d_x)}{l^2 \cdot t} \quad 25$$

$$\sigma_{yy} = \frac{F_y \cdot (l + d_y)}{l^2 \cdot t} \quad 26$$

where F_x , F_y , d_x , d_y are the force obtained from the load cells and the rakes displacement in x and y direction respectively; l is the initial gauge length and t is the initial thickness.

Simulation setup

The experimental tests were simulated numerically by means of finite element analysis, using the commercial FEA package Marc mentat a solver specifically

* This condition, usually assumed valid in constitutive models commonly adapted for the modelling of rubberlike materials and soft tissues, was verified to be valid by analysing the thermographic signal emitted by a silicone and a pericardial specimen under cyclic loading. It was evidenced that the thermal signal emitted from both samples was negligible confirming that no change in volume occur.

developed to model nonlinear phenomenon and severe contact conditions [113]. As shown in Figure 35a, the symmetry of the specimen was exploited modelling just one-eighth of the geometry. The solid model was created with a thickness of 1 mm and outer frame of: 5 mm, 3 mm, 1 mm, and with trimmed configuration. Furthermore, in order to identify the effect of the trimming, it was simulated a specimen with the trimmed shape starting from an outer frame of 5 mm (wide trimmed specimen in Figure 35b).

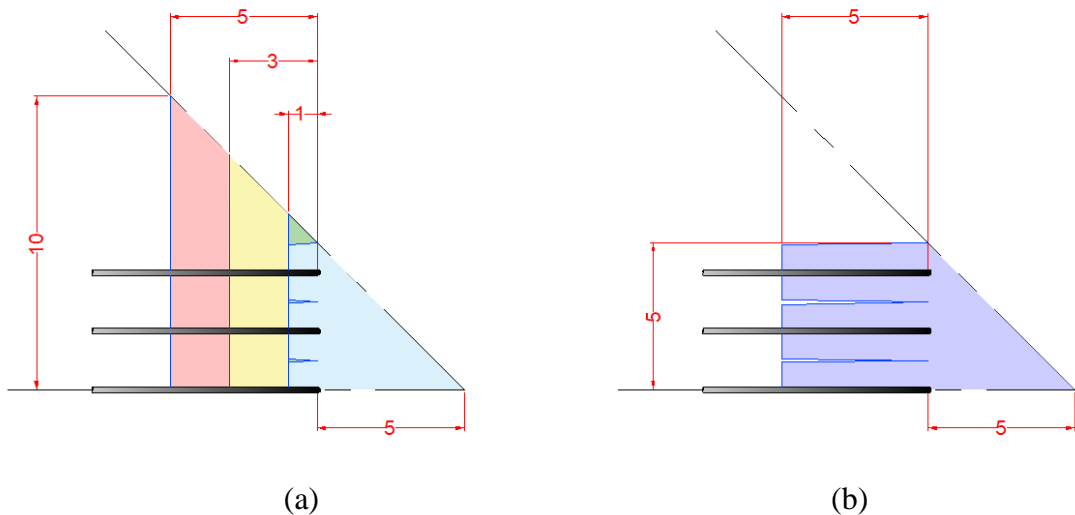


Figure 35 Simulation design a) wide, medium, small and trimmed specimen; b) wide trimmed specimen

The wide specimen and rakes (simulated as cylinders) were structurally meshed with about 50000 elements (mesh in Figure 36). To reproduce the sequence of experimental tests, keeping unchanged the mesh, all the shape were obtained starting from the wide specimen simply erasing 2 mm of element at the edges to reproduce the medium specimen and 4 mm in the case of small specimen. The trimmed shape was obtained removing from the small and wide specimen the corners elements and disconnecting the elements between the rakes by duplicating the nodes at the interface.

As material for rakes was set an Elastic-plastic Isotropic steel (Young modulus equal to 210000 MPa and Poisson ratio equal to 0.3) and for the specimen was set an Ogden material. To set the material coefficients, three dog-bone GI-1100 silicone uniaxial specimen were created, following the norm ISO 37 [114] specimen type 3, with the following dimension: gauge length (l) of 16 mm, width (w) of 4 mm and thickness (t) respectively of 1.148, 1.16, 1.23 mm.

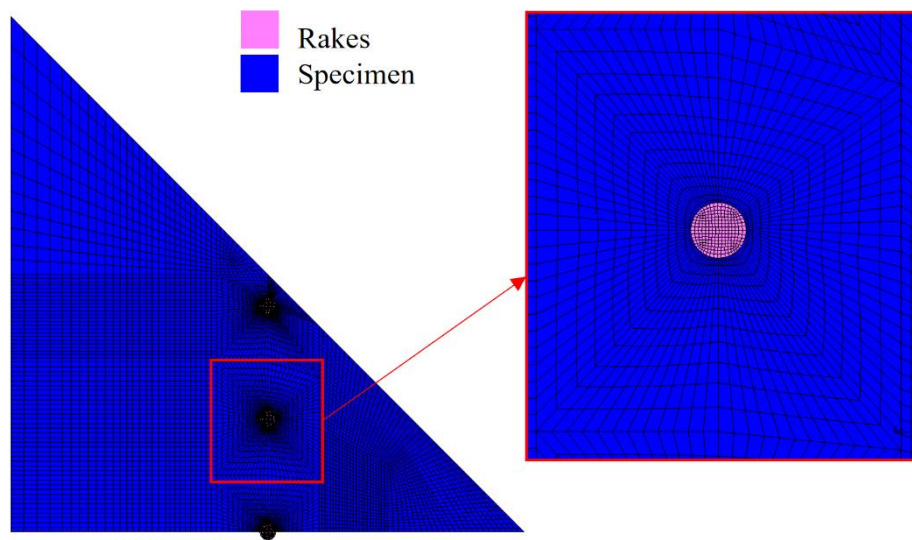


Figure 36 Wide specimen and rakes structurally meshed

These were tested to failure in an Instron 5943 uniaxial tensile machine in displacement control at a speed of 6 mm/min. The displacement (d) and force (F) data output were converted respectively in nominal strain and nominal stress as in equation 27 and 28.

$$\varepsilon = \frac{d}{l} \quad 27$$

$$\sigma = \frac{F}{w * t} \quad 28$$

The resulting nominal stress-strain curve mediated in all the uniaxial specimen was fitted with an Ogden model [115,116] that has 3 terms of the strain energy potential in the following equation:

$$W_{Ogden} = \sum_{i=1}^N \frac{2\mu_i}{\alpha_i^2} (\bar{\lambda}_1^{\alpha_i} + \bar{\lambda}_2^{\alpha_i} + \bar{\lambda}_3^{\alpha_i} - 3) \quad 29$$

where $\bar{\lambda}_1$, $\bar{\lambda}_2$ and $\bar{\lambda}_3$ are deviatoric principal stretches, μ_i and α_i are respectively moduli and exponent material parameter and N is the number of terms. The constant coefficients μ_i and α_i obtained in Abaqus hyperelastic material constants evaluator were imported in Marc.

The contact interaction between specimen and pins was set with 0.01 mm of interference and with a friction coefficient of 0.3. Each pin was moved applying a displacement ramp from 0 mm to 1.25 mm in the x direction and was left free to move in y direction.

To compare the numerical result with the experimental one, true stress - true strain curves were calculated. In particular, true stress was obtained as in equation 27 in which F is the contact force between rakes and specimen and d is the rakes displacement. Instead, as true strain was reported the strain of the central node. Furthermore, the stress strain curve associated to the central node that should represent the theoretical result.

Results

Three square silicone specimens were biaxially tested and cut in sequence four times. The strain map of each specimen were detected at different instant of the test by DIC technique. Then the experimental tests were reproduced in a Marc mentat

simulation. The Ogden experimental coefficients (of equation 29) used to reproduce the experimental material obtained from the uniaxial test were: modules $\mu_1 = 0.513517$; $\mu_2 = -0.376893$; $\mu_3 = -0.0156775$ and exponents $\alpha_1 = 4.65468$; $\alpha_2 = 4.89059$; $\alpha_3 = -0.600207$.

In Figure 37 are represented all the experimental and numerical ε_{xx} strain maps at the maximum displacement. In particular, the experimental maps (in Figure 37a,c,e,g), are referred to one of the three specimens (these are well representative of all tests, as they appear similar among them independently of the outer frame dimensions). The strain in the central region appears uniformly distributed and the highest and lower value of strain are located close to the rakes. Similar results are found also for numerical results (in Figure 37b,d,f,h), for which the highest and lowest values of strain are located close to the rakes and the uniform value of strain characterises the central region which expands with of the outer frame dimension decrease. A homogeneous strain map is obtained also for the wide trimmed specimen (in Figure 38). In fact, it presents a distribution of strain very similar to the trimmed specimen (in Figure 37h). Furthermore, true stress – true strain curves for all the outer frame cases are reported, for the experimental test in Figure 39a and for the numerical simulation in Figure 39b. In the experimental cases, as previously noticed, the maximum strain results are quite similar for all the cases, while the stresses values are different and decrease with the dimension of the outer frame. In Figure 39b the numerical curves show the same trend. Moreover, it can be noticed that curves related to the wide trimmed specimen and the trimmed specimen are overlapped and are the closest to the theoretical result.

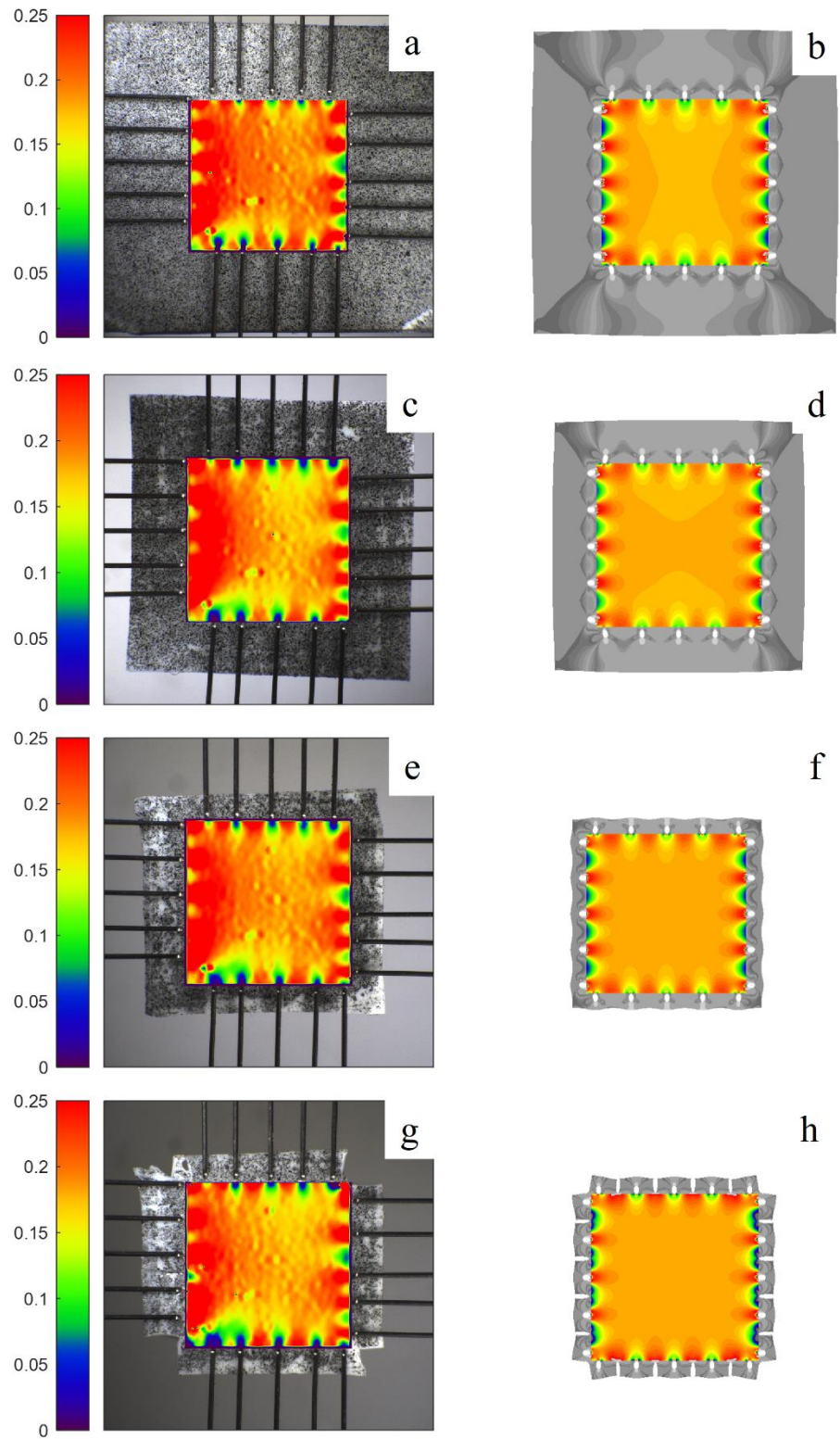


Figure 37 ϵ_{xx} strain map of: wide specimen a) experimental, b) numerical; medium specimen c) experimental, d) numerical; small specimen e) experimental, f) numerical; trimmed specimen g) experimental, h) numerical;

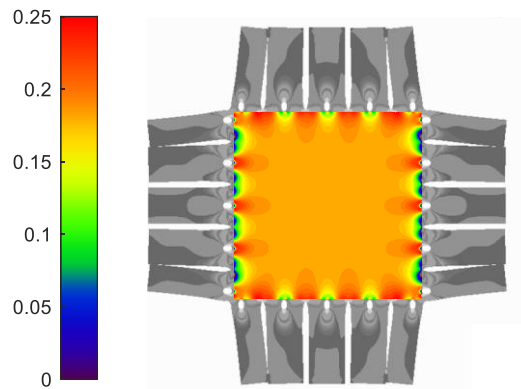


Figure 38 Numerical wide trimmed specimen ϵ_{xx} strain map

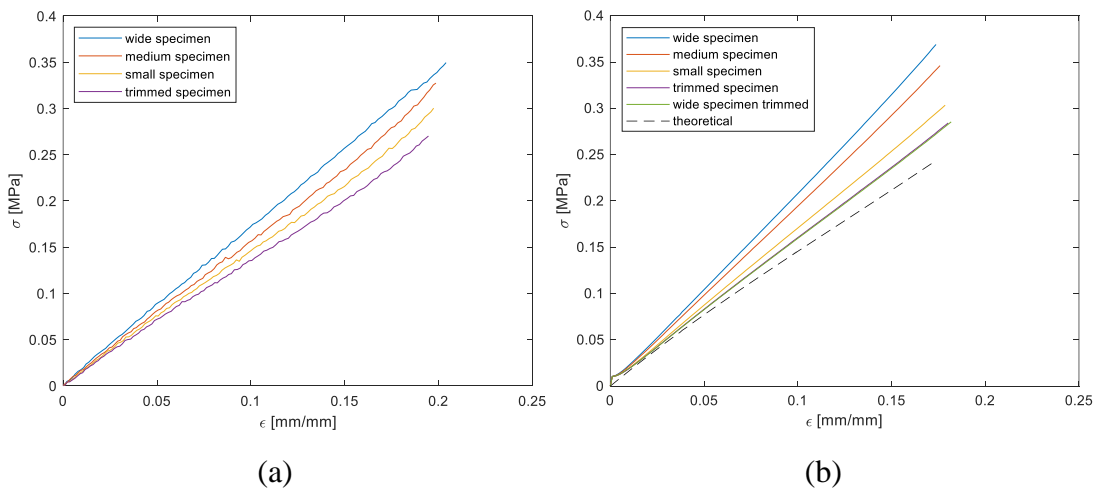


Figure 39 True stress strain curves a) experimental; b) numerical

In Table 3 the maximum value of stress are reported for each case and their distance from the theoretical result (expressed as a percentage). On average the experimental results are lower than the numerical ones, probably because in the experimental cases the outer frame instead of stretching in the plane tend to bend in z direction (as shown in Figure 40), reducing the load on the rakes. This effect, shown in all the experimental specimens, is more evident for higher frame dimensions. In the numerical cases it was not found because associated with instability phenomena not implemented in the simulations.

Table 3 Maximum value of stress for all the cases

<i>Specimen</i>	<i>Maximum stress [Mpa] (Distance from theoretical result [%])</i>	
	<i>experimental</i>	<i>numerical</i>
<i>Wide</i>	0.350 ± 0.023	0.369 (53 %)
<i>Medium</i>	0.325 ± 0.027	0.346 (44 %)
<i>Small</i>	0.300 ± 0.025	0.303 (26 %)
<i>Trimmed</i>	0.270 ± 0.026	0.284 (18 %)
<i>Wide trimmed</i>	-	0.285 (18 %)
<i>Theoretical</i>	-	0.241

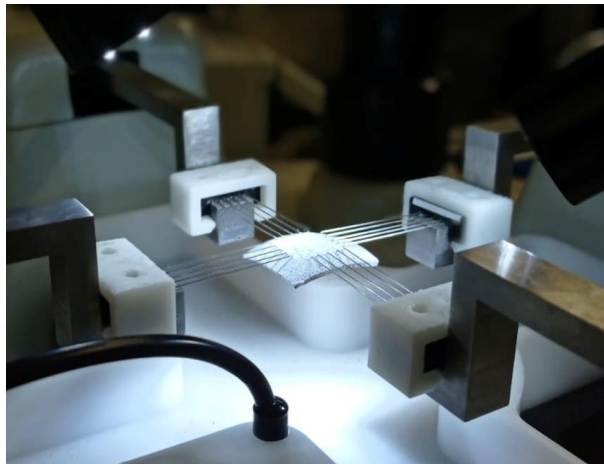


Figure 40 Specimen bending during traction test

Conclusion

Current testing practice for the determination of the biaxial material response of rubber like materials and soft tissues is inaccurate and may leads to overestimate the theoretical response above to 50 %. This may have strong implications in the design of bioprosthetic and polymeric heart valves, where the function components (the flexible leaflets) rely on the properties of these materials.

In particular, the experimental and numerical tests supported by DIC analysis have identified as source of error the outer frame dimension which has a direct effect

on the measured stress. The study, supported by FEA simulation, has also allowed the design of solutions of easy implementation. The shape that presents the closest value of stress to the theoretical result is the trimmed one. In fact, the trimmed specimen and the wide trimmed specimen results are almost the same. This implies that the trimmed shape stress is independent from original specimen dimension before the cutting procedure. Trimmed shape is a much simpler solution, as larger specimens are easier to cut and grip. This result suggests that the current centring of the sample, which usually represent a difficult task may become irrelevant on the accuracy of the results. The trimmed shape may also help in cause of tilted specimen.

In summary, the application of DIC, supported by FEA, has allowed to identify the limitations of current biaxial testing on critical biological soft materials and identify solutions that substantially improve the test results.

4.2 Complex fluid-dynamics

The use of Image Correlation techniques applied to investigate complex physiological flow such as aortic root can be crucial. Aortic root flow is particularly complex due to its anatomy and level of pressure (one of the most critical), and in the meantime essential for the correct aortic valve functioning. In this thesis it was verified the potential of PIV technique in this complex benchmark. A set of fluid-dynamics characterisation were performed on healthy native valve to understand the influence of Valsalva sinuses by means of valve sparing technique *ex vivo*. Then PIV technique was used in a non-conventional application for the direct measurement of the EOA. This study leads to identify significant limitation related to PIV feasibility and image

distortion due to refractive index mismatching. PIV feasibility was analysed generating PIV experiments from computational simulations based on Lagrangian SPH. Then, to reduce image distortion an image correlation function was used to find a new test fluid (composed of PBS and Propylene glycol) that match human blood density and viscosity, and silicone refractive index.

4.2.1 Analysis of healthy native aortic valve (and effects of alterations – valve sparing technique ex vivo)

Application of PIV technique to the investigation of the flow into the aortic root requires the manufacturing of optically transparent phantoms replicating the essential features of the native anatomy. This, as described in section 2.1.2, comprises the valve leaflets and a number of anatomical structures, such as the Valsalva sinuses. These, due to their complex three-dimensional shape, may introduce a number of errors associated to inaccuracies in the refractive index matching between the phantom material and the test fluid (see section 4.2.3.2). In order to get insight on the function of the native aortic valve and verify if the presence of the Valsalva sinuses is essential to model the valve operating mechanism or can be neglected, a study of the native aortic root and the changes produced by its alterations was performed. To this purpose, in collaboration with the University Hospital Policlinico Paolo Giaccone, Palermo (Mr Vincenzo Argano, Head of Cardiac Surgery), the hydrodynamic performance of a healthy porcine aortic valve was tested in the native aortic root and after three valve sparing surgical procedures. These consist in the replacement of the aortic root with artificial grafts, preserving the native valve cusps so as to restore the valve

functionality whilst avoiding the risks associated with the implant of a mechanical or biological valve prosthesis. In particular, valve-sparing aortic root replacement operations can be subdivided into two general families: the Yacoub *remodelling* and the David *reimplantation* procedure [117]. The main difference between them is that in *reimplantation* a straight graft is sutured drawing a circle along the aortic annulus, while in *remodelling* a straight graft is sutured drawing a three-pointed crown following the leaflets attachment to the ascending aorta. In both cases, the Valsalva sinuses are removed, and replaced by a tubular graft which do not reproduce their bulges. More recently, grafts with a bulge in correspondence of the native sinuses have been introduced by De Paulis, the most common of which is the Gelweave Valsalva™ conduit, Vascutek Ltd. Although it is claimed that this may contribute to maintain the physiological aortic hemodynamic [118].

The optimal conduit for valve-sparing aortic root replacement is still debated [119]. Some studies report a better long-term stability of the David straight grafts, related to the fact that this procedure constrains the native annulus into the graft, preventing dilatation and aneurism. Nonetheless, for the associated removal of the Valsalva sinuses has been associated with potentially suboptimal hemodynamic than what can be achieved with bulged grafts [120,121]. *Pisani et al.* compared De Paulis graft against straight graft, finding that the presence of Valsalva sinuses has a key role in stabilising the pressure gradient across the valve in case of increasing cardiac output (CO), by way of an increase of the effective orifice area [122]. Similar finding were reported by *Tango et al.* who used fluid-structure interaction (FSI) models, validated with *in vitro* findings, demonstrating that the valve leaflets open into the sinuses enlarging the effective orifice area [123]. More recently, *Paulsen et al.* questioned

these findings by presenting *ex vivo* experiments comparing 5 techniques of valve-sparing, and showing that straight grafts result in closer performance to native aortic root than bulged grafts [119,121].

These controversial results indicate that the role of Valsalva sinuses is still unclear and further studies are needed to gain a better comprehension. In this context, this study aims to elucidate the bio-mechanical mechanism underlying native aortic valve performance by means of *ex vivo* experiments to compare different valve-sparing implants. This would provide essential indication on the level of detail required in the creation of a phantom of the aortic root (i.e. need to include the sinuses, effect of the root compliance) for the present study. More importantly, the study has major clinical implications, as it can help to clarify the hydrodynamic changes produced by the different valve sparing techniques, suggesting optimal procedures. Two porcine aortic roots (Medtronic FreeStyle) of size 25 mm were used to represent the native healthy case. Each of these was then implanted with three different grafts, following a specific sequence of techniques, David, Yacoub and De Paulis. All implants were conducted by the same expert cardiac surgeon, to reduce the variability in the replacement techniques. All four configurations for each prosthesis were tested on a Pulse Duplicator, to evaluate the hydrodynamic performances.

Prosthesis implants

Two FreeStyle (MedTronic) of size 25 mm (corresponding to the annulus diameter), were selected to represent healthy physiological case (see Figure 41). They were then used to perform a sequence of three surgical techniques of replacement,

executed in series by the same surgeon, following the order: David, Yacoub and De Paulis.

Before the implants each graft was prepared for the experimental test by washing out the collagen coating and dipping it in a silicone suspension (1-2577 Low VOC) to make it impermeable to Phosphate Buffered Saline solution (PBS) for the fluid-dynamic measure acquisition.

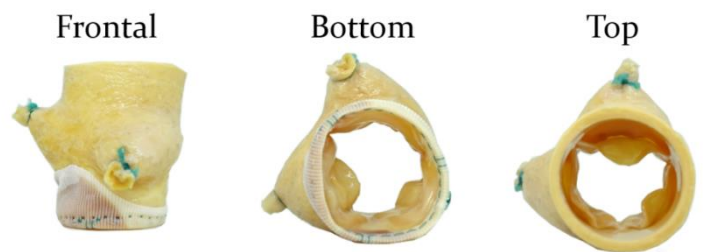


Figure 41 FreeStyle (Medtronic) prosthesis. Frontal, Bottom and Top views.

For the David implant, a straight graft made of surgical PET knitted fabric (Intergard) of 28 mm was used. Firstly, the surgeon excised the three cusps keeping a border of about 5 mm beyond the three pointed crown of leaflet attachment line. Successively, he sutured the straight graft with the porcine valve stitching it at the annulus level and at the three pointed crown (see Figure 42) [124]. The graft was then cut above the sinotubular junction and the three commissures (junction points between two adjacent leaflets) were secured to the Dacron graft with pledgets (strengthening devices for sutere).

The Yacoub implant was directly derived from the David's configuration. In fact, the two techniques are identical except for the inferior cut of the graft, which is a circular line in the David case and a three-pointed crown in the Yacoub case. Thus, in this case, the draft is fixed to the aortic valve only in correspondence of the leaflet

attachment line. To obtain this implant, the surgeon just removed the suture points at the aortic annulus and trimmed a three-pointed crown under the sutured line of the leaflet attachment.

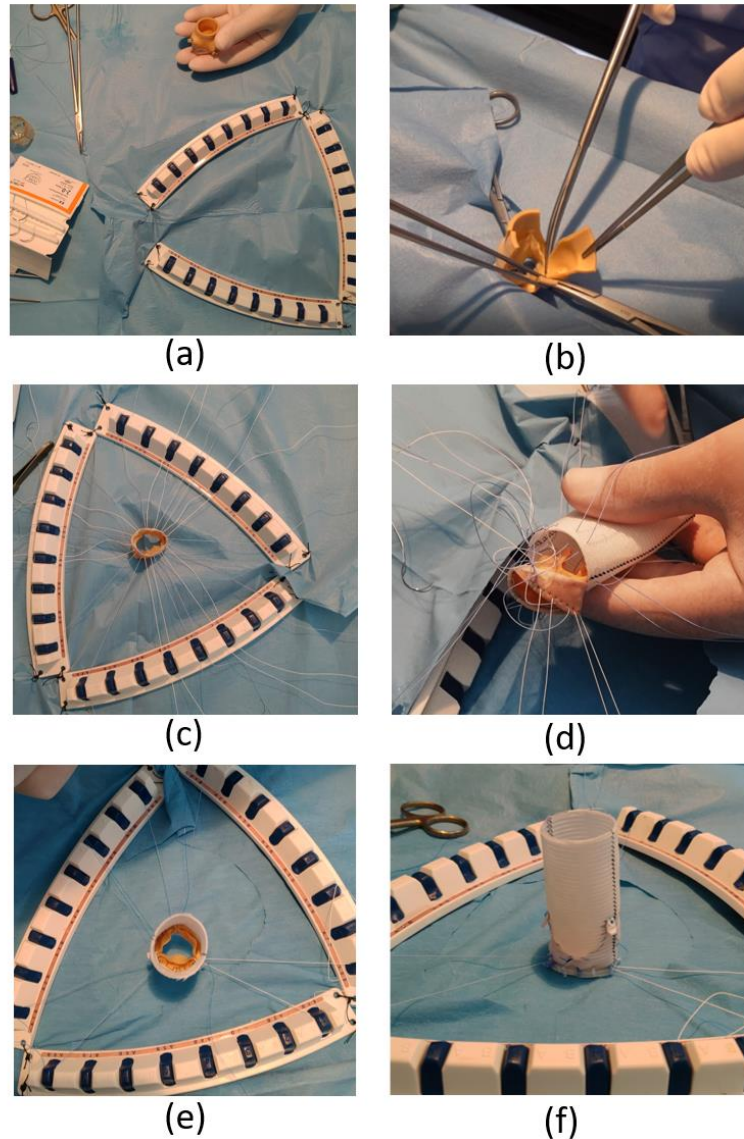


Figure 42 David implant step by step: (a) equipment, (b) FreeStyle cutting, (c) valve preparation, (d) graft positioning, (e) graft suturing, (f) final implant.

For the De Paulis implant, the straight graft was removed from the porcine valve, the latter, successively, was sutured along the annulus to a Gelweave Valsalva™ graft in surgical PET knitted fabric of 26 mm diameter [118].

The Freestyle valve and all the three implants were fixed to a specifically designed resin support, obtained by a stereolithography 3D printer Formlabs, in order to be integrated into the Pulse Duplicator for the hydrodynamic assessment (see Figure 43).

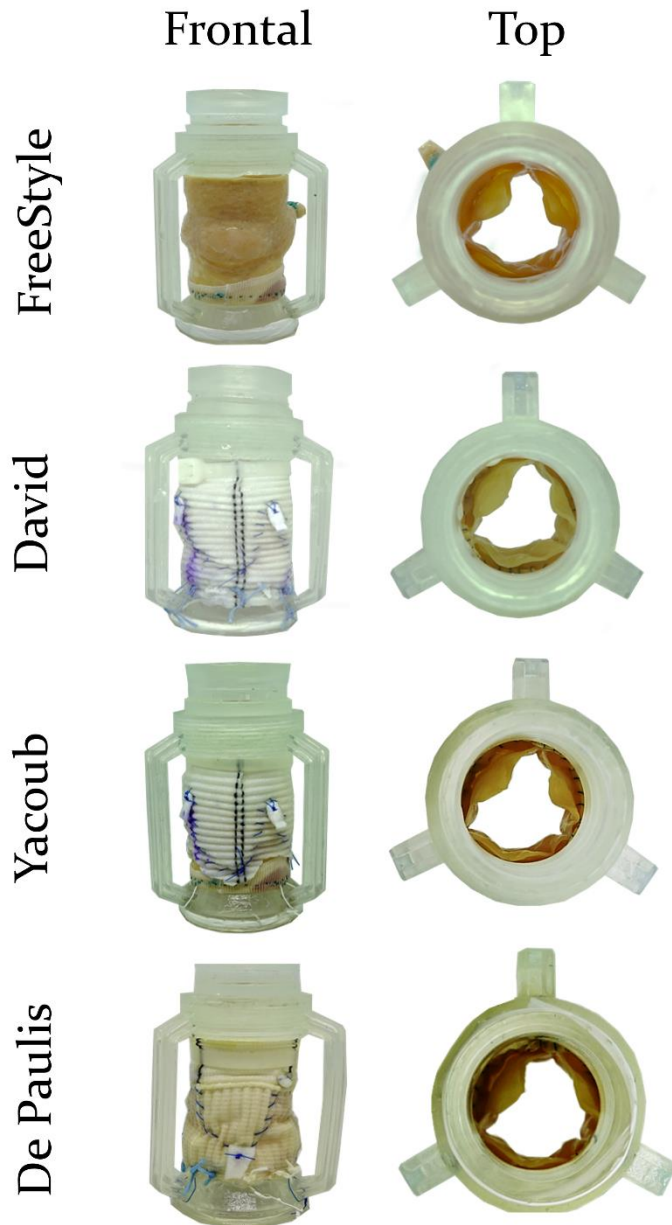


Figure 43 FreeStyle prosthesis and the three valve-sparing implants, David, Yacoub and De Paulis, set into resin support.

Test in vitro

The hydrodynamic performance assessment of each implant was conducted *in vitro* using a cardiovascular pulse duplicator system ViVitro (described in 3.3.1).

In this study, the system was used to reproduce the physiological circulatory system of the left heart, therefore the fluid flow from the left atrium to the left ventricle is regulated by the mitral valve, while the fluid flow from the left ventricle to the aorta is regulated by the aortic valve. The implants were tested in aortic position (mounting the implants support in place of the aortic root in Figure 13) while a St. Jude 29 mm bileaflet mechanical valve was used in mitral position. For each test ten consecutive cycles were recorded. In compliance with the *in vitro* test procedure of the International Standard ISO5840 [54], tests were carried out simulating six cardiac outputs (2, 3, 4, 5, 6, and 7 l/min) at a normal heart rate (70 bpm and systolic duration of 35%) at room temperature, applying 100 mmHg of mean aortic pressure. The test fluid was PBS.

The flowmeter and pressure transducer outputs were used to obtain the implant performance parameters (exposed in section 3.3.1). In particular, the Mean Systolic Transvalvular Pressure Drop (mean value of pressure difference across the aortic valve), the closing regurgitant Volume (calculated as the integral of the flow curve during the closing valve period), the Energy loss (calculated by adding up the forward and the closing energy loss contributes), and the EOA (calculated by the Gorlin equation as in equation 11 were determined for each test.

Results

In Figure 44 all the performance parameters of each implant are reported, each column corresponds to a prosthesis. In Figure 44a,b the mean systolic transvalvular pressure drop are reported. For both valves the healthy case (represented by the freestyle curve) presents the best performance, with the lowest value of pressure drop followed by the De Paulis implants, that present an intermediate behaviour for high value of Cardiac Output, and then Yacoub and David, whose performance are similar. The trend is confirmed by the Effective Orifice area, in Figure 44c,d. In fact, the two Freestyle present the largest area, followed by the De Paulis implants. David and Yacoub are mostly overlapping at high value of Cardiac Output. The closing volume, reported in Figure 44e,f, shows an increasing trend of the absolute volume in case of valves with aortic compliance. In fact, the David implants present the lowest increasing rate. Finally, the Energy loss in Figure 44g,h, shows that the native valve is more efficient for all the cardiac outputs followed by the De Paulis implants. The David and Yacoub implants have similar behaviour.

In Table 4 the performance value related to the standard Cardiac Output (5 l/min) are reported [78]. As expected, the Freestyle prostheses, that replicates the native valve in healthy conditions, are characterised by the best performance parameters. In fact, for both the prostheses (SN4 and SN5), the largest EOA, the lowest pressure drop and the lowest Energy loss are obtained. Instead, the closing volume results are on average higher than for the valves after surgical procedures. This is common for larger valves, and is probably due to the fact that the valve, attached to the native compliant root, can

expand more in the Valsalva sinuses [104], necessarily allowing a higher backflow during the closing phase.

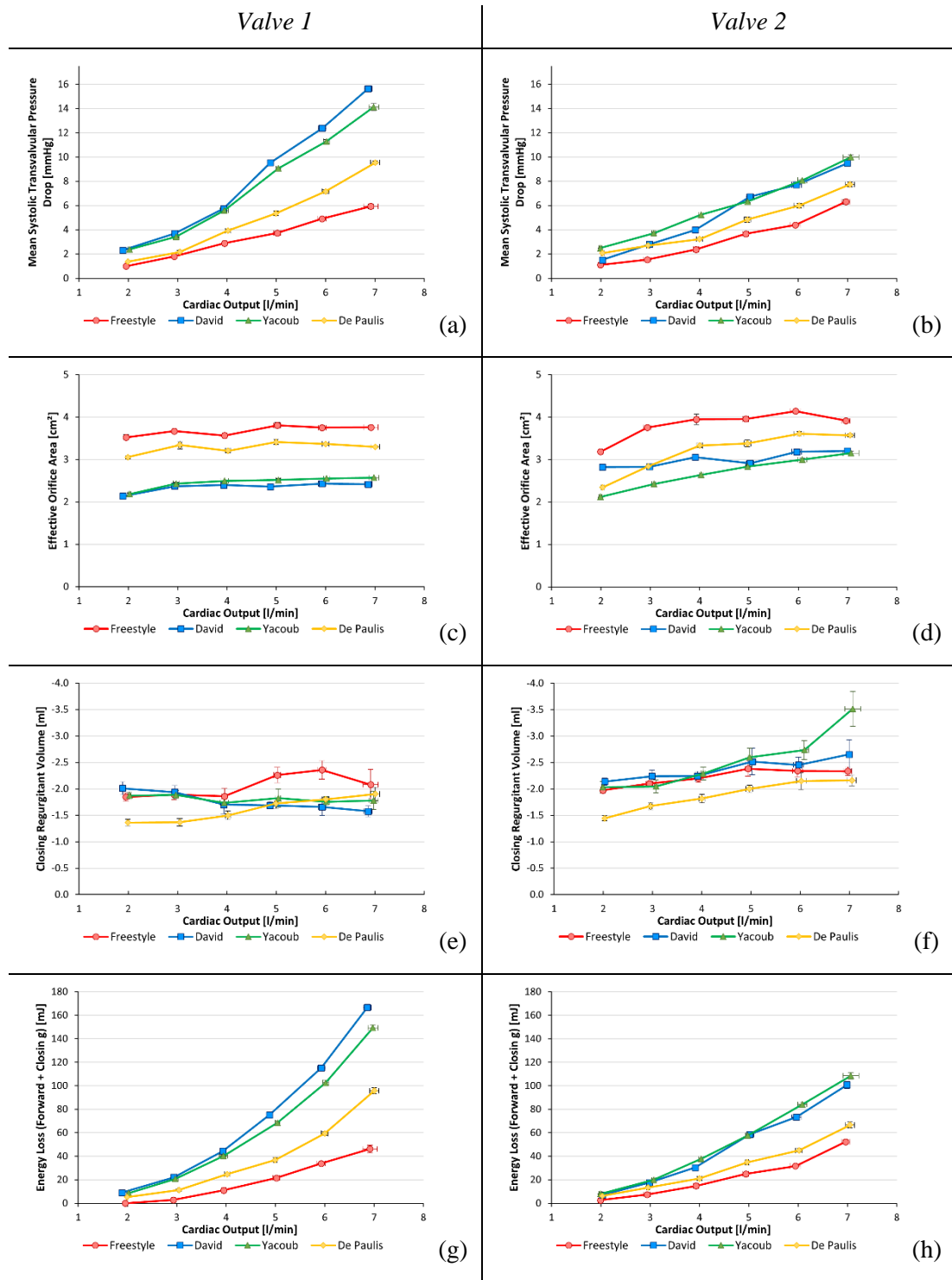


Figure 44 Implant performance parameter diagram of: a) mean systolic transvalvular pressure drop (SN4); b) mean systolic transvalvular pressure drop (SN5); c) Effective orifice area (SN4); d) Effective orifice area (SN5); e) Closing Regurgitant volume (SN4); f) Closing Regurgitant volume (SN5); g) Energy Loss (Forward + Closing) (SN4); h) Energy Loss (Forward + Closing) (SN5)

Table 4 Implant performance parameter at 5 l/min of Cardiac Output

Valve	Implants	Cardiac Output [l/min]	Mean Systolic Transvalvular Pressure Drop [mmHg]	Effective Orifice Area [cm ²]	Closing Regurgitant Volume [ml]	Energy Loss (Forward + Closing) [mJ]
1	Freestyle	5.02 ± 0.07	3.74 ± 0.12	3.81 ± 0.07	-2.26 ± 0.15	21.60 ± 1.07
	David	4.88 ± 0.03	9.53 ± 0.25	2.36 ± 0.02	-1.69 ± 0.07	75.05 ± 1.50
	Yacoub	5.04 ± 0.05	9.07 ± 0.14	2.52 ± 0.02	-1.83 ± 0.17	68.47 ± 1.63
	De Paulis	4.99 ± 0.03	5.36 ± 0.19	3.41 ± 0.06	-1.72 ± 0.09	36.81 ± 1.94
2	Freestyle	4.94 ± 0.06	3.66 ± 0.1	3.96 ± 0.5	-2.38 ± 0.14	25.03 ± 1.08
	David	5.02 ± 0.08	6.73 ± 0.07	2.91 ± 0.01	-2.52 ± 0.25	58.70 ± 1.54
	Yacoub	4.97 ± 0.04	6.32 ± 0.09	2.84 ± 0.02	-2.60 ± 0.17	57.65 ± 1.66
	De Paulis	4.97 ± 0.07	4.84 ± 0.23	3.38 ± 0.08	-2.00 ± 0.07	34.87 ± 1.06

Comparing all the implants Yacoub and David present similar results, and the De Paulis results in enhanced results at high cardiac output. In fact, it has intermediate characteristics between the Freestyle prosthesis and the Yacoub and David implants. Of note, these results are confirmed for both the prostheses analysed.

The results suggest a role of the Valsalva sinuses very different from that most commonly accepted in the literature [6,125,126], where these chambers are usually claimed to allow the formation of blood vortices that promote the prompt valve closing. On the contrary, the beneficial effect of the sinuses on the closing does not appear evident (surprisingly, closing leakage is larger for the native configuration than for the modified valves). Instead, the role of the Valsalva chambers appears to be supporting the systolic phase, by allowing leaflets to expand into the sinuses, thus reaching larger EOAs and minimum pressure drops. Optimisation of this phase, in fact, is energetically more convenient, as associated with greater energy losses. Interestingly, similar conclusions were recently proposed by *Tango et al.* [123], on the basis of computational simulations of idealised aortic root models.

Still, including the Valsalva sinuses in the aortic phantom appears essential to capture the correct hemodynamic that establish in the aortic root during systole.

Conclusion

From a clinical perspective the De Paulis implant resulted better performing than those based on tubular grafts, probably because is the one that better reproduce the anatomy of the sinuses [122] and their function on the valve opening. It is important to observe that this result does not confirm the latest reports in the literature [119,121]. This incongruence can be reconducted to the different positioning of the commissures that, contrary to previously published *in vitro* tests, our clinical collaborator sutures above the sinuses, at the sinotubular junction. This results in more anatomical configurations, where the valve commissures are constrained during diastole, limiting infra-valvular leakage.

4.2.2 *EOA direct measurement (PIV)*

The Effective Orifice Area, as described in section 3.3.1, is one of the most fundamental clinical parameters used to quantify the valve performance. EOA depends on multiple factors, such as left ventricle function, transvalvular pressure drop Δp and leaflet mobility. A stenotic valve (in Figure 45) presents a narrowed zone at the leaflet edge called geometric orifice area (GOA) that causes a flow acceleration from the left ventricle outflow tract (LVOT) to the *vena contracta*, whose cross section is directly quantified by the EOA. The jet flow in the ascending aorta (AAo) decelerates,

converting some of the kinetic energy into potential energy that causes a local increase of pressure.

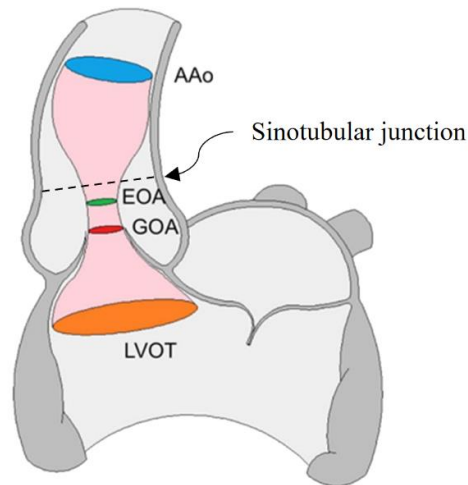


Figure 45 Schematic flow through a stenotic aortic valve [127]

EOA parameter is usually preferred, compared to GOA, to assess the flow properties [128]. As described in section 3.3.1, EOA can be estimated from pressure and flow measurement through the Gorlin equation (equation 11) [79,129]. This is derived from the Bernoulli equation and the continuity equation, introducing empirical contraction coefficients that do not take in to account the type of valve or prosthesis.

Hence, the value of the EOA currently derives by an approximated equation, which does not take into account the valve positioning, the anatomy of the root, or the typology of valve or prosthesis [123,130–132]. As a result, the estimated value can be strongly approximated (especially at large and small valve diameters), and a number of corrective equations have been suggested [133–135].

In this work, a new approach is suggested, where the EOA is not estimated, but measured, by applying PIV in an alternative mode. This would represent a major improvement towards a more rigorous assessment of heart valve efficacy, and on their effect on the section flow. For this purpose, PIV technique was used to evaluate the

out of plane flow field in a transversal plane of the aortic root up to the sinotubular junction by focusing the attention to the zone of non-correlation.

Proposed approach

As described in section 3.2.1.2, the PIV technique needs a seeded test fluid for the application of cross-correlation functions. Seeds are chosen (in dimension and density) to follow the flow being measured. In standard 2D PIV applications, the laser sheet is aligned parallel to the principal component of velocity (v_z) in the flow direction, tolerating a small component in the transversal plane (v_{xy}), which cannot be detected by the technique.

In this thesis, an alternative approach is attempted to measure the EOA, where the laser is aligned with a transversal plane, orthogonally to the principal component of the jet velocity (v_z). In this case, if the laser sheet has a thickness l_t and the time step between the two images to correlate is Δt , seeds with velocity $v_z > l_t/\Delta t$ would not remain in the laser sheet for both pictures (as schematically described Figure 46). Hence, the cross-correlation applied on IRs characterised by $v_z > l_t/\Delta t$ would attempt correlation of seeds illuminated at time t with new seeds, illuminated at time $t + \Delta t$ (that were behind in the previous instant). The matching of different patterns of particles leads to find erroneous displacement and velocity components (v_{xy}), detected in the post-processing validation procedure as invalid vectors. Hence, analysis of the regions of invalid correlation can quantify the area of the main jet departing from the open aortic valve, where the axial velocity is $l_t/\Delta t$.

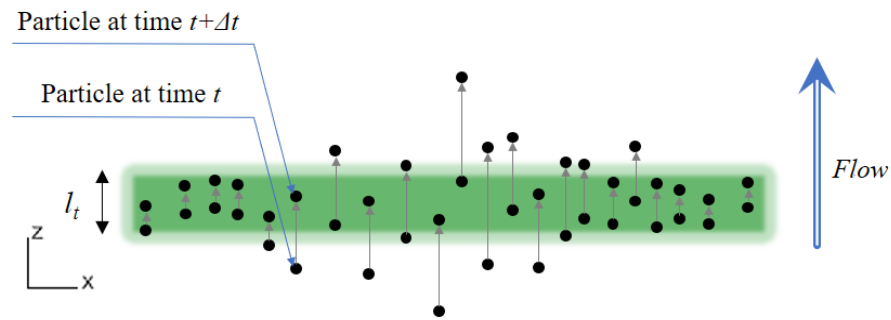


Figure 46 Particles movement in the laser thickness in an interval of time Δt

In fact, the systolic flow in the aortic root is characterised by a high velocity jet (v_{jet}) and a decreasing velocity towards the aortic root wall, in the axial direction. In this work, l_t and Δt were set in order to have $v_{jet} > l_t/\Delta t$. This setting should allow to identify the shape of the non-correlation area correspondent to the *vena contracta*.

Experiment setup

Aortic flow characterisation was performed applying PIV technique on the pulse duplicator system, where a silicone aortic root specifically designed and manufactured as part of this thesis was mounted in place of the glass aortic root in Figure 13. The aortic root phantom was made of Sylgard-184 silicone (in Figure 75), full manufacturing procedure is described Appendix C. St. Jude Medical bileaflet mechanical valve of size 25 mm (in Figure 4c) and Edwards Perimount valve of equivalent size (in Figure 5) were mounted in a customized aortic valve holder (in Figure 13). A mechanical bileaflet valve St. Jude Medical of size 29 mm was placed in mitral position.

In compliance with the *in vitro* test procedure of the International Standard ISO5840 [78] the test was carried out at room temperature, simulating a physiological cardiac outputs of 5 l/min, with a mean aortic pressure of 100 mmHg, at an normal

heart rate 70 bpm, applying a waveform FDA approved with a systolic duration of 35%. The test fluid used was PBS.

For PIV application, laser and camera were placed perpendicular with each other and close to the pulse duplicator in various configurations (for transversal plane as in Figure 48) acquiring for each valve two sagittal planes (S_1 and S_2) and one transversal plane (T) just up to the sinotubular junction (in Figure 47).

In order to measure the EOA, 100 pairs of PIV images were acquired at instant of maximum flow for each valve and configuration, with a Δt dependent on the mean velocity. In particular, a Δt equal to $80 \mu\text{s}$ was selected to analyse the sagittal planes, a Δt equal to $700 \mu\text{s}$ to analyse the transversal planes.

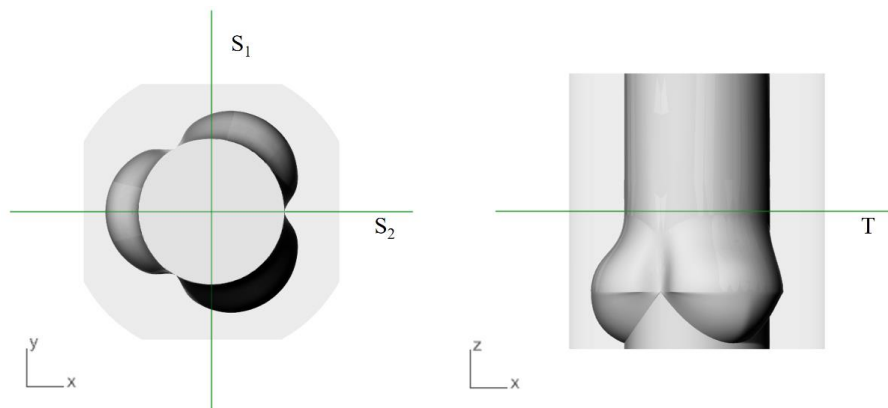


Figure 47 Sagittal planes (S_1, S_2) and transversal plane (T) identification

A different post processing was performed for sagittal and transversal planes. For sagittal planes, after the application of a low-pass filter, where the mean intensity was removed, the velocity field was obtained with a multi pass-processing (described in section 3.2.1.2). Then, a vector validation was applied on the vector field with a recursive filling of the invalid vectors, where the interpolated vectors and valid vectors are used to replace the invalid vector in several steps. The mean velocity field was then calculated in Tecplot. For the transversal planes, where the non-correlation is the

parameter to be detected, a low-pass filter was applied, followed by a single pass-processing and a vector validation. the vector validation was used to identify vectors that did not pass the validation criteria, they were replaced just where the neighbourhood were valid vectors. The resulting map were then processed in Matlab, looking at the Choice code (CHC) that identifies:

- Valid vectors (CHC=1), a high correlation peak is found;
- Invalid vectors (CHC=-1), vector did not pass a validation criteria;
- Interpolated vectors (CHC=4) vector replaced with the neighbourhood mean vector.

So, the non-correlation area is identified as region of invalid vectors, that have CHC equal to -1. To recognize non-correlation area in all the acquisition the CHC was reported as percentage. The chosen processing parameters were validated for each experiment.

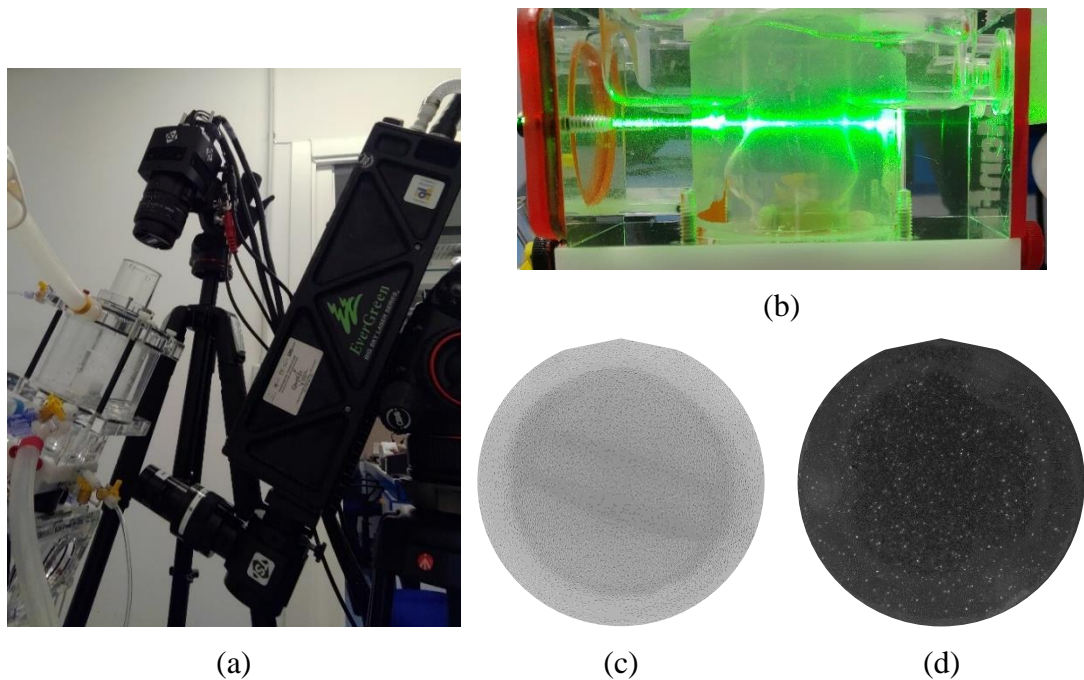


Figure 48 a) Setup for transversal plane, b) picture of the light sheet, c) mechanical valve view with the light on and laser off, d) biological valve view with laser on

Results

In Figure 49 and Figure 51 the velocity magnitude on plane S1 and S2 (shown in Figure 47) are reported, for the St. Jude mechanical valve and Perimount biological valve respectively. The velocity maps in sagittal planes present in both cases a higher velocity component above the aortic valve and lower velocity in the sinuses where vortexes are observed. Comparing Figure 49a and Figure 49b, it is evident that in the case of the mechanical valve the result depends on the observed plane. In fact, in Figure 49a the mechanical valve is perpendicular to S₁ plane, instead in Figure 49b the valve is aligned with S₂ plane. Figure 49a shows that the aortic outflow in the case of bileaflet mechanical valve is split into three main jets of which the central one presents a lower velocity compared to the external jets. Figure 49b shows a more homogeneous velocity map of the central jet. Furthermore, the two lateral jets have at the sinotubular junction (SJ) the higher velocity in the T plane (in Figure 50a). The areas where in T and S1 planes the higher velocity are measured, correspond to the areas of non-correlation (in Figure 50b). In Figure 50b, the percentage of invalid vectors is reported (valve alignment in Figure 48c), it can be noticed that, excluding the edge, the central area has the lowest percentage of invalid vectors, and the two jets have the higher percentage of invalid vectors.

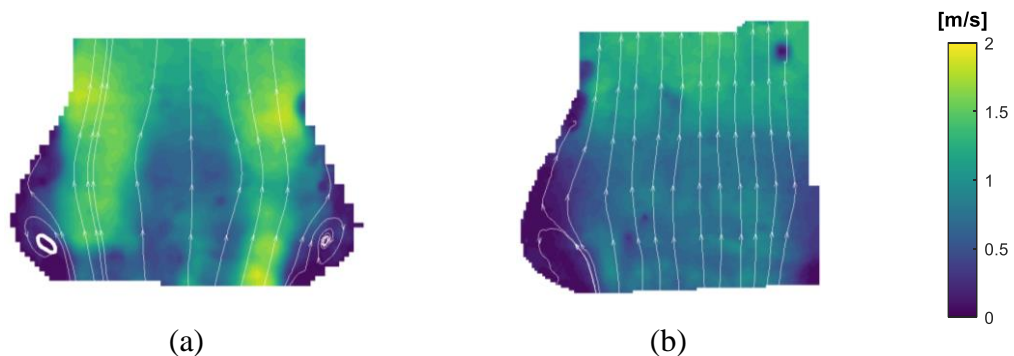


Figure 49 Velocity magnitude of st. Jude mechanical valve on plane a) S1, b) S2

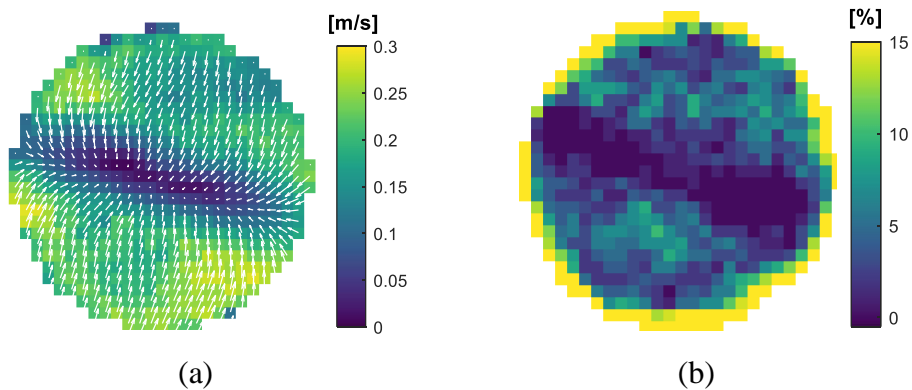


Figure 50 St. Jude mechanical valve a) velocity magnitude on T plane b) percent of invalid vectors (CHC=1)

The sagittal and transversal maps (in Figure 51a, b and Figure 52a), in the case of the biological valve, present a different pattern. Figure 51a, b show respectively S_1 and S_2 results that are quite similar because of the higher degree of axial symmetry of the valve (see Figure 48c). In particular, on both maps a central jet with the higher velocity and lateral vortex in the sinuses is shown. Figure 52a, b show that the lower amount of invalid vectors is concentrated in the central area, where the jet is perpendicular. In proximity of the wall, the transversal velocity increases with the number of invalid vectors.

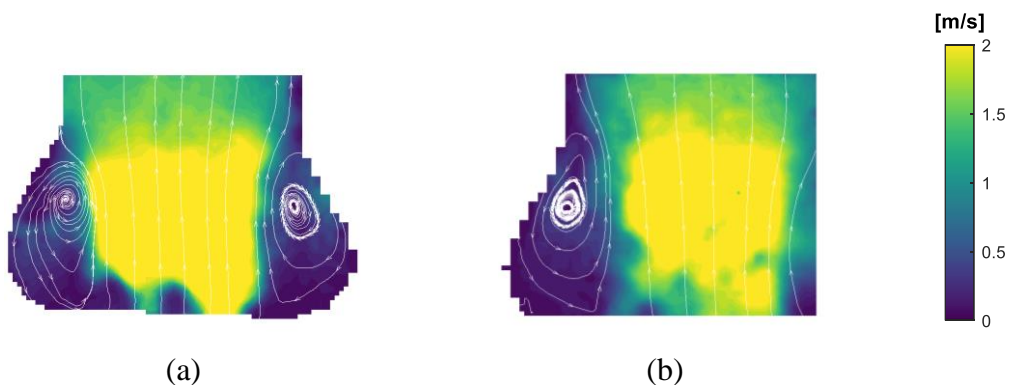


Figure 51 Velocity magnitude of Perimount biological valve on plane a) S_1 , b) S_2

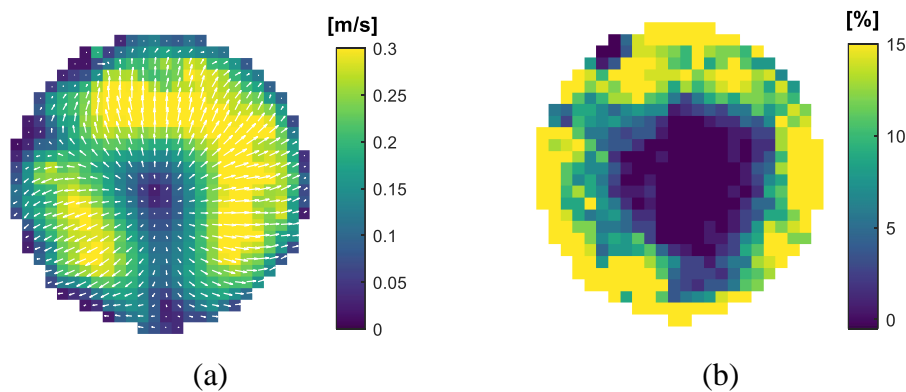


Figure 52 Perimount biological valve a) velocity magnitude on T plane b) percent of invalid vectors (CHC=1)

Conclusion

In conclusion, an experimental approach to measure the EOA is proposed. The approach is promising for the *vena contracta* direct measurement. In fact, its application on the sinotubular junction achieves maps of non-correlation (in Figure 50b and Figure 52b) related to the EOA and the valve positioning (shown in Figure 48c,d) which may serve as a basis for future studies. However, its application on the *vena contracta*, usually located just above the leaflets, may need a RI matching between the silicone root and the test fluid, because of the Valsalva sinuses geometry that with a non-matched RI may refract the laser light rays (investigated in section 4.2.3.2). Furthermore, the generation of *synthetic images* (investigated in section 4.2.3.1) may help to study the test feasibility and to identify the best experimental setup.

4.2.3 *Experimental issues*

PIV extends image correlation approaches to the determination of fluid dynamic parameters. However, in its application to complex cardiovascular flows, the technique

is necessarily affected by a number of approximations and experimental limitations, that need to be well understood in order to minimise their impact and expand PIV application to wider scopes. In the following sections some of the most common experimental issues are investigated.

4.2.3.1 *Experimental feasibility (SPH – PIV)*

PIV technique, as already described in section 3.2.1.2, allows to determine experimentally velocity distribution in fluid flows through the application of cross-correlation algorithms. With the evolution of numerical approaches, a common application of PIV has become providing an experimental validation to *in silico* models [136–138]. In order to rely on the methodology for this scope, the relationship between measurement errors and experimental parameters in complex flow conditions typical of cardiovascular setups needs to be better characterised [139]. In a number of previous works focused on aortic root flow, PIV technique has been applied to identify the full field velocity and derive from the velocity distribution and fluctuations other fluid-dynamics parameters such as shear rate, shear stress, turbulent kinetic energy and distribution of turbulent flow [140–144]. In this context, the uncertainty estimation is a critical aspect for the PIV result interpretation. In a PIV experiment, velocity fields are obtained by measuring, for each interrogation region (described in section 3.2.1.2), the particles displacement (Δx) in a time interval (Δt), as in equation 30:

$$u = \frac{\Delta x}{\Delta t} = \frac{\Delta X}{M\Delta t} \quad 30$$

where M is the magnification factor that allows to convert the image displacement (ΔX) from pixel to physical unit. The uncertainty of the estimated velocity [145] can be expressed as:

$$\left(\frac{U_u}{u}\right)^2 = \left(\frac{U_{\Delta X}}{\Delta X}\right)^2 + \left(\frac{U_{\Delta t}}{\Delta t}\right)^2 + \left(\frac{U_M}{M}\right)^2 \quad 31$$

where $U_{\Delta X}$ is the uncertainty related to the measurement, $U_{\Delta t}$ is the uncertainty related to the laser pulse separation Δt (estimated 1 ns [146]), U_M is the uncertainty related to the magnification factor which depends on the camera view, the image distortion and spatial calibration.

The contribution of the parameters $U_{\Delta t}$ and U_M can be considered negligible when measurements require Δt larger than 100 μs and calibration procedure is conducted properly. Therefore, most of the investigations have focused on the measurement uncertainty $U_{\Delta X}$ which is commonly classified as *a priori* and *a posteriori*. *A priori* uncertainty quantification techniques usually employ theoretical modelling to identify PIV algorithm performance. Instead, *a posteriori* approaches analyse the uncertainty related to a specific case of study. In both cases, a valid instrument used to perform PIV simulation is the use of *Synthetic images*. *Synthetic images* are generated using a random distribution of virtual tracer particles with a prescribed motion, in which the key parameters of flow and particles pattern can be changed individually without modifying the other. The images are traditionally obtained with statistics methods as Monte Carlo simulations [147,148] or with Numeric flow simulations [149]. Even if Monte Carlo is the most used method, it tends to underestimate errors related to actual measurement condition. Nevertheless, it has demonstrated useful for experimental planning [150,151]. In other studies, CFD

simulations were used to generate synthetic images, employing known velocity field [147,152].

In this context, Smoothed-particle hydrodynamics (SPH) is proposed as a new method to generate *Synthetic Images* for complex fluid-dynamics uncertainty quantification. SPH is a Lagrangian mesh-free method used for simulating fluid flows, in which the system is represented by a set of particles. Each particle has material properties and moves according to the Navier Stokes equations. At each particle position, hydrodynamic variables such as velocity and pressure fields are obtained using discrete convolution integrals with filter functions [153]. Since SPH is a Lagrangian method, particles are tracked during all the flow evolution. Therefore, as part of this thesis it was attempted a new approach where a random set of SPH particles on a virtual laser sheet is visualised as seeds, so as to obtain ideal sets of PIV images. Moreover, for the same identical instants and flows, it is possible to generate a practically infinite combinations of virtual PIV images, with total control on the particle concentration and dimensions, on the sheet thickness and on the time intervals. A further advantage of this approach is that it allows to verify the potential maximum accuracy of PIV methods, by excluding the effect of a number of experimental sources of inaccuracy, such as optical aberrations associated with refractive index mismatches, particle size and transport phenomena, or density differences between the particles and the fluid.

The PANORMUS [154,155] (Parallel Numerical Open-source Model for Unsteady flow Simulations) software was employed to perform SPH simulations.

Test case

A test case was designed to replicate extreme flow conditions similar to those experienced in the aortic root. In particular, a tube with diameter enlargement was simulated in SPH (in Figure 53) by using as test fluid PBS (density = 1025 kg/m³, dynamic viscosity = 0.001 Pa s), imposing as boundary conditions a sinusoidal pressure in one of the inputs and zero pressure in the other. The sinusoidal pressure was set with a frequency of 0.5 Hz, a mean value equal to zero and a maximum value needed to get a stroke volume (*SV*) equal to 25 ml. These conditions were selected in order to ensure Reynolds' and Womersley's numbers associated with a laminar flow. Specifically, in pulsatile conditions, the flow regime was identified by comparing the oscillatory Reynolds number (*Re*) with the critical value (*Re_c*), respectively in equation 32 and 33. The critical Reynold number was calculated in a safety condition, considering the lower bound of the transition region [156,157].

$$Re = \frac{v_{peak} * D}{\nu} \quad 32$$

$$Re_c = 250 * Wo \quad 33$$

where v_{peak} (calculated as in equation 34) is the peak mean velocity, ν is the kinematic viscosity (calculated as the ratio between the dynamic viscosity and the density), and Wo is the Womersley number (equation 35).

$$v_{peak} = \frac{SV}{2C * f} \quad 34$$

$$Wo = \frac{D}{2} * \sqrt{\frac{1}{\nu * f}} \quad 35$$

where f is the frequency and C is the cross-section of the tube.

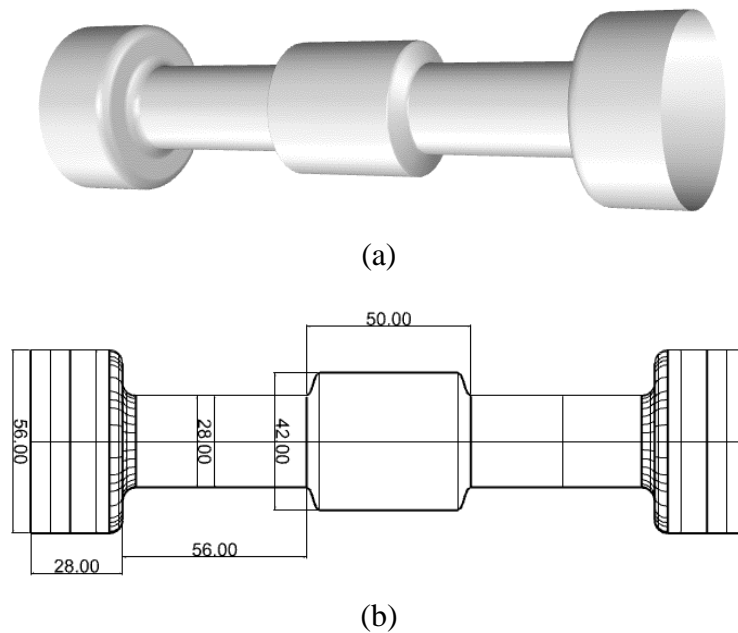


Figure 53 Case of study a) 3D view b) dimensioned drawing in millimetres

Considering a frequency equal to 0.5 Hz, stroke volume SV equal to 25 ml and the smallest diameter ($D = 28$ mm), v_{peak} results equal to 0.0638 m/s, Re equal to 1830 and Re_c equal to 6280, that correspond to laminar condition ($Re < Re_c$).

Synthetic images were obtained by randomly selecting 10% of the particles in a diametrical light sheet of 2 mm, and assigning at each particle a virtual diameter in the range 0.23 – 0.069 mm. The visualised particles were followed from the initial time t to the time $t + \Delta t$ (example of *Synthetic image* is shown in Figure 54). The time interval Δt was chosen equal to 3.5 ms, based on the mean velocity at the selected instant. Fifty pairs of images were obtained from the same couple of instants, by reselecting each time the particles to be shown.

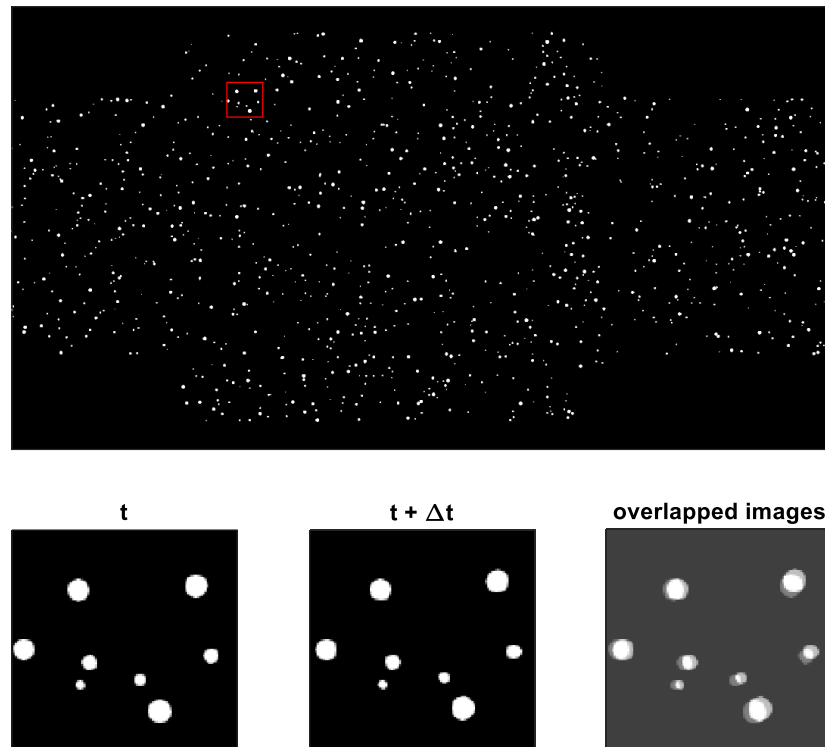


Figure 54 Example of Synthetic image

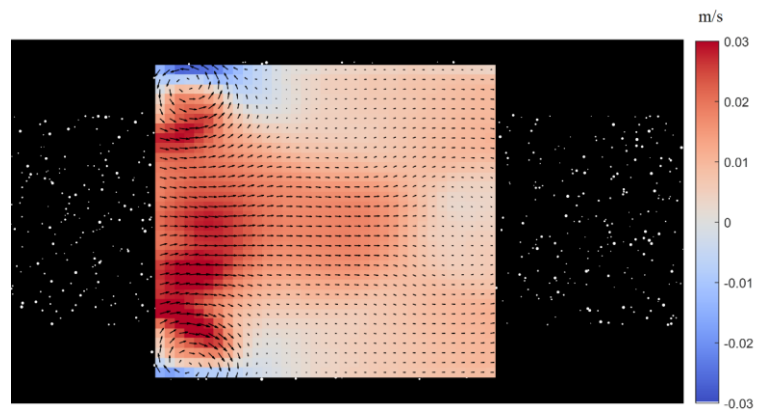
PIV analysis

SPH synthetic images were analysed in PIVlab, open-source Matlab program [66]. PIVlab program allow to apply PIV algorithm to external data images. After the selection of all the pairs of images, a mask was loaded to select a region of interest that includes the region with diameter equal to 42 mm. A recursive multi-pass approach with FFT window deformation was used. As described in section 3.2.1.2, this consists in a first processing pass that computes the vector field of the defined interrogation region. The result of the first processing is used to optimise the second processing pass and the window is deformed to find the best match. At last, a vector validation is applied on the vector field. This function filters out the spurious vectors and fill the removed vectors through interpolation of the neighbourhood vectors.

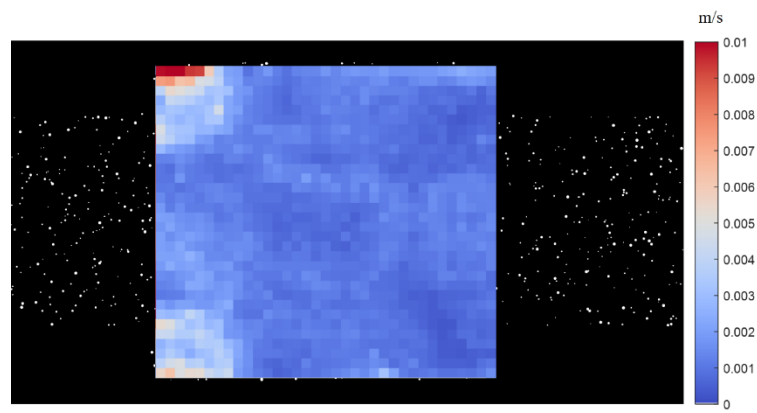
The resulting velocity field were then postprocessed in Matlab, where the mean vectors component and the standard deviation were calculated.

Results

The mean velocity vectors in flow direction and the relative standard deviation obtained through PIV analysis are represented in Figure 55a,b. The mean velocity vector map, compared with the SPH ones (in Figure 56a,b), shows that the velocity pattern is clearly represented, even if a large standard deviation, comparable to the magnitude of the velocity, is observed. This effect is particularly evident in the regions where a high velocity gradient occurs (as in Table 5). As all couples of images are obtained from the same identical instants, just reupdating the random selection of virtual seeding of a purely laminar simulated flow, this standard deviation (see Figure 55b) is just related to the approximation in the PIV processing and cannot be reconducted to the presence of turbulence. This result suggests that PIV velocity vectors are not reliable in regions where high velocity gradients occur, because high standard deviation may be mistaken for turbulence. Typical aortic valve studies detect a high standard deviation in the region between the central jet and the recirculation area in proximity of the wall. This has been commonly associated to the insurgence of turbulent effects [140–144]. This work suggests that the standard deviation may be associated, instead, to an intrinsic error of the PIV technique.







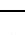
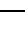



(a)

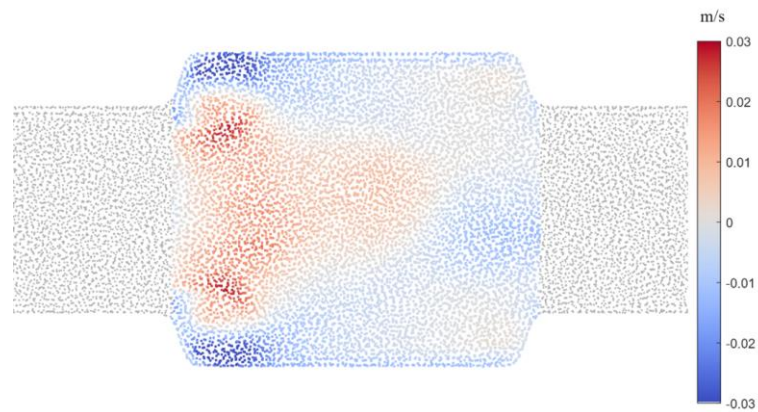


(b)

Figure 55 a) Mean velocity vectors in flow direction, b) standard deviation

Table 5 Mean velocity component and relative standard deviation

	$a_1 = 0.0039 \pm 0.0055$		$a_2 = -0.0063 \pm 0.0019$		$a_3 = 0.0038 \pm 0.0012$
	$c_1 = 0.0221 \pm 0.0014$		$c_2 = 0.0162 \pm 0.0013$		$c_3 = 0.0091 \pm 0.0007$
	$b_1 = 0.0232 \pm 0.0022$		$b_2 = 0.0247 \pm 0.0013$		$b_3 = 0.0177 \pm 0.0007$



(a)



(b)

Figure 56 SPH results: a) magnitude velocity displayed for every particle, b) velocity vector field

Conclusion

In conclusion, fifty pairs of SPH *Synthetic Images* obtained from the same set of instants (t and $t+\Delta t$) were analysed with a PIV algorithm. Even if the mean velocity vectors are comparable with SPH results, a high standard deviation is detected. The latter has the same magnitude of the velocity where a high velocity gradient occur, but cannot be related to turbulent flow, because a laminar flow was modelled in SPH.

The generation of SPH *Synthetic Images* on aortic root geometry and valve has resulted a practical and versatile method to assess the reliability of PIV results in complex flow patterns. Due to its Lagrangian nature, SPH is particularly suitable for

this application, because the virtual seeds are not positioned from the calculated streamlines but can correspond to the same particles on which the method calculates velocity and pressure field. Moreover, this kind of PIV analysis on SPH *Synthetic Images* may be also a powerful instrument for PIV experimental planning and for the setting of optimum parameters in terms of required time intervals suitable for the different regions, number of images, particles size and concentration, and laser sheet thickness. This could strongly expedite the testing phase, especially in complex cardiovascular cases, where a large number of experimental setups typically need to be analysed to tune the PIV parameters.

4.2.3.2 Refractive Index Matching

Due to its optical nature, the PIV technique is particularly sensible to refractive index (RI) variation [158]. Refractive index is an intrinsic property of materials, defined as the ratio between the light velocity in free space and the light velocity in the specific material. When light cross through two materials with different RI, the not orthogonal light rays are refracted (see Figure 57) of an angle θ_2 that depend on the incidence angle θ_1 and the RIs ratio, in equation 36 [159].

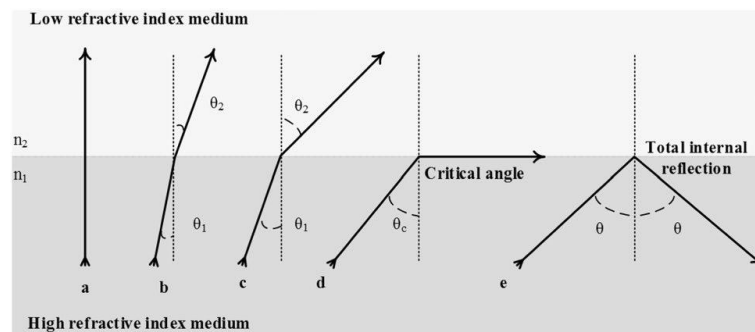


Figure 57 Refraction of a light rays that cross an interface between materials with different RI [159]

$$\frac{\sin(\theta_1)}{\sin(\theta_2)} = \frac{n_2}{n_1}$$

In PIV experiments, the laser sheet, passed the lens, has to cross through gas-solid and solid-liquid interfaces before reaching the investigated flow, thus experiencing potential changes of angle in its path, due to refraction. This makes impossible maintaining thickness and direction the sheet, especially when complex anatomical morphologies such as the Valsalva sinuses are modelled. Similarly, the light from the enlightened seeds travels through several interfaces before reaching the acquisition camera, experiencing potential distortions that produces spurious particle positions and velocities, not negligible in complex geometry [160]. Moreover, in cardiovascular applications, blood viscosity and density should be matched using suitable test fluid solutions, in order to reproduce the correct blood dynamic behaviour [5,6,161].

In order to overcome this issue, the refractive index of the different materials between which curved interfaces are present must be matched [158]. In the study of aortic flow (in section 4.2.2), PIV was applied on a Pulse Duplicator system (as discussed in section 3.3.1). To study the aortic flow, an aortic phantom made of silicone was positioned just above the aortic valve. Therefore, in this case there are three interfaces: air-acrylic, acrylic-silicone, silicone-test fluid solution.

In particular, the acrylic walls of the aortic chamber are flat, and perpendicular to the camera and the laser (see Figure 48). In the aortic chamber, a silicone mock root was placed instead of the glass aortic root (in Figure 13), that has an external shape with flat surfaces in correspondence of the camera and the laser sheet and has a complex internal shape, that models an idealised aortic root with its Valsalva sinuses,

in contact with the test fluid solution. The working fluid for valve performance study is usually PBS, as described in the standard ISO5840 [78], which has a RI substantially different from that of common optically transparent silicones. Hence, to minimise image distortion the RI should be matched between the silicone and the fluid solution.

In this work, a new blood equivalent solution, composed of PBS and propylene glycol (PG) is proposed. An ideal blood equivalent have same blood viscosity and density as human blood, and match its RI with that of the anatomical solid phantom, usually made from silicone materials. Two optically transparent silicone materials were investigated: Sylgard-184 and FER-7061. Moreover, the potential influence of the proposed blood equivalent solution upon the mechanical properties of soft tissues, normally used in bioprosthetic heart valves, were assessed. In fact, previous works suggested that glycerol solutions commonly adopted as blood equivalent can alter tissue properties, potentially altering the valve leaflets dynamics and leading to incorrect analysis [162–164]. In order to make PG solutions attractive alternative, their potential effect on the mechanical properties of biological tissues needs to be verified.

Materials

Human blood is a non-Newtonian liquid composed of cellular elements suspended in plasma. In large vessels (> 0.5 mm) and high shear rates (> 100 s⁻¹), which are typical of most cardiovascular applications, blood can be assumed Newtonian, with dynamic viscosity in the range between 3.5 and 5.5 cP [165–168].

The proposed blood equivalent consists of a solution of PBS and PG (properties reported in Table 6).

Table 6 Material Properties at room temperature

Material	RI	Viscosity [cP]	Density [kg/l]	Phase
Air	1.0003	-	-	Gas
Acrylic [158]	1.491	-	-	Solid
Sylgard-184 (Silicone)	1.4118	-	-	Solid
FER-7061(Silicone)	1.38	-	-	Solid
PBS solution [169]	1.336	1.02	1.030	Liquid
Propylene Glycol (PG)	1.431 ÷ 1.433	46	1.035 ÷ 1.040	Liquid
Human blood [165,170] *	-	3.5 - 5.5	1.060	Liquid

* Whole blood at body temperature

PBS is the most common test fluid for valve assessment for its biocompatibility with the biological prosthesis and its ionic content suitable for velocity measurements by means of electromagnetic Flowmeters (such a device is used in the Pulse Duplicator system used for tests presented in this thesis). PBS is composed of distilled water and 0.9% of salt (0.138 M of NaCl and 0.0027 M of KCl), and has a RI equal to 1.336, a low viscosity (1.02 cP) and a density equal to 1.030 kg/l. PG is a transparent, colourless, odourless and tasteless viscous synthetic liquid which is totally soluble in water [171] with: density equal to 1.035 ÷ 1.040 kg/l, high viscosity (46 cP) and 1.4324 of RI.

The matched silicone were: FER-7061, a new low RI silicone produced by Shin-Etsu for high requirements optical applications, and Sylgard-184 silicone [159] produced by Dow Corning. Their RI is intermediate between PBS and PG, equal to 1.38 and 1.4118 respectively.

RI matching experimental setup

In order to match the RI of silicone and PG solution, a basic test was devised, as shown in Figure 58. The test system comprises: an acrylic box (50x50x50 mm) with

flat surfaces, a silicone model composed by a cylinder (of diameter 20 mm) with a half-sphere on top (described in Appendix C), a grid with square side of 2 mm and the blood equivalent solution. The latter, initially composed of 100% of PG, is progressively diluted with incremental percentage of PBS, acquiring pictures until an optimum match is found. The volume of PBS was added with a 5 ml pipette and mixed each time.

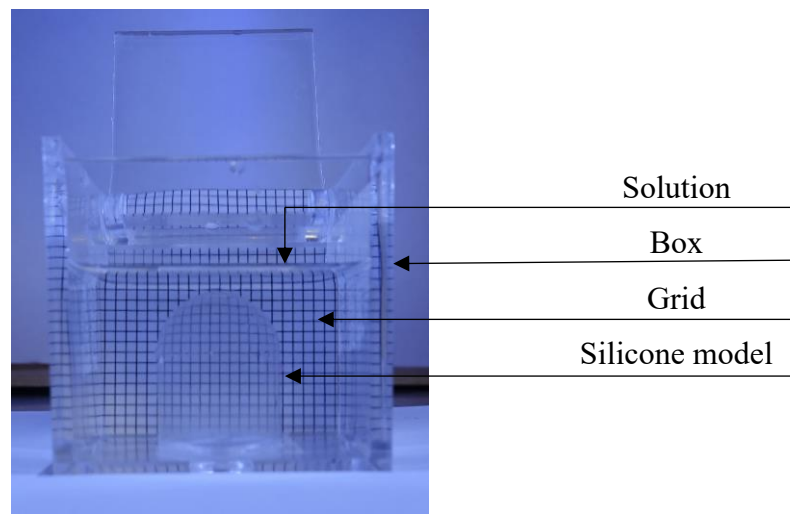


Figure 58 Mismatching experimental set-up

The pictures acquired with a camera (Sony RX0 II) were processed in Matlab by means of DIC technique. In particular, each image was divided in three regions, represented in Figure 59 as enclosed into a yellow, red and blue rectangular contour. The correlation was performed by comparing each reference region (in yellow) with the red and blue ones by using a basic Matlab image correlation function “corr2”. The latter returns a correlation coefficient (R) between 0 and 1, dependent on the matching obtained by applying the following equation:

$$R = \frac{\sum_m \sum_n (A_{mn} - \bar{A})(B_{mn} - \bar{B})}{\sqrt{(\sum_m \sum_n (A_{mn} - \bar{A})^2)(\sum_m \sum_n (B_{mn} - \bar{B})^2)}} \quad 37$$

where A and B are the compared images, m and n are image row and column, and \bar{A} and \bar{B} are the mean value of the whole image A and B .

A high value of R is associated with a better image matching. The correlation coefficient values obtained in the red and blue regions were mediated to obtain the best match.

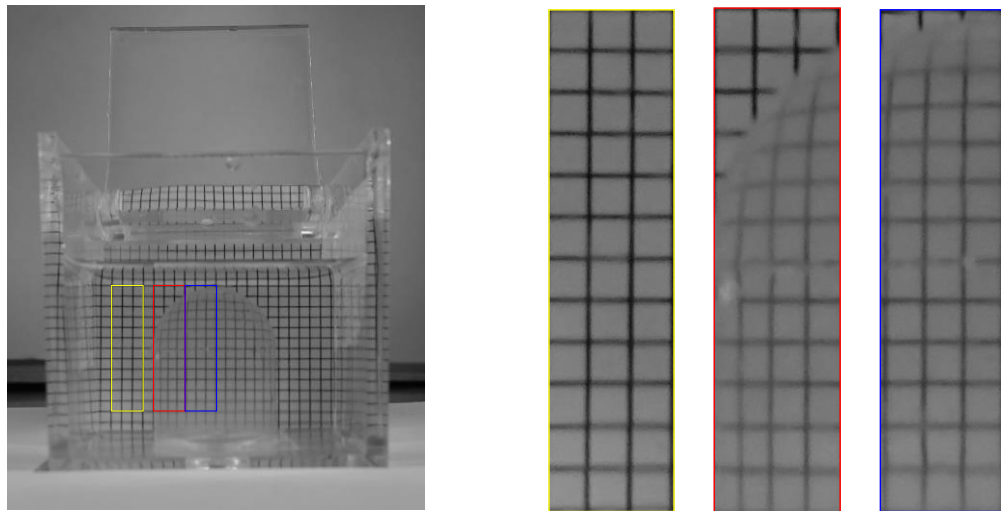


Figure 59 Regions of correlation

Moreover, to match the blood properties, the dynamic viscosity of each solution was monitored with a viscosimeter (Viscolite 700) and density was calculated by weighting the volume of the solution in a graduated beaker in a scale (Sartorius resolution 0.1 g maximum weight 8200 g).

Uniaxial tests

An optimum blood equivalent must demonstrate to be able to operate in contact with test devices without altering their behaviour. In the case of cardiovascular devices, the most critical materials are soft tissues, such as xenograft glutaraldehyde fixed valve

leaflets and pericardium, which have demonstrated some sensibility to commonly employed blood equivalent solutions based on glycerol [162–164]. These tissues are used in a critical applications, such as the leaflets of bioprosthetic valves, so that any change in their mechanical response may introduced artefacts in the operating dynamics leading to incorrect results. Although PG is widely used in the chemical, food, and pharmaceutical industries, and recognized as safe for food use [171], its effect on mechanical properties of biological tissue is unknown. Hence, in order to ascertain the suitability of the proposed blood equivalent for general cardiovascular applications, a series of uniaxial tests was performed on three dog-bone pericardium specimens (CardioCel) in a uniaxial tensile machine Instron 5943 equipped with a 1 kN load cell, pneumatic grips and a thermostatic BioPuls bath. The specimens had gauge length equal to 12 mm, width equal to 2 mm and thickness respectively equal to 0.190 mm, 0.276 mm and 0.217 mm. They were cut trying to align their test axis with the observed collagen fibre direction, using a standardised die-cutter following the standard ISO 37 specimen type 4 [114] (as in Figure 60a). Specimens were loaded in the tensile test machine via the use of a PLA specimen support (sketch in Figure 60b). This support was helpful to load the specimen avoiding preload due to its own weight, it was cut after the specimen was clamped and immersed in the test fluid (cut lines in Figure 60c). Specimens were kept clamped during all test repetitions.

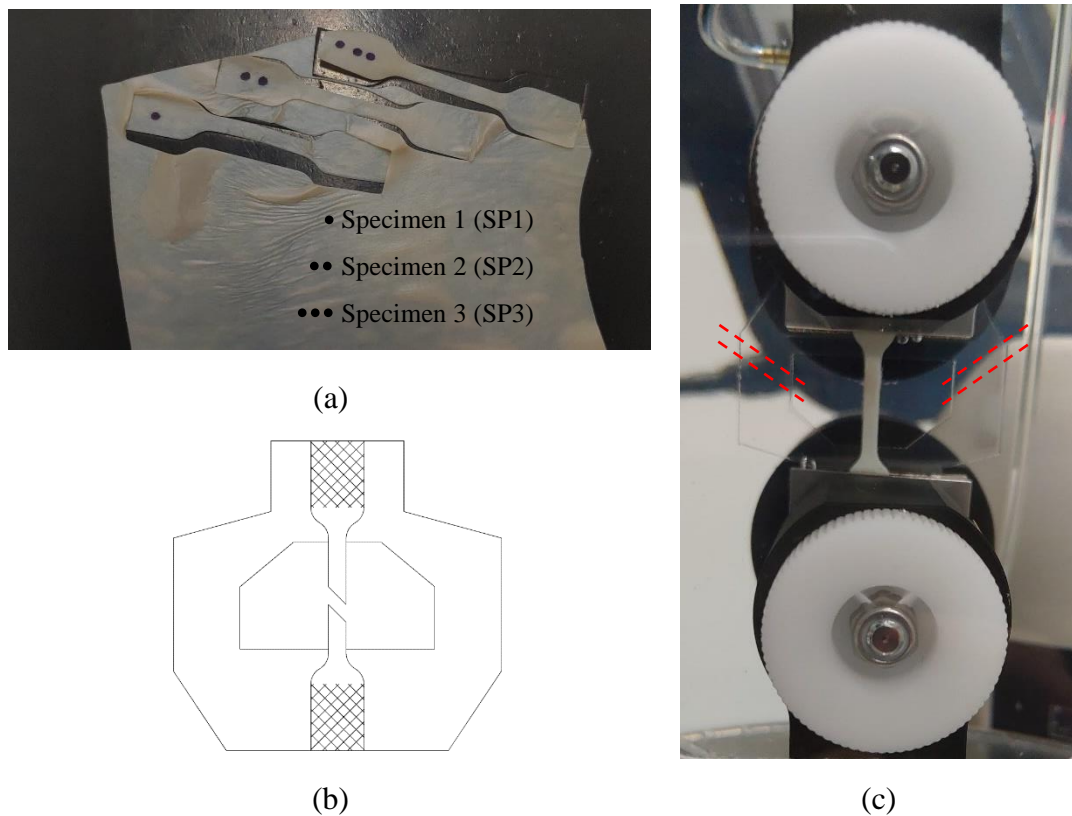


Figure 60 a) Dog-bone pericardium specimens, b) specimen support, c) gripped and immersed specimen

In order to identify the effect of the blood equivalent solution on pericardium mechanical characteristics, specimens SP2 and SP3 were tested at room temperature ($\sim 25\text{ }^{\circ}\text{C}$) in displacement control (1 rpm) reaching a stress of 4.5-5 MPa (maximum stress estimated in heart valve aortic leaflets during their operating cycle [9]) immersed in PBS and then in PG solution, following the schedule:

a) in PBS (in Figure 61)

- Determination of the test deformation (ϵ_{test}) that gives a stress of 4.5-5 MPa with the specimen immersed in PBS;
- 100 cycles of preconditioning in solution, 10 cycles of data acquisition in solution, 1 cycle out of solution and 10 cycles of data acquisition in solution;

- The specimen was left in the PBS solution for 24 hours;
- 100 cycles of preconditioning in solution, 10 cycles of data acquisition in solution, 1 cycle out of solution and 10 cycles of data acquisition in solution;
- The sample was left in the PBS solution for 24 hours;

b) in PG solution (in Figure 62)

- 100 cycles of preconditioning in solution, 10 cycles of data acquisition in solution, 1 cycle out of solution and 10 cycles of data acquisition in solution;
- The sample was left in PG solution for 6 hours;
- 100 cycles of preconditioning in solution, 10 cycles of data acquisition in solution, 1 cycle out of solution and 10 cycles of data acquisition in solution;
- The sample was left in PG solution for 18 hours;
- 100 cycles of preconditioning in solution, 10 cycles of data acquisition in solution, 1 cycle out of solution and 10 cycles of data acquisition in solution;
- The sample was left in PG solution for 6 hours;
- 100 cycles of preconditioning in solution, 10 cycles of data acquisition in solution, 1 cycle out of solution and 10 cycles of data acquisition in solution.

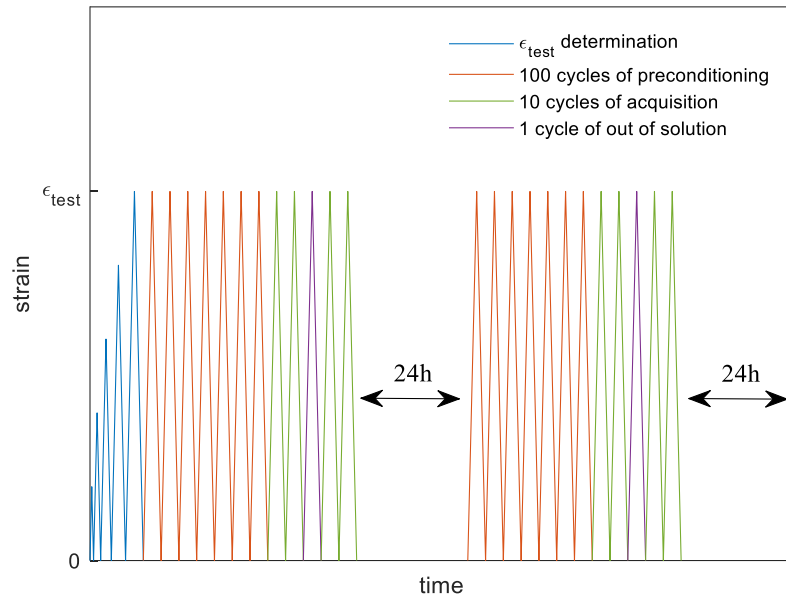


Figure 61 Qualitative schedule plot of test in PBS

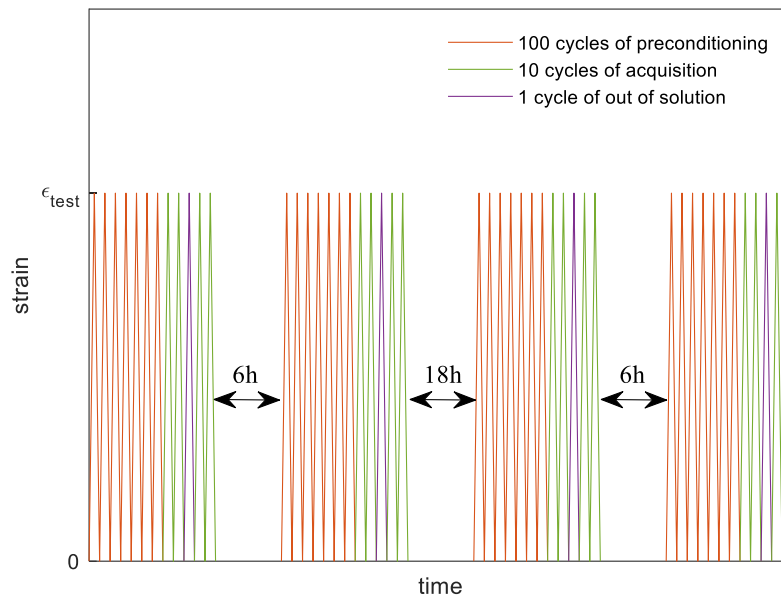


Figure 62 Qualitative schedule plot of test in PG solution

Practically, the specimens, after the determination of the test deformation, were tested by following the protocol repetition twice in PBS in order to evaluate the different behaviour in 24 hours. Then it was tested in PG solution four times to assess the variations in 48 hours.

The specimen SP1 (identified from the single dot in Figure 60 a) was sacrificed to optimise the schedule protocol. The remaining samples (SP2 and SP3) were compared. In particular, strains were calculated from the crosshead displacement and stresses as force measured by the load-cell, divided by initial cross-sectional area, for all the acquisition cycles.

For each repetition, two sets of 10 cycles (C1, C2) were performed. Results from set C1 were mediated and corrected to be compared between the PBS and PG solution tests. Results from set C2 were mediated and compared with C1, to check if a cycle out of solution affects the mechanical characteristics. Tests out of solution (Co) were performed to evaluate the variation of fluid force on the grip during its movement. During the test, the upper grid partially emerges from the test fluid since the different density between PBS and PG (reported in Table 6) can affect the results. So, the variation of fluid force was evaluated and added to the C1 cycles in order to make PBS and PG tests comparable. In particular, the fluid force was calculated as in equation:

$$F_{fluid} = (F_{max} - F_{min})_{Co} + (\bar{F}_{max} - \bar{F}_{min})_{C1} \quad 38$$

where F_{max} and F_{min} are the maximum and minimum force of the cycle out of solution (Co) while \bar{F}_{max} and \bar{F}_{min} represent the mean cycle of data acquisition (C1). F_{fluid} was transformed in stress dividing by initial cross-sectional area and subsequently was fitted between zero and ε_{test} . The resulting line was thus subtracted from the C1 curve obtaining the adjusted curve (C1a).

Results

Figure 63 a,b shows the RI mismatch of the raw components of the proposed solution (PBS and PG) with Sylgard-184 silicone. As the RI of Sylgard-184 is

intermediate between PBS and PG (see Table 6), an opposite optical dispersion can be observed. In fact, PBS tends to enlarge the Grid (in Figure 63 a), PG makes grid squares optically smaller (Figure 63 b).

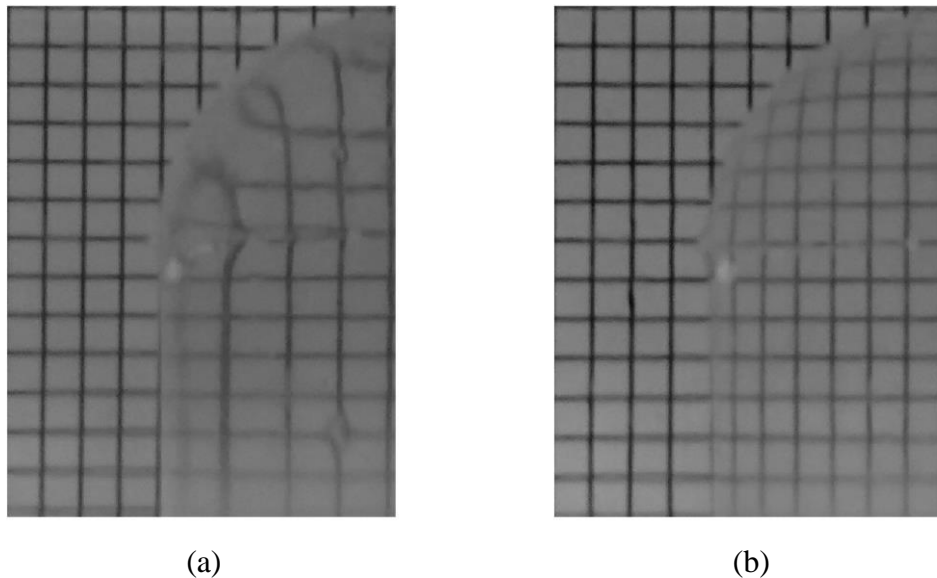
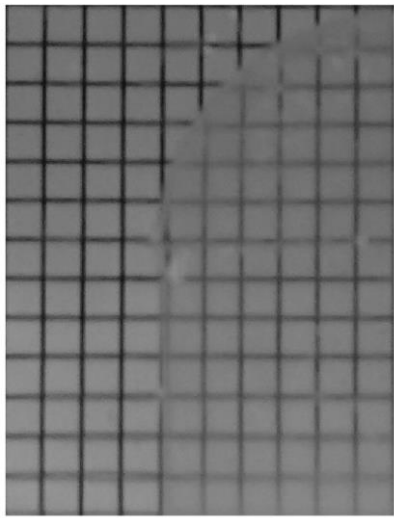


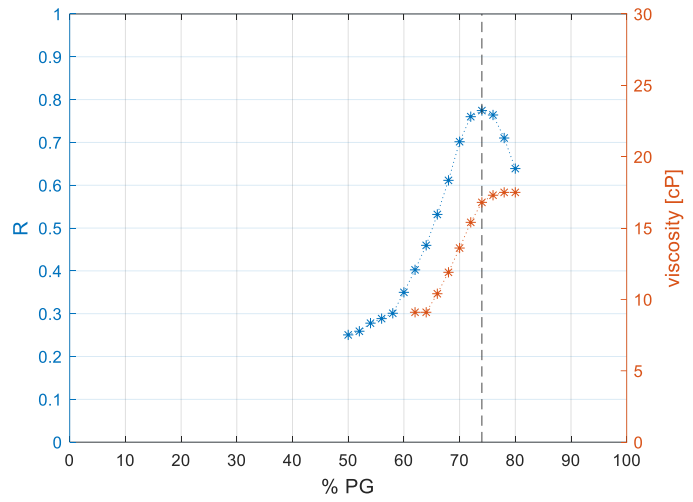
Figure 63 Picture composed of: a) 100% PBS (or % PG); b) 100% PG

By diluting PG with PBS, the best match between PG solution and Sylgard-184 silicone is reached at 74% that corresponds to a viscosity equal to 16.8 cP (in Figure 64). This result suggests that at room temperature (25 °C) a good refractive index must tolerate errors in the viscosity.

The best match between the PG solution and FER-7061 is reached at 52% (Figure 65) that corresponds to a dynamic viscosity equal to 6.2 cP at room temperature (25 °C). Furthermore, by considering a temperature about 37 ± 1 °C the RI match remains unchanged, while the viscosity becomes equal to 3.8 cP (value in the range of blood viscosity in normal hemodynamic conditions) and a density equal to 1.034 kg/l.

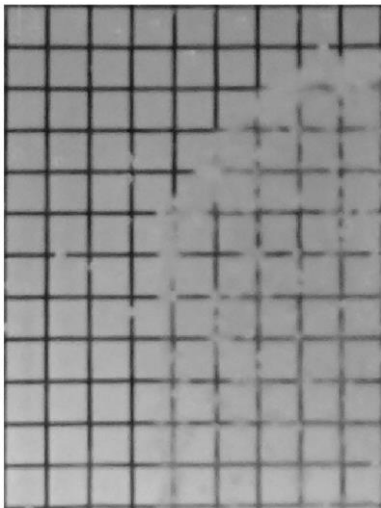


(a)

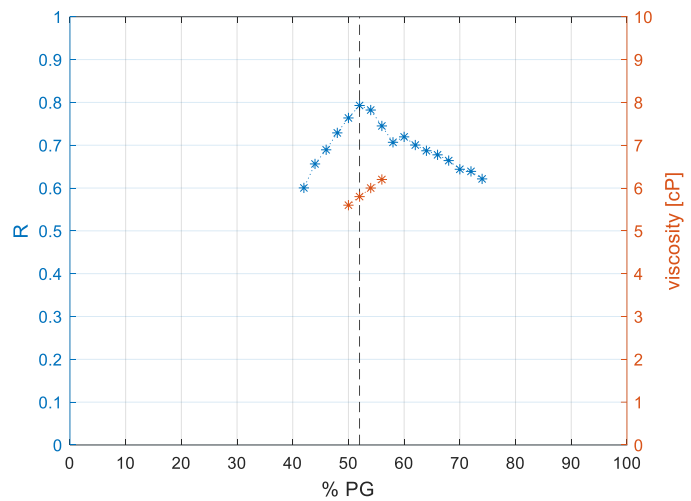


(b)

Figure 64 a) Best match between PG solution and Sylgard-184, b) diagram of correlation coefficient R and viscosity respect to PG concentration



(a)



(b)

Figure 65 a) Best match between PG solution and FER-7061, b) diagram of correlation coefficient R and viscosity respect to PG concentration

Therefore, in the tests to evaluate the potential influence of blood equivalent upon mechanical pericardium properties, the thermostatic bath was filled with the solution representing the highest percentage of PG (74% PG solution corresponding to the best blood equivalent for Sylgard-184 silicone).

In Figure 66 it is reported the stress-strain plot of the first repetition in PBS, performed on sample SP2. The curves present the typical J-shape expected for soft tissues [172,173]. As shown in Figure 66 curve C1 and C2 (the mean curve of the first and second set of 10 cycles) are almost overlapped. So, because the same result is observed in all the other cases, just the first set of cycles will be discussed.

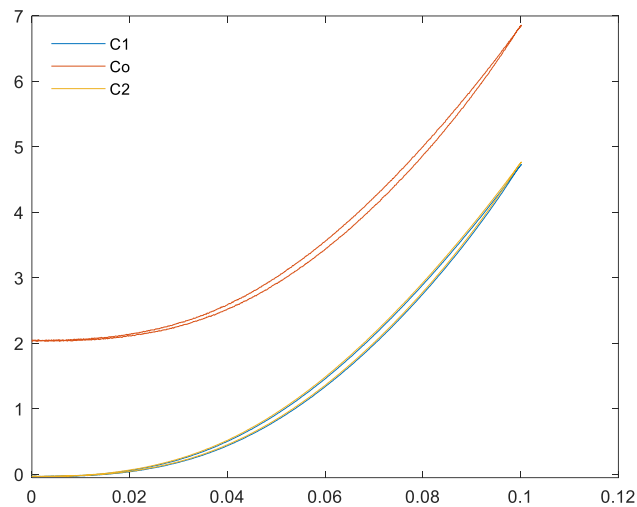


Figure 66 Stress-strain plot of the first in PBS repetition performed on the first sample

The curve C1 of each repetition was adjusted, as described in equation 38, obtaining C1a curve. In Figure 67 C1a curves of the specimens for all the repetitions with PBS and PG are reported. As it can be observed, the curves shape does not change with the test fluid, although some differences in the maximum value of reached stress are observed.

In Figure 68 the maximum stresses and its standard deviation are represented. In the case of specimen SP2 (in Figure 68a), the PBS stress in 24 hours remains almost unchanged, drops down when the PG solution is inserted and then starts to increase again in the following repetition. Specimen SP3 (in Figure 68a), on the contrary,

exhibits similar changes between PBS stress at 0 hours and 24 hours, and between all the PG repetitions.

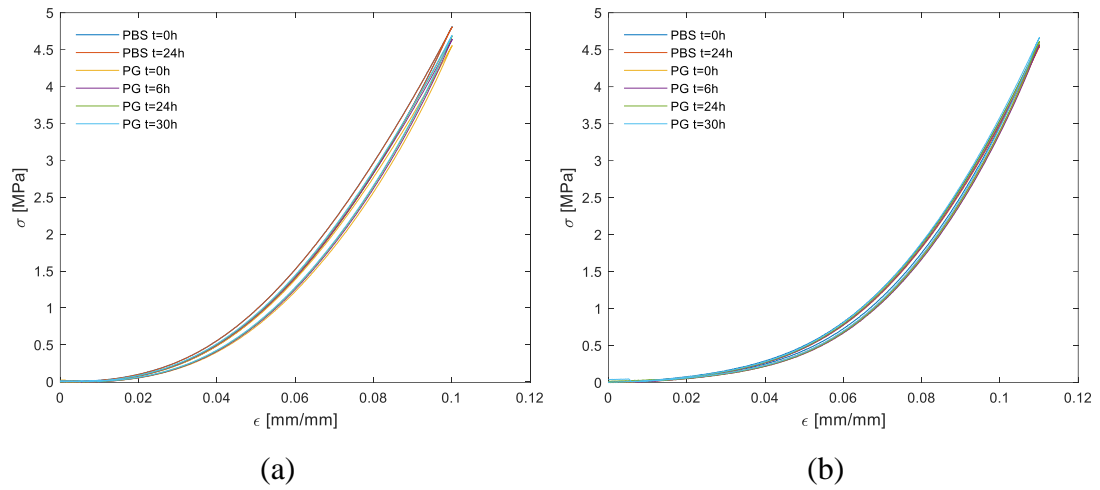


Figure 67 C1a curves for all the repetition with PBS and PG of specimen a) SP2 b) SP3

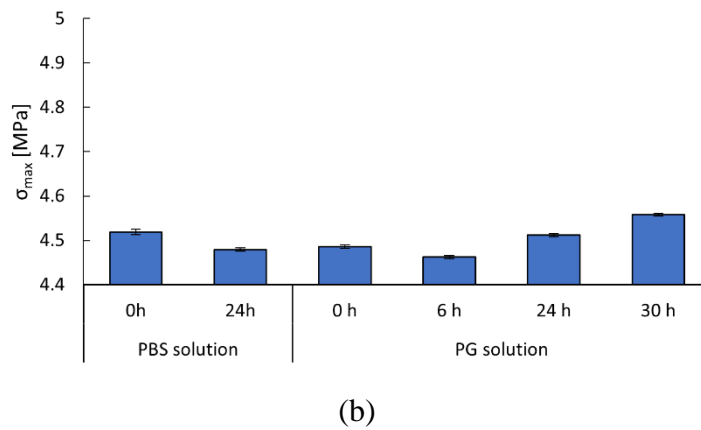
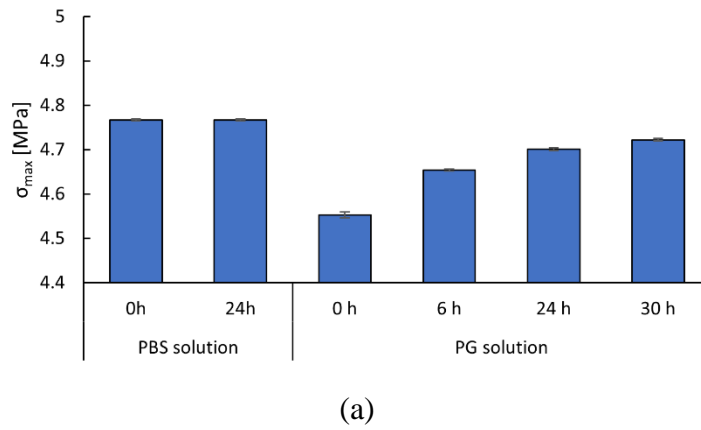


Figure 68 Maximum stress of all the repetition for specimen a) SP2 and b) SP3

In summary, specimens show different behaviour with a maximum stress variation of 4%, that results smaller than the difference between the two specimens. These results confirm that the changes introduced by the PG solution are equivalent to those produced by standard PBS.

At the end of all the repetitions, specimen SP3 (just removed from PG solution) was visually compared to specimen SP1, that was tested and kept in PBS. Specimen SP3 appeared more transparent (in Figure 69a) but regained its normal opacity when kept for few days in PBS (in Figure 69b).

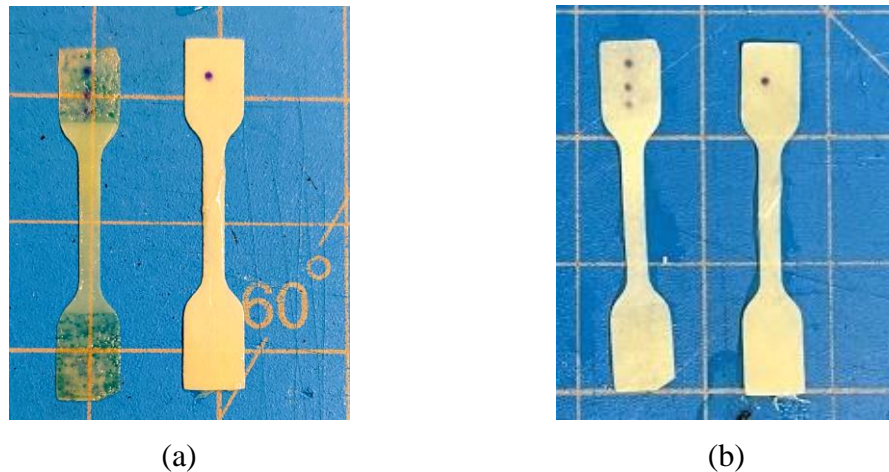


Figure 69 Comparison between: a) SP3 kept in PG solution and SP1 kept in PBS solution b) SP3 kept after test few days in PBS solution and SP1 kept in PBS solution

Conclusion

In conclusion, the solution based on 52 % PG in PBS, at a body temperature of 37 °C, provides an optimum model of human blood in terms of density and viscosity, also matching the RI of FER-7061 silicone. Moreover, it does not introduce any observable alteration in the mechanical response of the soft tissues commonly employed in cardiovascular prostheses.

5. Conclusion

Image correlation techniques were used for structural and fluid-dynamics analyses in biomechanics and cardiovascular application, in order to improve the understanding of a number of phenomena and enhance the characterisation and assessment of biomaterials, biofluids and prosthetic devices. In particular, DIC technique was applied to the mechanical characterisation of complex biomaterials of common use in prosthetic devices, such as biocompatible superelastic shape memory alloys and soft materials.

PIV was employed for the analysis of complex fluid-dynamic systems, such as Aortic root hydrodynamic assessment, expanding its application to the measurement of the EOA.

Finally, digital image correlation was also applied to the design synthesis of a new blood equivalent solution, more suitable for *in vitro* PIV testing.

These critical applications of digital image correlation techniques in the cardiovascular area were analysed, with the aim to verify their current limitations and identify, where possible, original solutions to overcome them and expand their reliability and application field.

In particular, thanks to the application of DIC, substantial errors in the standard methods for Nitinol mechanical characterisation was found as part of the presented study. Still, the use of DIC, in combination with thermography, has allowed to devise a new testing methodology that minimises these errors and detect a mechanical behaviour which is substantially closer to the theoretical one, more directly employable to a derive parameters suitable for their use in computational simulations. This can have major impact in the optimisation of critical cardiovascular structures such as angioplasty stents, stent grafts, endovascular occluders and transcatheter heart valves. Furthermore, DIC application combined with TSA have proved their potentiality to provide a powerful tool to study the local and global stress state of Nitinol components. Future work should consider the application of mono frequency loading (in load control) to better identify the nature of the second harmonic response and verify the finding of this works about thermomechanical heat source.

Similarly, DIC application to soft materials has allowed the identification of errors that can exceed 50 % in the material rigidity determined by means of biaxial characterisation methods. Again, by integrating DIC and finite element analyses, a new setup arrangement of easy implementation was devised as part of this thesis, that contains the error below 20% and indicates a route towards further improvements by optimising the specimen design. Further studies may focus on the application of the

identified setup arrangement to biological soft tissue, in order to identify the effective influence of the outer frame in the case of anisotropic and viscoelastic behaviour.

Fluid-dynamic applications were explored by means of PIV, to better understand complex fluid-dynamic mechanism of aortic valve function and support its assessment. For this purpose, a fluid-dynamic analysis of the healthy native valve was conducted in order to understand the role of the principal aortic root anatomic components. Then PIV technique was applied to establish a new potential experimental approach allowing the direct measurement of the EOA, an aortic valve performance parameter conventionally estimated through approximate equations. This PIV analysis enabled to identify significant sources of error such as experimental feasibility and image distortion due to refractive index mismatching. Those errors were studied and digital image correlation was used to synthesise a new optically transparent test solution that exhibits similar dynamic viscosity and density as healthy human blood. The fluid provides optimum refractive index matching with a recently developed silicone, whose potential use for the manufacturing of anatomical phantoms was verified, implementing a protocol. Moreover, contrary to the test fluids currently used to mimic blood properties, which are glycerol based, it was demonstrated not to alter the mechanical response of biological soft tissues commonly adopted in cardiovascular prostheses.

Another important area of research was the analysis of potential errors affecting PIV analysis in cardiovascular flows, such as the flow at the exit of the aortic valve. As PIV is the accepted experimental gold standard, quantifying its limits is particularly arduous, due to the lack of more accurate approaches. Hence, an approach that generate

virtual PIV experiments from computational simulations based on Lagrangian SPH was attempted. The study replicated fluid dynamic conditions with similar features as physiological flows in the aorta, identifying a source of potential errors in the regions surrounding the outcoming jet, where high velocity gradients are present. In particular, despite most PIV studies in the literature indicate the presence of regions at the exit of the aortic valve associated with turbulent phenomena, the presented study suggest that this may be a misinterpretation due to the intrinsic errors in the experimental technique. This reveals an essential limitation that needs to be taken into consideration to assess the PIV suitability to investigate the blood damage potential of prosthetic valves, as suggested by latest regulations.

In conclusion, although Image Correlation techniques offer a valid support to design and assess cardiovascular devices, they are still far from their full potential. The studies presented as part of this thesis contribute to this purpose, expanding the reliability and their field of application (often in combination with other experimental and numerical approaches), with the aim to support the development and assessment of safer and more effective cardiovascular solutions.

6. Appendix

Appendix A. Selection of the ROIs _{σ} , dimension based on the maximum estimated error on the stress determination.

In order to maintain geometrical congruence, the interface between the region where the martensitic transformation has occurred and the portion of the specimen which is in the austenitic phase needs to take a specific angle with respect to the axis. Therefore, the cross sections hosting the front of transformation are partitioned into multiple regions with different mechanical properties. This results in departures of the neutral axis from the cross-sectional centre of gravity, contributing to locally introduce a bending moment.

Based on the common theory of composite beams, for each cross section, the eccentricity of the neutral axis will depend on the cross-section geometry, on the distribution of the regions with different Young's modulus and, in the case where only two Young's moduli are present, on their ratio n . In particular, the maximum eccentricity of the neutral axis will be reached when the transformation occurs with a single front.

In fact, if the front of the martensitic phase reaches a distance m from the origin of a reference system positioned at the left end of the specimen cross section, with the x -axis aligned with the specimen width w (see Figure 70.a), the position of the neutral axis can be determined as:

$$x_{NA} = \frac{A_M x_M + n A_A x_A}{A_M + n A_A} = \frac{1}{2} \cdot \frac{m^2 + n(w^2 - m^2)}{m + n(w - m)} \quad 39$$

and the eccentricity of the neural axis is:

$$e_{NA} = x_{NA} - \frac{w}{2} = \frac{1}{2} \cdot \frac{m^2(1-n) - mw(1-n)}{nw + m(1-n)}. \quad 40$$

This eccentricity will be maximum when:

$$\frac{de_{NA}}{dm} = (n-1) \frac{(n-1)m^2 - 2nwm + nw^2}{[(n-1)m - nw]^2} = 0; \quad 41$$

which has acceptable solution:

$$m = w \frac{\sqrt{n}}{1 + \sqrt{n}}. \quad 42$$

Substituting into the expression of the eccentricity:

$$e_{NA \max} = \frac{w}{2} \cdot \frac{\sqrt{n} - 1}{\sqrt{n} + 1}. \quad 43$$

In this case, the position of the neutral axis in the reference system, x_e and that of the front of transformation, m , are coincident. In fact:

$$x_e = \frac{w}{2} + e_{NA \max} = \frac{w}{2} \left(1 + \frac{\sqrt{n} - 1}{\sqrt{n} + 1} \right) = w \frac{\sqrt{n}}{1 + \sqrt{n}} = m. \quad 44$$

Hence, the stress associated with the resulting bending moment M (excluding the stress produced by the normal load) will have the distribution represented in Figure 70.b, with:

$$\sigma_{M \max} = \frac{m}{n(w-m)} \sigma_{A \max} \quad 45$$

The mean stress calculated over a centred specimen length of dimension $p \cdot w$, is given by:

$$\bar{\sigma}_x = \frac{\frac{1}{2} \left(m - \frac{1-p}{2} w \right)^2 \frac{\sigma_{M \max}}{m} - \frac{1}{2} \left(w - m - \frac{1-p}{2} w \right)^2 \frac{\sigma_{A \max}}{w-m}}{p \cdot w}$$

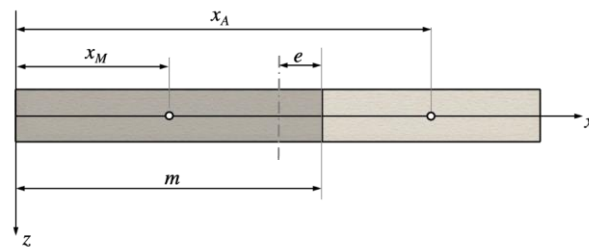
46

$$= \left[\left(\frac{\sqrt{n}-1}{1+\sqrt{n}} + p \right)^2 - n \left(\frac{1-\sqrt{n}}{1+\sqrt{n}} + p \right)^2 \right] \frac{(1+\sqrt{n})}{8np} \sigma_{A \max}$$

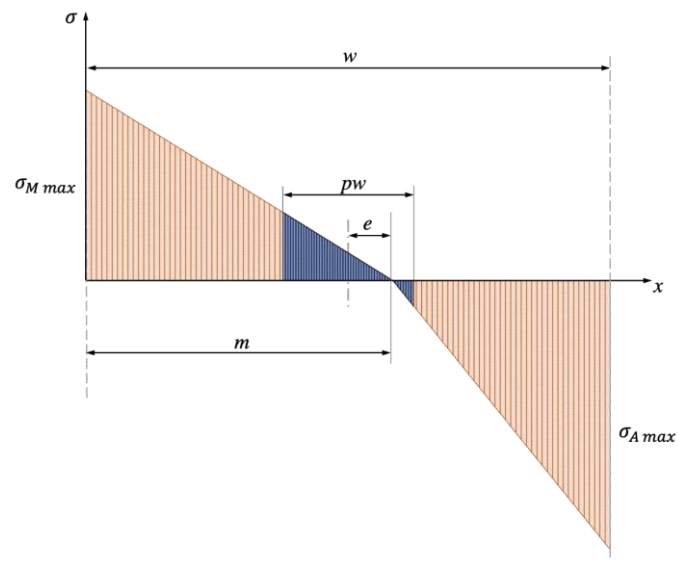
Assuming a reasonably conservative value of $n = E_A/E_M = 2$, analysing a region equal to 25 % of the specimen width ($p = 0.25$):

$$\bar{\sigma}_x = 0.10 \sigma_{A \max}$$

47



(a)



(b)

Figure 70 a) Specimen cross-section; b) Bending moment diagram

Appendix B. Angles between the regions at the interface between the two phases

Due to the large transformation strain ε_L and transformation Poisson's ratio ν_T , the martensitic region of the specimen is characterised by significant dimensional changes compared to the untransformed austenitic region. Hence, in order to preserve continuity, the interface between two phases and the two regions at the interface will need to take specific angles that, in first approximation, can be determined from basic geometric considerations.

Assuming, for simplicity, that the transformation propagates with a single front (see Figure 23.a), the dimensions of the martensitic triangular region covering the specimen length interested by front will be:

$$h_M = h_A(1 + \varepsilon_L); \quad 48$$

and

$$w_M = w_A(1 - \nu_T \varepsilon_L). \quad 49$$

Indicating with α_A and α_M the angles between the transformation front line and the transversal section of the austenitic and martensitic regions, respectively, it will also be:

$$h_A = w_A \tan \alpha_A \quad 50$$

The Pythagorean theorem can provide the following additional relation, which allows to solve the system:

$$h_A^2 + w_A^2 = h_M^2 + w_M^2 \quad 51$$

Combining equations 48 with 49, α_A can be determined as:

$$\alpha_A = \arctan \sqrt{\frac{2v_T - v_T^2 \varepsilon_L}{2 + \varepsilon_L}} \quad 52$$

α_M can be determined from the equations below, thanks to the trigonometric relationship:

$$\frac{h_A}{\sin \alpha_A} = \frac{h_M}{\sin \alpha_M}. \quad 53$$

In fact, combining equations 53 with 50, α_M can be obtained as:

$$\alpha_M = \arcsin[(1 + \varepsilon_L) \sin \alpha_A]. \quad 54$$

Appendix C. Manufacturing

Human aortic root has unique shape and size. For the test case of in section 4.2.2 an idealised model based on healthy human anatomy was identified [123,174], in Figure 71. The model is based on the description of the aortic root by *Swanson & Clark* [175] with the leaflets attachment defined by *Thubrikar et al.* [176] and the profile of the sinuses of Valsalva defined by *Reul et al.* [177].

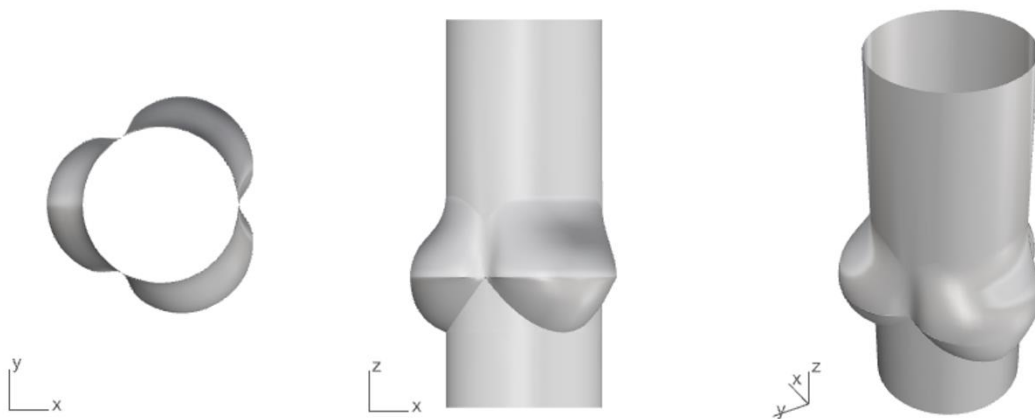


Figure 71 Aortic root 3D model

Before manufacturing the Silicone Aortic root some prototyping test was performed by preparing the silicone model for the refractive index experiment (of section 4.2.3.2) in Sylgard-184 and FER-7061.

Both materials are bicomponent optically transparent silicones that present different characteristics and curing cycles. In particular, Sylgard-184 cures at room temperature in a couple of day (less if heated), and FER-7061 cures at 150 °C in 2 hours.

Sylgard.184 model (in Figure 64a) was made by:

- Designing in Rhinoceros a model (composed by a cylinder with an half sphere on top) and the relative mould (in Figure 72);
- 3D printing the mould with a rigid resin by using a Form3 printer (Formlab);
- Mixing the two silicone parts with the suggested mixing ratio;
- Removing the bubbles in a vacuum chamber;
- Pouring the silicone in the mould;
- Curing the silicone in the oven at 60 °C for a day;
- Tearing the mould to release the casted model.



Figure 72 Refractive index 3D model of the mould

In the case of FER-7061, because of the higher curing temperature, the high expansion coefficient and high adhesion strength, the 3D model was printed with a flexible resin, needed to be coated with a Teflon spray.

Both procedures were used to produce aortic mock root designed to be integrated in the pulse duplicator for PIV applications. The inner mould was made replicating the aortic root shape (previously described in Figure 71) and the external ones was designed with four flat surfaces to reduce the laser and camera distortion, as in Figure 73.

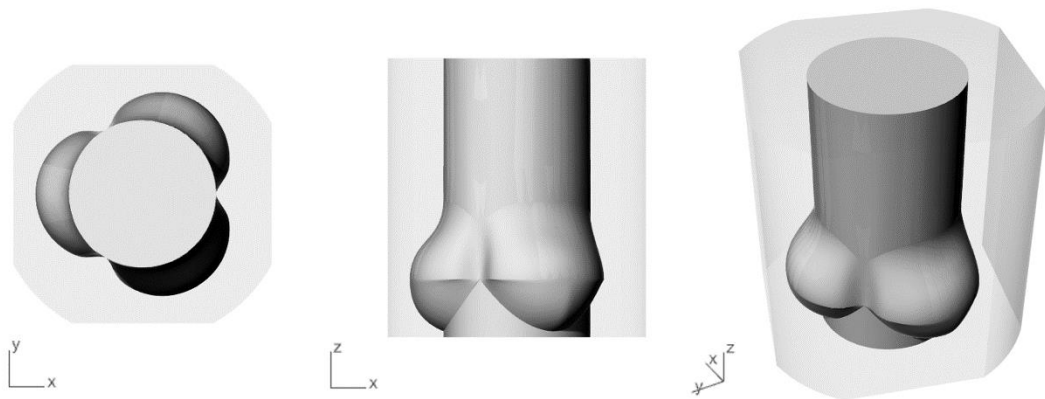


Figure 73 Aortic mock root 3D model

The mould was designed in Rhinoceros and 3D printed in resin by using a Form3 printer (Formlab). The mould consists of four external identical blocks, an inner mould with the aortic root shape, and a bottom mould that allows to connect and align the external and the inner moulds, in Figure 74b. The inner and bottom blocks were printed in a flexible resin, in order to be more adaptable. The external blocks were printed with a rigid resin (Figure 74b). Furthermore, the wall of the inner mould was designed to allow it to be extracted by squeezing it through the ascending aorta, preserving its integrity, the final mock root is shown in Figure 75.

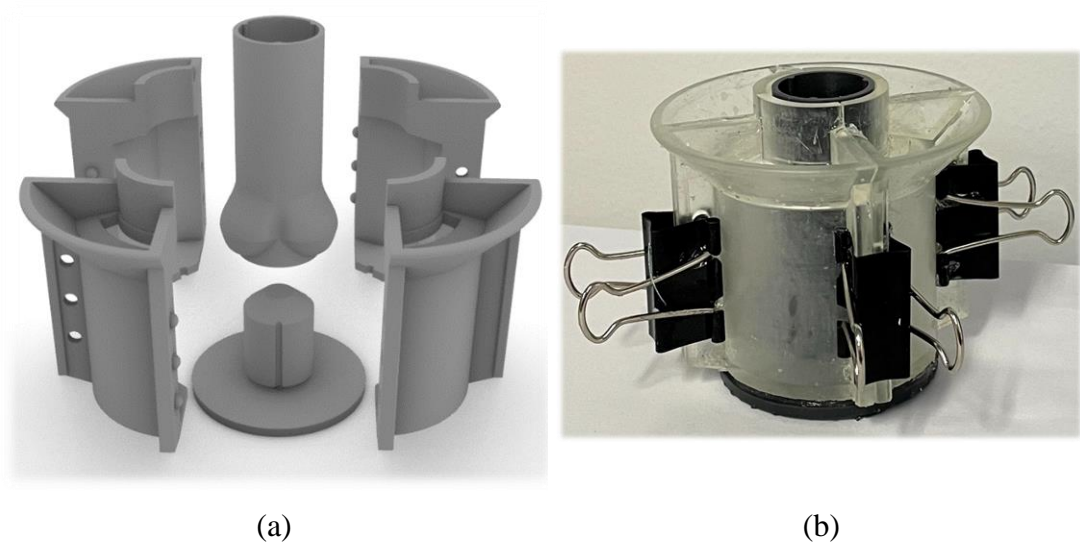


Figure 74 Mould for mock root realization a) 3D model b) printed mould

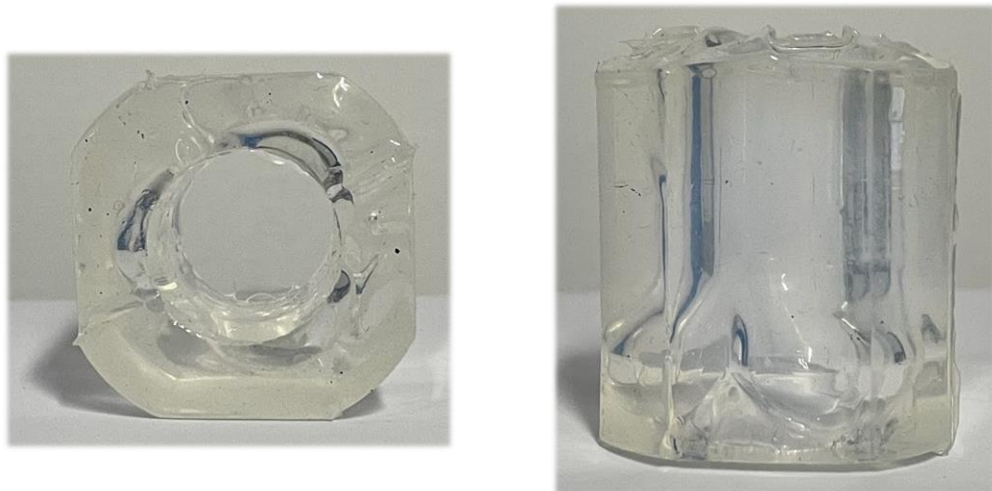


Figure 75 Sylgard-184 aortic mock root

Appendix D. Custom Heat Exchanger for sided liquids

Testing at body temperature is essential for a number of devices, especially if they are based on Nitinol, whose mechanical properties are strictly associated with the operating temperature (as described in section 4.1.1.2). To this purpose, the blood equivalent synthesised as part of this thesis for PIV applications (in section 4.2.3.2),

was designed to achieve the main physical properties as human blood at the physiological temperature of 37 °C.

The ViVitro pulse duplicator system (described in section 3.3.1) is equipped with a heat exchanger and a heat bath (in Figure 76) allowing to perform tests at body temperature. The heat exchanger is composed by 412 stainless steel tubes, and a separate outer shell tube [178]. When the pulse duplicator is running, the test fluid flows in the tubes and the bath fluid flows in the outer shell tube. The heat bath (in Figure 76 b) has the function to keep the bath fluid at constant temperature and to keep it moving in the outer circuit. This heat system, in conventional tests, acts as a resistance that contributes to increase the mean aortic pressure, and can be compensated by readjusting the systemic resistance of the system. However, this heat exchanger is not ideal for PIV applications, as the seeding needed for the test causes clogging in the stainless-steel tubes. To address this issue, a custom heat exchanger was designed and built.

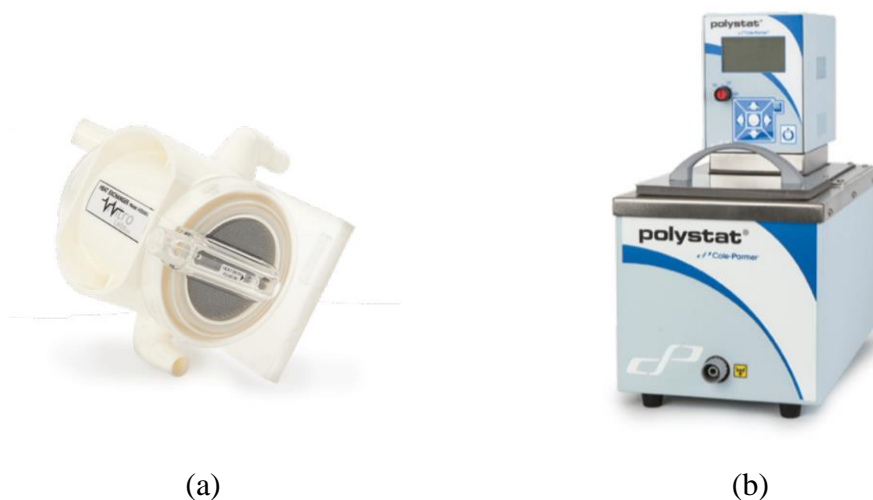


Figure 76 a) ViVitro heat exchanger, b) Heat bath

The custom heat exchanger (in Figure 77 and Figure 78) comprises:

- Two preformed heating mats;
- Foam for thermal insulation;
- Two thermocouples (TP100 and NTC);
- Custom connectors (Y and Elbow);
- Custom box;
- Two controllers.

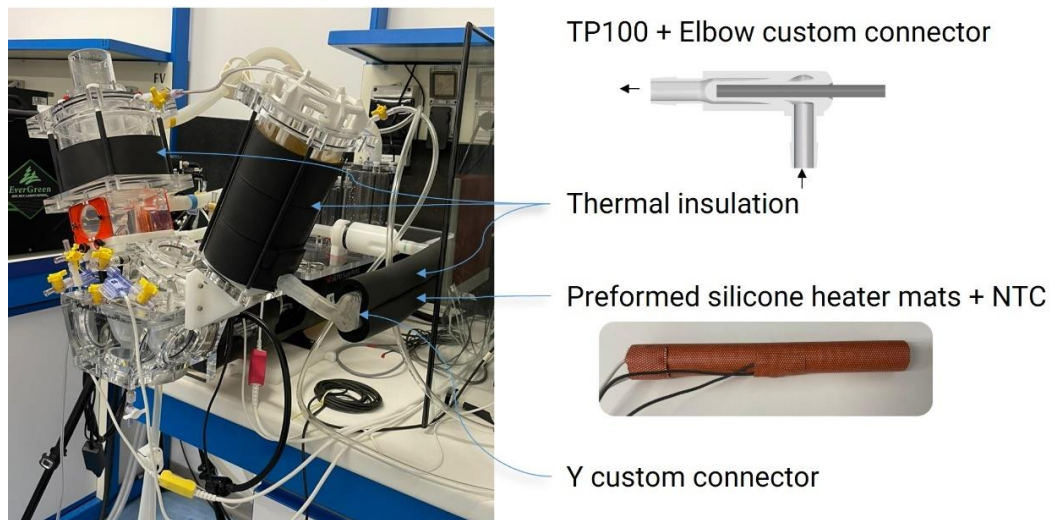
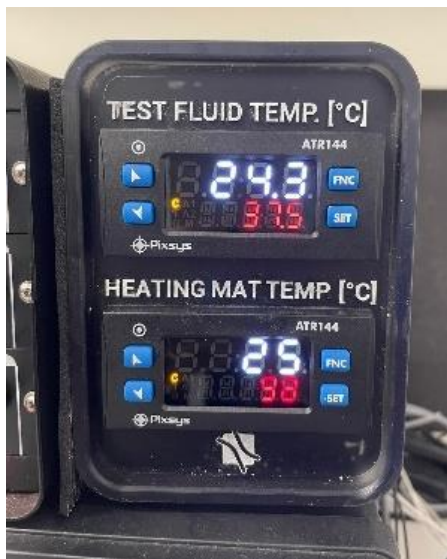


Figure 77 ViVitro setup for PIV tests at body temperature

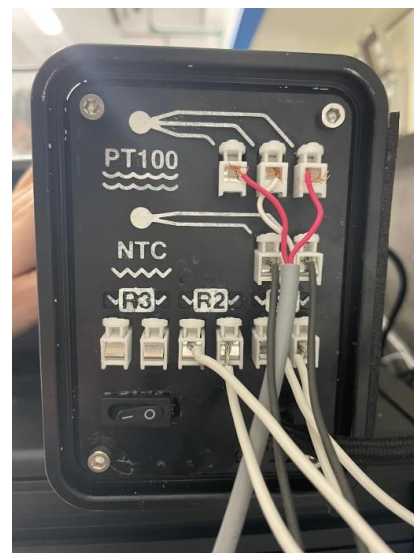
The electric circuit was made to allow a double control of the heating mat, to avoid mat overheats and to keep the test fluid at constant temperature. The preformed heating mat is composed of a resistance ($\varnothing 20 \text{ mm} \times 200 \text{ mm}$, 230 V, 30 W) and a NTC thermocouple incorporated in a cylindrical silicone shell. In particular, the NTC thermocouple was used to monitor the mat temperature, and the TP100 thermocouple to monitor the test fluid temperature.

To implement a double control, two controllers (PID controller ATR144 by Pixsys) were placed in series (sketch in Figure 79). The PID controller compare the

temperature set point (red number) with the actual temperature acquired with the thermocouple (white number) and if the acquired temperature exceeds the set point, the circuit is opened. The master controller regulates the heating mat temperature (NTC thermocouple) and, if the mat overheats, switches off the slave controller. Instead, the slave controller regulates the fluid temperature (PT100 thermocouple), and when the set point is exceeded, switches off the heating mats (placed in parallel). So, the heating mats are turned off both when the mat overheats and when the fluid temperature has reached the setpoint. The circuit connections were enclosed in a 3D printed box, in order to have a safe and user-friendly control (box in Figure 78).



(a)



(b)

Figure 78 Controlbox a) front panel, b) back panel

The system was implemented with two heating mats placed in parallel, because they have proved to be sufficient to maintain the test fluid temperature at 37 °C.

The custom heater was integrated in The ViVitro hydraulic system through 3D printed connectors designed for the purpose. ‘Y’ connectors were designed to place in parallel two silicone tubes, around which the heating mats were placed, instead the

elbow connector was designed to insulate the test fluid from the TP100 thermocouple for electromagnetic flowmeter protection (described in section 3.3.1). Foam thermal insulation was placed around the hydraulic system to reduce thermal dissipation.

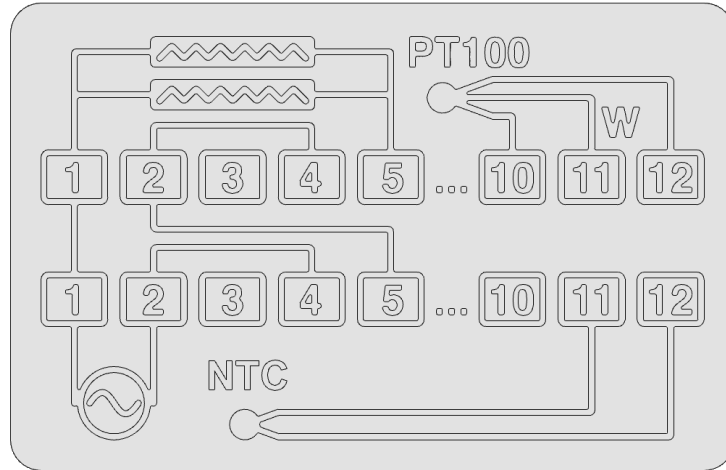


Figure 79 Electric circuit sketch

Bibliography

- [1] M. Raffel, C.E. Willert, S. Wereley, J. Kompenhans, Particle Image Velocity A Practical Guide, 2012.
- [2] M.A. Sutton, J.J. Orteu, H.W. Schreier, Image Correlation for Shape, Motion and Deformation Measurements, Springer US, Boston, MA, 2009. <https://doi.org/10.1007/978-0-387-78747-3>.
- [3] J. Blaber, B. Adair, A. Antoniou, Ncorr: Open-Source 2D Digital Image Correlation Matlab Software, *Exp. Mech.* 55 (2015) 1105–1122. <https://doi.org/10.1007/s11340-015-0009-1>.
- [4] W. Thielicke, E.J. Stamhuis, PIVlab – Towards User-friendly, Affordable and Accurate Digital Particle Image Velocimetry in MATLAB, *J. Open Res. Softw.* 2 (2014). <https://doi.org/10.5334/jors.bl>.
- [5] A. Ducci, F. Pirisi, S. Tzamtzis, G. Burriesci, Transcatheter aortic valves produce unphysiological flows which may contribute to thromboembolic events: An in-vitro study, *J. Biomech.* 49 (2016) 4080–4089. <https://doi.org/10.1016/j.jbiomech.2016.10.050>.
- [6] R. Toninato, J. Salmon, F.M. Susin, A. Ducci, G. Burriesci, Physiological vortices in the sinuses of Valsalva: An in vitro approach for bio-prosthetic valves, *J. Biomech.* 49 (2016) 2635–2643. <https://doi.org/10.1016/j.jbiomech.2016.05.027>.
- [7] H. Fehervary, M. Smoljkić, J. Vander Sloten, N. Famaey, Planar biaxial testing of soft biological tissue using rakes: A critical analysis of protocol and fitting process, *J. Mech. Behav. Biomed. Mater.* 61 (2016) 135–151. <https://doi.org/10.1016/j.jmbbm.2016.01.011>.
- [8] S. V. Bhagwat, V. V. Shukla, M.G. Trivedi, A. Jha, P. Padole, An engineering investigation of bio-polymers, *Int. J. Mech. Prod. Eng. Res. Dev.* 9 (2019) 348–355.
- [9] G. Burriesci, F.C. Marincola, C. Zervides, Design of a novel polymeric heart valve, *J. Med. Eng. Technol.* 34 (2010). <https://doi.org/10.3109/03091900903261241>.
- [10] Lambert, B. J., Tang, F. W., Rogers, W. J., *Polymers in medical applications*, (2001).
- [11] S. Daly, G. Ravichandran, K. Bhattacharya, Stress-induced martensitic phase transformation in thin sheets of Nitinol, *Acta Mater.* 55 (2007) 3593–3600. <https://doi.org/10.1016/j.actamat.2007.02.011>.
- [12] J.M. Dulieu-Barton, J. Eaton-Evans, E.G. Little, I.A. Brown, Thermoelastic Stress Analysis of Vascular Devices, in: E.E. Gdoutos (Ed.), *Exp. Anal. Nano Eng. Mater. Struct.*, Springer Netherlands, Dordrecht, 2007: pp. 5–6.
- [13] A. Szold, Nitinol: shape-memory and super-elastic materials in surgery, *Surg. Endosc.* 20 (2006) 1493–1496. <https://doi.org/10.1007/s00464-005-0867-1>.

- [14] S. Shabalovskaya, J. Anderegg, J. Van Humbeeck, Critical overview of Nitinol surfaces and their modifications for medical applications, *Acta Biomater.* 4 (2008) 447–467. <https://doi.org/10.1016/j.actbio.2008.01.013>.
- [15] C. V. Bourantas, P.W. Serruys, Evolution of transcatheter aortic valve replacement, *Circ. Res.* 114 (2014). <https://doi.org/10.1161/CIRCRESAHA.114.302292>.
- [16] A. Bose, M. Hartmann, H. Henkes, H.M. Liu, M.M.H. Teng, I. Szikora, A. Berlis, J. Reul, S.C.H. Yu, M. Forsting, M. Lui, W. Lim, S.P. Sit, A Novel, Self-Expanding, Nitinol Stent in Medically Refractory Intracranial Atherosclerotic Stenoses, *Stroke.* 38 (2007) 1531–1537. <https://doi.org/10.1161/STROKEAHA.106.477711>.
- [17] C. L’Acqua, E. Hod, New perspectives on the thrombotic complications of haemolysis, *Br. J. Haematol.* 168 (2015) 175–185. <https://doi.org/10.1111/bjh.13183>.
- [18] C. Bludszuweit, Model for a General Mechanical Blood Damage Prediction, *Artif. Organs.* 19 (1995) 583–589. <https://doi.org/10.1111/j.1525-1594.1995.tb02385.x>.
- [19] B. Taghizadeh, L. Ghavami, H. Derakhshankhah, E. Zangene, M. Razmi, M. Jaymand, P. Zarrintaj, N. Zarghami, M.R. Jaafari, M. Moallem Shahri, A. Moghaddasian, L. Tayebi, Z. Izadi, Biomaterials in Valvular Heart Diseases, *Front. Bioeng. Biotechnol.* 8 (2020). <https://doi.org/10.3389/fbioe.2020.529244>.
- [20] S.J. Phillips, Thrombogenic influence of biomaterials in patients with the Omni series heart valve: Pyrolytic carbon Versus titanium, *ASAIO J.* 47 (2001). <https://doi.org/10.1097/00002480-200109000-00002>.
- [21] American Society for Testing and Materials, ASTM E8/E8M standard test methods for tension testing of metallic materials 1, *Annu. B. ASTM Stand.* 4. (2010) 1–27. <https://doi.org/10.1520/E0008>.
- [22] A.R. Pelton, Nitinol fatigue: A review of microstructures and mechanisms, in: *J. Mater. Eng. Perform.*, 2011: pp. 613–617. <https://doi.org/10.1007/s11665-011-9864-9>.
- [23] American Society for Testing and Materials, ASTM F2516–14: Standard Test Method for Tension Testing of Nickel-Titanium Superelastic Materials, *ASTM Int.* (2015) 6. <https://doi.org/10.1520/F2516-14.2>.
- [24] P. Susan Standring DSc, *Gray’s Anatomy 41st edition: The Anatomical Basis of Clinical Practice*, 2015.
- [25] A. Quarteroni, L. Formaggia, A. Veneziani, Cardiovascular Mathematics: Modeling and simulation of the circulatory system, *Model. Simul. Appl.* 1 (2009).
- [26] <https://yourheartvalve.com/heart-basics/heart-valves/>, (n.d.).
- [27] A.P. Yoganathan, Z. He, S.C. Jones, Fluid mechanics of heart valves, *Annu. Rev. Biomed. Eng.* 6 (2004) 331–362.

<https://doi.org/10.1146/annurev.bioeng.6.040803.140111>.

- [28] V.T. Nkomo, J.M. Gardin, T.N. Skelton, J.S. Gottdiener, C.G. Scott, M. Enriquez-Sarano, Burden of valvular heart diseases: a population-based study, *Lancet*. 368 (2006). [https://doi.org/10.1016/S0140-6736\(06\)69208-8](https://doi.org/10.1016/S0140-6736(06)69208-8).
- [29] S.Y. Ho, Structure and anatomy of the aortic root, *Eur. J. Echocardiogr.* 10 (2009) i3–i10. <https://doi.org/10.1093/ejechocard/jen243>.
- [30] P. Nagpal, M.D. Agrawal, S.S. Saboo, S. Hedgire, S. Priya, M.L. Steigner, Imaging of the aortic root on high-pitch non-gated and ECG-gated CT: awareness is the key!, *Insights Imaging*. 11 (2020). <https://doi.org/10.1186/s13244-020-00855-w>.
- [31] C.M. Otto, B. Prendergast, Aortic-Valve Stenosis — From Patients at Risk to Severe Valve Obstruction, *N. Engl. J. Med.* 371 (2014). <https://doi.org/10.1056/nejmra1313875>.
- [32] P. Nataf, E. Lansac, Dilation of the thoracic aorta: Medical and surgical management, *Heart*. 92 (2006). <https://doi.org/10.1136/hrt.2005.074781>.
- [33] A. Kamal, A. Faraz, B.C. Vasavada, I.A. Khan, Prosthetic heart valves : Types and echocardiographic evaluation, 122 (2007) 99–110. <https://doi.org/10.1016/j.ijcard.2006.12.037>.
- [34] J. Butany, M.S. Ahluwalia, C. Fayet, C. Munroe, P. Blit, C. Ahn, Hufnagel valve: The first prosthetic mechanical valve, *Cardiovasc. Pathol.* 11 (2002). [https://doi.org/10.1016/S1054-8807\(02\)00132-1](https://doi.org/10.1016/S1054-8807(02)00132-1).
- [35] R.A. North, L. Sadler, A.W. Stewart, L.M.E. McCowan, A.R. Kerr, H.D. White, Long-term survival and valve-related complications in young women with cardiac valve replacements, *Circulation*. 99 (1999). <https://doi.org/10.1161/01.CIR.99.20.2669>.
- [36] L.P. Dasi, H.A. Simon, P. Sucusky, A.P. Yoganathan, Fluid mechanics of artificial heart valves, *Clin. Exp. Pharmacol. Physiol.* 36 (2009). <https://doi.org/10.1111/j.1440-1681.2008.05099.x>.
- [37] J.M. Duncan, D.A. Cooley, J.J. Livesay, The St. Jude Medical valve: Early clinical results in 253 patients, *Texas Hear. Inst. J.* 10 (1983).
- [38] M. Magarakis, A.E. Macias, A. Ghodsizad, T.A. Salerno, Surgical Management of Cardiovascular Thrombotic Conditions, in: *Cardiovasc. Thrombus*, Elsevier, 2018: pp. 367–376. <https://doi.org/10.1016/B978-0-12-812615-8.00025-9>.
- [39] https://americanhistory.si.edu/collections/search/object/nmah_1726277, (n.d.).
- [40] N. Ural, *Clinical Manual and Review of Transesophageal Echocardiography, Second Edition*, Anesthesiology. 116 (2012). <https://doi.org/10.1097/aln.0b013e318249cf90>.
- [41] D.S. Bach, M.P. Sakwa, M. Goldbach, M.R. Petracek, R.W. Emery, F.W. Mohr, D. Fullerton, J. Laas, Hemodynamics and early clinical performance of the St. Jude Medical Regent mechanical aortic valve, *Ann. Thorac. Surg.* 74 (2002). [https://doi.org/10.1016/S0003-4975\(02\)04034-1](https://doi.org/10.1016/S0003-4975(02)04034-1).

- [42] G.L. Grunkemeier, W.N. Anderson, Clinical evaluation and analysis of heart valve substitutes, *J. Heart Valve Dis.* 7 (1998).
- [43] Edwards, www.edwards.com, (n.d.).
- [44] A. Cribier, H. Eltchaninoff, A. Bash, N. Borenstein, C. Tron, F. Bauer, G. Derumeaux, F. Anselme, F. Laborde, M.B. Leon, Percutaneous transcatheter implantation of an aortic valve prosthesis for calcific aortic stenosis: First human case description, *Circulation.* 106 (2002). <https://doi.org/10.1161/01.CIR.0000047200.36165.B8>.
- [45] M. Bianchi, G. Marom, R.P. Ghosh, H.A. Fernandez, J.R. Taylor, M.J. Slepian, D. Bluestein, Effect of Balloon-Expandable Transcatheter Aortic Valve Replacement Positioning: A Patient-Specific Numerical Model, *Artif. Organs.* 40 (2016). <https://doi.org/10.1111/aor.12806>.
- [46] E. Van Belle, F. Vincent, J. Labreuche, V. Auffret, N. Debry, T. Lefèvre, H. Eltchaninoff, T. Manigold, M. Gilard, J.-P. Verhoye, D. Himbert, R. Koning, J.-P. Collet, P. Leprince, E. Teiger, A. Duhamel, A. Cosenza, G. Schurtz, S. Porouchani, B. Lattuca, E. Robin, A. Coisne, T. Modine, M. Richardson, P. Joly, G. Rioufol, S. Ghostine, O. Bar, N. Amabile, D. Champagnac, P. Ohlmann, N. Meneveau, T. Lhermusier, L. Leroux, F. Leclercq, T. Gandet, F. Pinaud, T. Cuisset, P. Motreff, G. Souteyrand, B. Iung, T. Folliguet, P. Commeau, G. Cayla, G. Bayet, O. Darremont, C. Spaulding, H. Le Breton, C. Delhay, Balloon-Expandable Versus Self-Expanding Transcatheter Aortic Valve Replacement, *Circulation.* 141 (2020). <https://doi.org/10.1161/circulationaha.119.043785>.
- [47] J.P. Fanning, D.G. Platts, D.L. Walters, J.F. Fraser, Transcatheter aortic valve implantation (TAVI): Valve design and evolution, *Int. J. Cardiol.* 168 (2013) 1822–1831. <https://doi.org/10.1016/j.ijcard.2013.07.117>.
- [48] T. Ishihara, V.J. Ferrans, M. Jones, S.W. Boyce, O. Kawanami, W.C. Roberts, Histologic and ultrastructural features of normal human parietal pericardium, *Am. J. Cardiol.* 46 (1980) 744–753. [https://doi.org/10.1016/0002-9149\(80\)90424-5](https://doi.org/10.1016/0002-9149(80)90424-5).
- [49] M.S. Sacks, Biaxial mechanical evaluation of planar biological materials, *J. Elast.* 61 (2000) 199–246. <https://doi.org/10.1023/A:1010917028671>.
- [50] B. BRITISH STANDARD, BS 903-5 Physical testing of rubber. Part 1: Guide to the selection and use of methods of test for rubber., (1995).
- [51] S. De Gelidi, G. Tozzi, A. Bucchi, The role of pre-conditioning frequency in the experimental characterization of hyper-elastic materials as models for soft tissue applications, *Int. J. Appl. Mech.* 8 (2016). <https://doi.org/10.1142/S1758825116500666>.
- [52] X. Huang, G.J. Ackland, K.M. Rabe, Crystal structures and shape-memory behaviour of NiTi, *Nat. Mater.* 2 (2003) 307–311. <https://doi.org/10.1038/nmat884>.
- [53] E. Sgambitterra, L. Bruno, C. Maletta, Stress induced martensite at the crack tip

- in NiTi alloys during fatigue loading, *Frat. Ed Integrità Strutt.* 8 (2014) 167–173. <https://doi.org/10.3221/IGF-ESIS.30.22>.
- [54] V.I. Itin, V.E. Gyunter, S.A. Shabalovskaya, R.L.C. Sachdeva, Mechanical properties and shape memory of porous nitinol, *Mater. Charact.* 32 (1994) 179–187. [https://doi.org/10.1016/1044-5803\(94\)90087-6](https://doi.org/10.1016/1044-5803(94)90087-6).
- [55] J.M. Gallardo Fuentes, P. Gümpel, J. Strittmatter, Phase Change Behavior of Nitinol Shape Memory Alloys, *Adv. Eng. Mater.* 4 (2002) 437–452. [https://doi.org/10.1002/1527-2648\(20020717\)4:7<437::AID-ADEM437>3.0.CO;2-8](https://doi.org/10.1002/1527-2648(20020717)4:7<437::AID-ADEM437>3.0.CO;2-8).
- [56] B. Wang, S. Zhu, Seismic behavior of self-centering reinforced concrete wall enabled by superelastic shape memory alloy bars, *Bull. Earthq. Eng.* 16 (2018). <https://doi.org/10.1007/s10518-017-0213-8>.
- [57] G. Song, N. Ma, H.-N. Li, Applications of shape memory alloys in civil structures, *Eng. Struct.* 28 (2006) 1266–1274. <https://doi.org/10.1016/j.engstruct.2005.12.010>.
- [58] L. Petrini, F. Migliavacca, Biomedical Applications of Shape Memory Alloys, *J. Metall.* 2011 (2011) 1–15. <https://doi.org/10.1155/2011/501483>.
- [59] A. AJOVALASIT, D. CERNIGLIA, G. PETRUCCI, G. PITARRESI, *Introduzione alla meccanica sperimentale dei solidi*; Canterano; Aracne editrice, 2018.
- [60] S. Scharnowski, C.J. Kähler, On the loss-of-correlation due to PIV image noise, *Exp. Fluids.* 57 (2016) 1–12. <https://doi.org/10.1007/s00348-016-2203-z>.
- [61] J.C.F. Jorge, L.F.G.D. Souza, M.C. Mendes, I.S. Bott, L.S. Araújo, V.R.D. Santos, J.M.A. Rebello, G.M. Evans, Microstructure characterization and its relationship with impact toughness of C-Mn and high strength low alloy steel weld metals - A review, *J. Mater. Res. Technol.* 10 (2021). <https://doi.org/10.1016/j.jmrt.2020.12.006>.
- [62] Z. Guo, F. Zhou, J. Hao, W. Liu, Effects of system parameters on making aluminum alloy lotus, *J. Colloid Interface Sci.* 303 (2006). <https://doi.org/10.1016/j.jcis.2006.06.067>.
- [63] TSI, <https://tsi.com/home/>, (n.d.).
- [64] H. Huang, D. Dabiri, M. Gharib, On errors of digital particle image velocimetry, *Meas. Sci. Technol.* 8 (1997) 1427–1440. <https://doi.org/10.1088/0957-0233/8/12/007>.
- [65] E.J. Stamhuis, Basics and principles of particle image velocimetry (PIV) for mapping biogenic and biologically relevant flows, *Aquat. Ecol.* 40 (2006) 463–479. <https://doi.org/10.1007/s10452-005-6567-z>.
- [66] W. Thielicke, R. Sonntag, Particle Image Velocimetry for MATLAB: Accuracy and enhanced algorithms in PIVlab, *J. Open Res. Softw.* 9 (2021). <https://doi.org/10.5334/JORS.334>.
- [67] H. Huang, D. Dabiri, M. Gharib, On errors of digital particle image velocimetry,

- Meas. Sci. Technol. 8 (1997) 1427–1440. <https://doi.org/10.1088/0957-0233/8/12/007>.
- [68] J. Westerweel, D. Dabiri, M. Gharib, The effect of a discrete window offset on the accuracy of cross-correlation analysis of digital PIV recordings, *Exp. Fluids*. 23 (1997) 20–28. <https://doi.org/10.1007/s003480050082>.
- [69] Tecplot, <https://www.tecplot.com/>, (n.d.).
- [70] G. Pitarresi, E.A. Patterson, A review of the general theory of thermoelastic stress analysis, *J. Strain Anal. Eng. Des.* 38 (2003) 405–417. <https://doi.org/10.1243/03093240360713469>.
- [71] M.A. Biot, Thermoelasticity and irreversible thermodynamics, *J. Appl. Phys.* 27 (1956) 240–253. <https://doi.org/10.1063/1.1722351>.
- [72] A.K. Wong, R. Jones, J.G. Sparrow, Thermoelastic constant or thermoelastic parameter?, *J. Phys. Chem. Solids*. 48 (1987). [https://doi.org/10.1016/0022-3697\(87\)90071-0](https://doi.org/10.1016/0022-3697(87)90071-0).
- [73] A.K. Wong, J.G. Sparrow, S.A. Dunn, On the revised theory of the thermoelastic effect, *J. Phys. Chem. Solids*. 49 (1988). [https://doi.org/10.1016/0022-3697\(88\)90099-6](https://doi.org/10.1016/0022-3697(88)90099-6).
- [74] M. Catanho, M. Sinha, V. Vijayan, Model of Aortic Blood Flow Using the Windkessel Effect, *Math. Methods Bioeng.* (2012).
- [75] N. Westerhof, G. Elzinga, P. Sipkema, An artificial arterial system for pumping hearts., *J. Appl. Physiol.* 31 (1971) 776–781. <https://doi.org/10.1152/jappl.1971.31.5.776>.
- [76] A.C. Mellinghoff, A.J. Reininger, L.J. Wurzinger, R. Landgraf, K.D. Hepp, Influence of glycemic control on viscosity and density of plasma and whole blood in Type-1 diabetic patients, *Diabetes Res. Clin. Pract.* 33 (1996) 75–82. [https://doi.org/10.1016/0168-8227\(96\)01279-X](https://doi.org/10.1016/0168-8227(96)01279-X).
- [77] Vivitro, <https://vivotrolabs.com/>, (n.d.).
- [78] B. BRITISH STANDARD, BS EN ISO 5840 - 3: 2021 BSI Standards Publication Cardiovascular implants — Cardiac valve prostheses, (2021).
- [79] R. Gorlin, S.G. Gorlin, Hydraulic formula for calculation of the area of the stenotic mitral valve, other cardiac valves, and central circulatory shunts. I, *Am. Heart J.* 41 (1951). [https://doi.org/10.1016/0002-8703\(51\)90002-6](https://doi.org/10.1016/0002-8703(51)90002-6).
- [80] A. Wadood, Brief overview on nitinol as biomaterial, *Adv. Mater. Sci. Eng.* 2016 (2016). <https://doi.org/10.1155/2016/4173138>.
- [81] M. Frost, P. Sedlák, P. Sedmák, L. Heller, P. Šittner, SMA Constitutive Modeling Backed Up by 3D-XRD Experiments: Transformation Front in Stretched NiTi Wire, *Shape Mem. Superelasticity*. 4 (2018) 411–416. <https://doi.org/10.1007/s40830-018-0192-x>.
- [82] L. Zheng, Y. He, Z. Moumni, Effects of Lüders-like bands on NiTi fatigue behaviors, *Int. J. Solids Struct.* 83 (2016) 28–44. <https://doi.org/10.1016/j.ijsolstr.2015.12.021>.

- [83] D.C. Lagoudas, *Shape Memory Alloys: modeling and engineering applications*, 2008. <https://doi.org/https://doi.org/10.1007/978-0-387-47685-8>.
- [84] E. McCumiskey, W.M. Dempster, D.H. Nash, T.R. Ashton, D.G. Stevenson, The determination and evaluation of nitinol constitutive models for finite element analysis, in: *Appl. Mech. Mater.*, 2007: pp. 81–88. <https://doi.org/10.4028/www.scientific.net/AMM.7-8.81>.
- [85] E. Masoumi Khalil Abad, D. Pasini, R. Cecere, Shape optimization of stress concentration-free lattice for self-expandable Nitinol stent-grafts, *J. Biomech.* 45 (2012). <https://doi.org/10.1016/j.jbiomech.2012.01.002>.
- [86] C. Bewerse, K.R. Gall, G.J. Mcfarland, P. Zhu, L.C. Brinson, A Local and global strains and strain ratios in shape memory alloys using digital image correlation, *Mater. Sci. Eng. A.* 568 (2013) 134–142. <https://doi.org/10.1016/j.msea.2013.01.030>.
- [87] G.M. Hassan, Digital Image Correlation for discontinuous displacement measurement using subset segmentation, *Opt. Lasers Eng.* 115 (2019) 208–216. <https://doi.org/10.1016/j.optlaseng.2018.12.003>.
- [88] R.H. Pritchard, P. Lava, D. Debruyne, E.M. Terentjev, Precise determination of the Poisson ratio in soft materials with 2D digital image correlation, *Soft Matter.* 9 (2013) 6037–6045. <https://doi.org/10.1039/c3sm50901j>.
- [89] G. Ananthakrishna, Current theoretical approaches to collective behavior of dislocations, *Phys. Rep.* 440 (2007) 113–259. <https://doi.org/https://doi.org/10.1016/j.physrep.2006.10.003>.
- [90] W.B. Cross, A.H. Kariotis, F. J. Stimler, Nitinol characterization study, NASA CR- 1433. (1969).
- [91] S. Qiu, B. Clausen, S.A. Padula, R.D. Noebe, R. Vaidyanathan, On elastic moduli and elastic anisotropy in polycrystalline martensitic NiTi, *Acta Mater.* 59 (2011) 5055–5066. <https://doi.org/https://doi.org/10.1016/j.actamat.2011.04.018>.
- [92] C. Kleinstreuer, Z. Li, C. a. Basciano, S. Seelecke, M. a. Farber, Computational mechanics of Nitinol stent grafts, *J. Biomech.* 41 (2008) 2370–2378. <https://doi.org/10.1016/j.jbiomech.2008.05.032>.
- [93] P. Schlosser, D. Favier, H. Louche, L. Orgéas, Experimental Characterization of NiTi SMAs Thermomechanical Behaviour Using Temperature and Strain Full-Field Measurements, *Adv. Sci. Technol.* 59 (2009) 140–149. <https://doi.org/10.4028/www.scientific.net/ast.59.140>.
- [94] K. Kim, S. Daly, Martensite Strain Memory in the Shape Memory Alloy Nickel-Titanium Under Mechanical Cycling, *Exp. Mech.* 51 (2011) 641–652. <https://doi.org/10.1007/s11340-010-9435-2>.
- [95] H. Ossmer, F. Lambrecht, M. Gültig, C. Chluba, E. Quandt, M. Kohl, Evolution of temperature profiles in TiNi films for elastocaloric cooling, *Acta Mater.* 81 (2014) 9–20. <https://doi.org/10.1016/j.actamat.2014.08.006>.
- [96] G.J. Pataky, E. Ertekin, H. Sehitoglu, Elastocaloric cooling potential of NiTi,

- Ni₂FeGa, and CoNiAl, *Acta Mater.* 96 (2015) 420–427. <https://doi.org/10.1016/j.actamat.2015.06.011>.
- [97] D. Delpueyo, M. Grédiac, X. Balandraud, C. Badulescu, Investigation of martensitic microstructures in a monocrystalline Cu-Al-Be shape memory alloy with the grid method and infrared thermography, *Mech. Mater.* 45 (2012) 34–51. <https://doi.org/10.1016/j.mechmat.2011.09.007>.
- [98] Y. Xiao, P. Zeng, L. Lei, H. Du, Local Mechanical Response of Superelastic NiTi Shape-Memory Alloy Under Uniaxial Loading, *Shape Mem. Superelasticity.* 1 (2015) 468–478. <https://doi.org/10.1007/s40830-015-0037-9>.
- [99] X. Xie, Q. Kan, G. Kang, J. Li, B. Qiu, C. Yu, Observation on the transformation domains of super-elastic NiTi shape memory alloy and their evolutions during cyclic loading, *Smart Mater. Struct.* 25 (2016) 0. <https://doi.org/10.1088/0964-1726/25/4/045003>.
- [100] E. Sgambitterra, P. Magarò, F. Niccoli, D. Renzo, C. Maletta, Novel insight into the strain-life fatigue properties of pseudoelastic NiTi shape memory alloys, *Smart Mater. Struct.* 28 (2019) 10LT03. <https://doi.org/10.1088/1361-665X/ab3df1>.
- [101] F. Furgiuele, P. Magarò, C. Maletta, E. Sgambitterra, Functional and Structural Fatigue of Pseudoelastic NiTi: Global Vs Local Thermo-Mechanical Response, *Shape Mem. Superelasticity.* 6 (2020) 242–255. <https://doi.org/10.1007/s40830-020-00289-9>.
- [102] H. Yin, M. Li, Q. Sun, Thermomechanical coupling in cyclic phase transition of shape memory material under periodic stressing—experiment and modeling, *J. Mech. Phys. Solids.* (2021) 104199. <https://doi.org/10.1016/j.jmps.2020.104199>.
- [103] Y. Zhang, Y. You, Z. Moumni, G. Anlas, J. Zhu, W. Zhang, Experimental and theoretical investigation of the frequency effect on low cycle fatigue of shape memory alloys, *Int. J. Plast.* 90 (2017) 1–30. <https://doi.org/10.1016/j.ijplas.2016.11.012>.
- [104] L. Zheng, Y. He, Z. Moumni, Investigation on fatigue behaviors of NiTi polycrystalline strips under stress-controlled tension via in-situ macro-band observation, *Int. J. Plast.* 90 (2017) 116–145. <https://doi.org/10.1016/j.ijplas.2016.12.008>.
- [105] J. Tušek, A. Žerovnik, M. Čebren, M. Brojan, B. Žužek, K. Engelbrecht, A. Cadelli, Elastocaloric effect vs fatigue life: Exploring the durability limits of Ni-Ti plates under pre-strain conditions for elastocaloric cooling, *Acta Mater.* 150 (2018) 295–307. <https://doi.org/10.1016/j.actamat.2018.03.032>.
- [106] J. Eaton-Evans, J.M. Dulieu-Barton, E.G. Little, I.A. Brown, Thermoelastic studies on Nitinol stents, *J. Strain Anal. Eng. Des.* 41 (2006) 481–495. <https://doi.org/10.1243/03093247JSA195>.
- [107] G. Pitarresi, Lock-In Signal Post-Processing Techniques in Infra-Red Thermography for Materials Structural Evaluation, *Exp. Mech.* 55 (2015) 667–

680. <https://doi.org/10.1007/s11340-013-9827-1>.

- [108] I. Rehman, A. Rehman, *Anatomy, Thorax, Pericardium*, 2018.
- [109] Y.C. Fung, S.C. Cowin, *Biomechanics: Mechanical Properties of Living Tissues*, 2nd ed., *J. Appl. Mech.* 61 (1994) 1007–1007. <https://doi.org/10.1115/1.2901550>.
- [110] D.P. Sokolis, H. Boudoulas, P.E. Karayannacos, Assessment of the aortic stress-strain relation in uniaxial tension, *J. Biomech.* 35 (2002). [https://doi.org/10.1016/S0021-9290\(02\)00073-8](https://doi.org/10.1016/S0021-9290(02)00073-8).
- [111] O.A. Shergold, N.A. Fleck, D. Radford, The uniaxial stress versus strain response of pig skin and silicone rubber at low and high strain rates, *Int. J. Impact Eng.* 32 (2006) 1384–1402. <https://doi.org/10.1016/j.ijimpeng.2004.11.010>.
- [112] M.S. Sacks, W. David Merryman, D.E. Schmidt, On the biomechanics of heart valve function, *J. Biomech.* 42 (2009). <https://doi.org/10.1016/j.jbiomech.2009.05.015>.
- [113] MSC Software, *Marc 2016 - Volume A: Theory and user information*, Msc. Software, Palo Alto, USA. (2016) 82–85. <http://scholar.google.com/scholar?hl=en&btnG=Search&q=intitle:Volume+A+:+Theory+and+User+Information#0>.
- [114] BRITISH STANDARD, *ISO 37:2011 Rubber, vulcanized or thermoplastic — Determination of tensile stress-strain properties*, (2011).
- [115] R.W. Ogden, *LARGE DEFORMATION ISOTROPIC ELASTICITY - ON THE CORRELATION OF THEORY AND EXPERIMENT FOR INCOMPRESSIBLE RUBBERLIKE SOLIDS.*, *Rubber Chem. Technol.* 46 (1973). <https://doi.org/10.5254/1.3542910>.
- [116] M. Rackl, *Article + Errata Curve Fitting for Ogden, Yeoh and Polynomial Models*, *Ostbayerische Tech. Hochschule Regensburg*. (2017).
- [117] D.C. Miller, Valve-sparing aortic root replacement in patients with the Marfan syndrome, *J. Thorac. Cardiovasc. Surg.* 125 (2003) 773–778. <https://doi.org/10.1067/MTC.2003.162>.
- [118] R. De Paulis, G.M. De Matteis, P. Nardi, R. Scaffa, D.F. Colella, L. Chiarello, A new aortic Dacron conduit for surgical treatment of aortic root pathology., *Ital. Heart J.* 1 (2000) 457–63. <http://www.ncbi.nlm.nih.gov/pubmed/10933327>.
- [119] M.J. Paulsen, P. Kasinpila, A.M. Imbrie-Moore, H. Wang, C.E. Hironaka, T.K. Koyano, R. Fong, P. Chiu, A.B. Goldstone, A.N. Steele, L.M. Stapleton, M. Ma, Y.J. Woo, Modeling conduit choice for valve-sparing aortic root replacement on biomechanics with a 3-dimensional–printed heart simulator, *J. Thorac. Cardiovasc. Surg.* 158 (2019) 392–403. <https://doi.org/10.1016/j.jtcvs.2018.10.145>.
- [120] E. Beckmann, A. Leone, A. Martens, ... C.M.-T.A. of thoracic, undefined 2020, Comparison of two strategies for aortic valve-sparing root replacement,

Elsevier. (n.d.).

- [121] M.J. Paulsen, A.M. Imbrie-Moore, M. Baiocchi, H. Wang, C.E. Hironaka, H.J. Lucian, J.M. Farry, A.D. Thakore, Y. Zhu, M. Ma, J.W. MacArthur, Y.J. Woo, Comprehensive Ex Vivo Comparison of 5 Clinically Used Conduit Configurations for Valve-Sparing Aortic Root Replacement Using a 3-Dimensional-Printed Heart Simulator, *Circulation*. (2020) 1361–1373. <https://doi.org/10.1161/CIRCULATIONAHA.120.046612>.
- [122] G. Pisani, R. Scaffa, O. Ieropoli, E.M. Dell’Amico, D. Maselli, U. Morbiducci, R. De Paulis, Role of the sinuses of Valsalva on the opening of the aortic valve, *J. Thorac. Cardiovasc. Surg.* 145 (2013) 999–1003. <https://doi.org/10.1016/j.jtcvs.2012.03.060>.
- [123] A.M. Tango, J. Salmons smith, A. Ducci, G. Burriesci, Validation and Extension of a Fluid–Structure Interaction Model of the Healthy Aortic Valve, *Cardiovasc. Eng. Technol.* 9 (2018) 739–751. <https://doi.org/10.1007/s13239-018-00391-1>.
- [124] T.E. David, C.M. Feindel, An aortic valve-sparing operation for patients with aortic incompetence and aneurysm of the ascending aorta, in: *J. Thorac. Cardiovasc. Surg.*, Mosby, 1992: pp. 617–622. [https://doi.org/10.1016/s0022-5223\(19\)34942-6](https://doi.org/10.1016/s0022-5223(19)34942-6).
- [125] B.J. Bellhouse, L. Talbot, The fluid mechanics of the aortic valve, *J. Fluid Mech.* 35 (1969) 721–735. <https://doi.org/10.1017/S0022112069001406>.
- [126] A. Salica, G. Pisani, U. Morbiducci, R. Scaffa, D. Massai, A. Audenino, L. Weltert, L. Guerrieri Wolf, R. De Paulis, The combined role of sinuses of Valsalva and flow pulsatility improves energy loss of the aortic valve, *Eur. J. Cardio-Thoracic Surg.* 49 (2016) 1222–1227. <https://doi.org/10.1093/ejcts/ezv311>.
- [127] N. Saikrishnan, G. Kumar, F.J. Sawaya, S. Lerakis, A.P. Yoganathan, Accurate assessment of aortic stenosis: A review of diagnostic modalities and hemodynamics, *Circulation*. 129 (2014) 244–253. <https://doi.org/10.1161/CIRCULATIONAHA.113.002310>.
- [128] D. Garcia, L. Kadem, What do you mean by aortic valve area: Geometric orifice area, effective orifice area, or Gorlin area?, *J. Heart Valve Dis.* 15 (2006) 601–608.
- [129] I.G. Burwash, D.D. Thomas, M. Sadahiro, A.S. Pearlman, E.D. Verrier, R. Thomas, C.D. Kraft, C.M. Otto, Dependence of Gorlin formula and continuity equation valve areas on transvalvular volume flow rate in valvular aortic stenosis, *Circulation*. 89 (1994). <https://doi.org/10.1161/01.CIR.89.2.827>.
- [130] J.A. Salmons smith, A. Ducci, G. Burriesci, Does transcatheter aortic valve alignment matter?, *Open Hear.* 6 (2019) 1–10. <https://doi.org/10.1136/openhrt-2019-001132>.
- [131] J. Garcia, L. Kadem, E. Larose, M.-A. Clavel, P. Pibarot, Comparison between cardiovascular magnetic resonance and transthoracic doppler echocardiography for the estimation of effective orifice area in aortic stenosis, *J. Cardiovasc.*

Magn. Reson. 13 (2011) 25. <https://doi.org/10.1186/1532-429X-13-25>.

- [132] J.G. Dumesnil, A.P. Yoganathan, Theoretical and practical differences between the Gorlin formula and the continuity equation for calculating aortic and mitral valve areas, *Am. J. Cardiol.* 67 (1991) 1268–1272. [https://doi.org/10.1016/0002-9149\(91\)90939-I](https://doi.org/10.1016/0002-9149(91)90939-I).
- [133] S.R. Cannon, K.L. Richards, M. Crawford, Hydraulic estimation of stenotic orifice area: A correction of the Gorlin formula, *Circulation.* 71 (1985). <https://doi.org/10.1161/01.CIR.71.6.1170>.
- [134] R.A. Migliore, M.E. Adaniya, M. Barranco, G. Miramont, S. Gonzalez, H. Tamagusuku, Estimation of Contraction Coefficient of Gorlin Equation for Assessment of Aortic Valve Area in Aortic Stenosis, *World J. Cardiovasc. Dis.* 07 (2017) 119–130. <https://doi.org/10.4236/wjcd.2017.74012>.
- [135] J.-C. Tardif, A.G. Rodrigues, J.-F. Hardy, Y. Leclerc, R. Petitclerc, R. Mongrain, L.-A. Mercier, Simultaneous Determination of Aortic Valve Area by the Gorlin Formula and by Transesophageal Echocardiography Under Different Transvalvular Flow Conditions, *J. Am. Coll. Cardiol.* 29 (1997) 1296–1302. [https://doi.org/10.1016/S0735-1097\(97\)00060-0](https://doi.org/10.1016/S0735-1097(97)00060-0).
- [136] C. Guivier-Curien, V. Deplano, E. Bertrand, Validation of a numerical 3-D fluid–structure interaction model for a prosthetic valve based on experimental PIV measurements, *Med. Eng. Phys.* 31 (2009) 986–993. <https://doi.org/10.1016/j.medengphy.2009.05.012>.
- [137] I. Kemp, K. Dellimore, R. Rodriguez, C. Scheffer, D. Blaine, H. Weich, A. Doubell, Experimental validation of the fluid–structure interaction simulation of a bioprosthetic aortic heart valve, *Australas. Phys. Eng. Sci. Med.* 36 (2013) 363–373. <https://doi.org/10.1007/s13246-013-0213-1>.
- [138] A.D. Bordones, M. Leroux, V.O. Kheyfets, Y.-A. Wu, C.-Y. Chen, E.A. Finol, Computational Fluid Dynamics Modeling of the Human Pulmonary Arteries with Experimental Validation, *Ann. Biomed. Eng.* 46 (2018) 1309–1324. <https://doi.org/10.1007/s10439-018-2047-1>.
- [139] A. Sciacchitano, Uncertainty quantification in particle image velocimetry, *Meas. Sci. Technol.* 30 (2019). <https://doi.org/10.1088/1361-6501/ab1db8>.
- [140] P.S. Gunning, N. Saikrishnan, L.M. Mcnamara, A.P. Yoganathan, An in vitro evaluation of the impact of eccentric deployment on transcatheter aortic valve hemodynamics, *Ann. Biomed. Eng.* 42 (2014) 1195–1206. <https://doi.org/10.1007/s10439-014-1008-6>.
- [141] M. Heitkemper, H. Hatoum, L.P. Dasi, In vitro hemodynamic assessment of a novel polymeric transcatheter aortic valve, *J. Mech. Behav. Biomed. Mater.* 98 (2019) 163–171. <https://doi.org/10.1016/j.jmbbm.2019.06.016>.
- [142] W.L. Lim, Y.T. Chew, T.C. Chew, H.T. Low, Steady flow dynamics of prosthetic aortic heart valves: A comparative evaluation with PIV techniques, *J. Biomech.* 31 (1998). [https://doi.org/10.1016/S0021-9290\(98\)00026-8](https://doi.org/10.1016/S0021-9290(98)00026-8).
- [143] N. Saikrishnan, C.H. Yap, N.C. Milligan, N. V. Vasilyev, A.P. Yoganathan, In

- vitro characterization of bicuspid aortic valve hemodynamics using particle image velocimetry, *Ann. Biomed. Eng.* 40 (2012) 1760–1775. <https://doi.org/10.1007/s10439-012-0527-2>.
- [144] H. Hatoum, A. Yousefi, S. Lilly, P. Maureira, J. Crestanello, L.P. Dasi, An in vitro evaluation of turbulence after transcatheter aortic valve implantation, *J. Thorac. Cardiovasc. Surg.* 156 (2018) 1837–1848. <https://doi.org/10.1016/j.jtcvs.2018.05.042>.
- [145] H.W. Coleman, W.G. Steele, *Experimentation, validation, and uncertainty analysis for engineers: Fourth edition*, 2018. <https://doi.org/10.1002/9781119417989>.
- [146] E. Lazar, B. DeBlauw, N. Glumac, C. Dutton, G. Elliott, A practical approach to PIV uncertainty analysis, in: *27th AIAA Aerodyn. Meas. Technol. Gr. Test. Conf.* 2010, 2010. <https://doi.org/10.2514/6.2010-4355>.
- [147] B.H. Timmins, B.W. Wilson, B.L. Smith, P.P. Vlachos, A method for automatic estimation of instantaneous local uncertainty in particle image velocimetry measurements, *Exp. Fluids.* 53 (2012) 1133–1147. <https://doi.org/10.1007/s00348-012-1341-1>.
- [148] S. Scharnowski, C.J. Kähler, Estimation and optimization of loss-of-pair uncertainties based on PIV correlation functions, *Exp. Fluids.* 57 (2016). <https://doi.org/10.1007/s00348-015-2108-2>.
- [149] C. Cierpka, M. Rossi, R. Segura, F. Mastrangelo, C.J. Kähler, A comparative analysis of the uncertainty of astigmatism- μ PTV, stereo- μ PIV, and μ PIV, *Exp. Fluids.* 52 (2012). <https://doi.org/10.1007/s00348-011-1075-5>.
- [150] M. Stanislas, J. Kompenhans, W. J, *Particle Image Velocimetry - Progress towards Industrial Application*, 2007.
- [151] A. Sciacchitano, D.R. Neal, B.L. Smith, S.O. Warner, P.P. Vlachos, B. Wieneke, F. Scarano, Collaborative framework for PIV uncertainty quantification: Comparative assessment of methods, *Meas. Sci. Technol.* 26 (2015) 74004. <https://doi.org/10.1088/0957-0233/26/7/074004>.
- [152] K. Okamoto, S. Nishio, T. Saga, T. Kobayashi, Standard images for particle-image velocimetry, *Meas. Sci. Technol.* 11 (2000) 685–691. <https://doi.org/10.1088/0957-0233/11/6/311>.
- [153] M.B. Liu, G.R. Liu, Smoothed particle hydrodynamics (SPH): An overview and recent developments, *Arch. Comput. Methods Eng.* 17 (2010). <https://doi.org/10.1007/s11831-010-9040-7>.
- [154] E. Napoli, M. De Marchis, E. Vitanza, PANORMUS-SPH. A new Smoothed Particle Hydrodynamics solver for incompressible flows, *Comput. Fluids.* 106 (2015) 185–195. <https://doi.org/10.1016/j.compfluid.2014.09.045>.
- [155] A. Monteleone, M. Monteforte, E. Napoli, Inflow/outflow pressure boundary conditions for smoothed particle hydrodynamics simulations of incompressible flows, *Comput. Fluids.* 159 (2017) 9–22. <https://doi.org/10.1016/j.compfluid.2017.09.011>.

- [156] J. Peacock, T. Jones, C. Tock, R. Lutz, The onset of turbulence in physiological pulsatile flow in a straight tube, *Exp. Fluids*. 24 (1998). <https://doi.org/10.1007/s003480050144>.
- [157] M. Özdiñ Çarpınliođlu, M. Yařar Gündođdu, A critical review on pulsatile pipe flow studies directing towards future research topics, *Flow Meas. Instrum.* 12 (2001). [https://doi.org/10.1016/S0955-5986\(01\)00020-6](https://doi.org/10.1016/S0955-5986(01)00020-6).
- [158] R. Budwig, Refractive index matching methods for liquid flow investigations, *Exp. Fluids*. 17 (1994). <https://doi.org/10.1007/BF01874416>.
- [159] S.F. Wright, I. Zadrazil, C.N. Markides, A review of solid–fluid selection options for optical-based measurements in single-phase liquid, two-phase liquid–liquid and multiphase solid–liquid flows, Springer Berlin Heidelberg, 2017. <https://doi.org/10.1007/s00348-017-2386-y>.
- [160] P.R. Jackson, R.A. Musalem, C.R. Rehmann, D.F. Hill, Particle image velocimetry errors due to refractive index fluctuations, in: *Hydraul. Meas. Exp. Methods*, 2002. [https://doi.org/10.1061/40655\(2002\)86](https://doi.org/10.1061/40655(2002)86).
- [161] M.Y. Yousif, D.W. Holdsworth, T.L. Poepping, A blood-mimicking fluid for particle image velocimetry with silicone vascular models, *Exp. Fluids*. 50 (2011) 769–774. <https://doi.org/10.1007/s00348-010-0958-1>.
- [162] K.L. Billiar, M.S. Sacks, Biaxial mechanical properties of the native and glutaraldehyde-treated aortic valve cusp: Part II - A structural constitutive model, *J. Biomech. Eng.* 122 (2000). <https://doi.org/10.1115/1.1287158>.
- [163] R. Parker, R. Randev, W.H. Wain, D.N. Ross, Storage of heart valve allografts in glycerol with subsequent antibiotic sterilisation, *Thorax*. 33 (1978). <https://doi.org/10.1136/thx.33.5.638>.
- [164] R.F. Carey, B.A. Herman, The effects of a glycerin-based blood analog on the testing of bioprosthetic heart valves, *J. Biomech.* 22 (1989). [https://doi.org/10.1016/0021-9290\(89\)90220-0](https://doi.org/10.1016/0021-9290(89)90220-0).
- [165] E. Nader, S. Skinner, M. Romana, R. Fort, N. Lemonne, N. Guillot, A. Gauthier, S. Antoine-Jonville, C. Renoux, M.D. Hardy-Dessources, E. Stauffer, P. Joly, Y. Bertrand, P. Connes, Blood rheology: Key parameters, impact on blood flow, role in sickle cell disease and effects of exercise, *Front. Physiol.* 10 (2019). <https://doi.org/10.3389/fphys.2019.01329>.
- [166] J. Stuart, M.W. Kenny, Blood rheology., *J. Clin. Pathol.* 33 (1980) 417–429. <https://doi.org/10.1136/jcp.33.5.417>.
- [167] D.S. Long, M.L. Smith, A.R. Pries, K. Ley, E.R. Damiano, Microviscometry reveals reduced blood viscosity and altered shear rate and shear stress profiles in microvessels after hemodilution, *Proc. Natl. Acad. Sci.* 101 (2004) 10060–10065. <https://doi.org/10.1073/pnas.0402937101>.
- [168] A. Arzani, Accounting for residence-time in blood rheology models: do we really need non-Newtonian blood flow modelling in large arteries?, *J. R. Soc. Interface.* 15 (2018) 20180486. <https://doi.org/10.1098/rsif.2018.0486>.
- [169] D.Z. Stupar, J.S. Bajić, A. V. Joža, B.M. Dakić, M.P. Slankamenac, M.B.

- Živanov, E. Cibula, Remote monitoring of water salinity by using side-polished fiber-optic U-shaped sensor, in: 15th Int. Power Electron. Motion Control Conf. Expo. EPE-PEMC 2012 ECCE Eur., 2012. <https://doi.org/10.1109/EPEPEMC.2012.6397458>.
- [170] John D. Cutnell, K.W. Johnson, Physics, 1998.
- [171] PubChem, PubChem Compound Summary for CID 1030, Propylene glycol, Natl. Cent. Biotechnol. Inf. (2021). <https://pubchem.ncbi.nlm.nih.gov/compound/Propylene-glycol>.
- [172] A. Hasan, K. Ragaert, W. Swieszkowski, Š. Selimović, A. Paul, G. Camci-Unal, M.R.K. Mofrad, A. Khademhosseini, Biomechanical properties of native and tissue engineered heart valve constructs, *J. Biomech.* 47 (2014) 1949–1963. <https://doi.org/10.1016/j.jbiomech.2013.09.023>.
- [173] R. van Noort, S.P. Yates, T.R.P. Martin, A.T. Barker, M.M. Black, A study of the effects of glutaraldehyde and formaldehyde on the mechanical behaviour of bovine pericardium, *Biomaterials.* 3 (1982). [https://doi.org/10.1016/0142-9612\(82\)90056-4](https://doi.org/10.1016/0142-9612(82)90056-4).
- [174] J.A. Salmonsmith, Haemodynamic alterations after percutaneous valve implantation. Doctoral thesis (Ph.D), UCL (University Coll. London). (2019).
- [175] W.M. Swanson, R.E. Clark, Aortic valve leaflet motion during systole. Numerical-graphical determination., *Circ. Res.* 32 (1973). <https://doi.org/10.1161/01.RES.32.1.42>.
- [176] M.J. Thubrikar, M.R. Labrosse, K.J. Zehr, F. Robicsek, G.G. Gong, B.L. Fowler, Aortic root dilatation may alter the dimensions of the valve leaflets, *Eur. J. Cardio-Thoracic Surg.* 28 (2005). <https://doi.org/10.1016/j.ejcts.2005.09.012>.
- [177] H. Reul, A. Vahlbruch, M. Giersiepen, T. Schmitz-Rode, V. Hirtz, S. Effert, The geometry of the aortic root in health, at valve disease and after valve replacement, *J. Biomech.* 23 (1990). [https://doi.org/10.1016/0021-9290\(90\)90351-3](https://doi.org/10.1016/0021-9290(90)90351-3).
- [178] Y.A. Çengel, Introduction to thermodynamics and heat transfer / Yunus A. Çengel., 2008.